8-2019

Energy-Driven Analysis of Electronically-Interfaced Resources for Improving Power System Dynamic Performance

Horacio Silva Saravia
University of Tennessee, hsilvasa@vols.utk.edu

To the Graduate Council:

I am submitting herewith a dissertation written by Horacio Silva Saravia entitled "Energy-Driven Analysis of Electronically-Interfaced Resources for Improving Power System Dynamic Performance." I have examined the final electronic copy of this dissertation for form and content and recommend that it be accepted in partial fulfillment of the requirements for the degree of Doctor of Philosophy, with a major in Electrical Engineering.

Hector Pulgar, Major Professor

We have read this dissertation and recommend its acceptance:

Yilu Lu, Fran Li, Russell Zaretzki

Accepted for the Council:

Dixie L. Thompson

Vice Provost and Dean of the Graduate School

(Original signatures are on file with official student records.)

Energy-Driven Analysis of Electronically-Interfaced Resources for Improving Power System Dynamic Performance

A Dissertation Presented for the

Doctor of Philosophy

Degree

The University of Tennessee, Knoxville

Horacio Daniel Silva-Saravia

August 2019

Dedicated to my beloved mother Ana and son Tomas.

Acknowledgments

I would like to thank my family for always supporting me in this crazy journey that I started several years ago. My mom Ana who has always believed in me, and who makes me think I can achieve everything I dream of. My Son Tomas, who without too much of a choice when seeing his father leaving to another country, has been always understanding and sweet. Son, you are the reason I want to be the best version of myself, you motivate me to overcome any difficulty and you inspire me to leave a better world behind me. Thanks to my sisters Claudia and Paulina, my nieces Paz, Paloma, Martina and Valentina and my nephew and also friend Damian. You all make my life happy, despite the distance I will always be thankful for every video call, text and meme that made me smile thousands of miles away from my home. Thank you Tata for this beautiful family that you started, and thank you for ever for being there for me when I needed it. I know I make you proud in heaven.

I would also like to thank so many friends that are, or have been at some point, part of my graduate life. Each of you have made me the person that I am right now. Special thanks to Yajun, Jonathan and Mojtaba who were not only my office mates but also my first friends in the US. Life was pretty tough during my first year, but you guys made it all better. Also thanks to my Latino friends who often reminded me how to enjoy life with that signature style that we all have. Thanks Tay, Luna, Lucas, and so many other good friends. Thank you Diane for always being sweet and helping me get through the final part of my thesis and stressful job search.

Finally, I would like to thank all the professors in CURENT, specially my advisor Dr. Pulgar. You formed me as a researcher very early in my career back in Chile. I will always be grateful for every career advise, research discussion and countless comments in red for

my revised papers. Finally, as the famous Chilean singer Violeta Parra said, thank you to life, that has given me so much. And thank you God for all these wonderful people.

Abstract

This dissertation investigates the strengthening of power system dynamics with regard to electromechanical oscillations by using electronically-interfaced resources (EIR). The dissertation addresses (1) the modeling and control design of a flywheel energy storage system and a large-scale solar PV plant. The latest is enabled to participate in oscillation damping control without the need for power curtailment. (2) A new dynamic performance evaluation and coordination of damping controller is also developed to analyze systems with several critically low damping ratios. This is studied by using the system oscillation energy to define the total action and total action sensitivity, which allow the identification of control action that benefit exited modes, rather than fixed targeted modes. Finally, (3) this thesis proposes a solution for the site selection of EIR-based damping controllers in a planning stage. The effect of wind power variability and correlation between geographically closed wind farms is modeled to analyze the system performance and determine the site selection that maximizes the probability of dynamic performance improvement. Mathematical description as well as simulations in different multi-machine power systems show the advantages of the methods described in this work. The findings of this thesis are expected to advance the state-of-the-art of power system control by effectively and efficiently utilizing the fast power capabilities of EIR in systems with high penetration of renewable energy.

Table of Contents

List of Tables

List of Figures

Chapter 1

Introduction

1.1 Background and motivation

Electromechanical oscillations in power systems appear as the result of the energy exchange between different groups of synchronous generators after a disturbance. These oscillations are unwanted because of the mechanical stress in generator shafts, power congestion in the transmission system and the potential risk of instability. To avoid these problems, control efforts are done to guarantee higher damping ratios for these oscillations, with special consideration for inter-area oscillations, which involve a larger part of the system. Although for the current scenario these control actions fulfill the system requirements, research on control schemes and a better understanding of the oscillation problem need to continue as higher penetration of non conventional renewable energy (NCRE)—and decommission of traditional generation—will take place. This increasing penetration of NCRE is expected to reduce the relative inertia of the system, pushing power systems closer to their stability limits and leading to a higher risk of system blackouts [1, 2]

The traditional approach to tackle electromechanical oscillations consists of adding power system stabilizers (PSSs) in the excitation systems of synchronous generators. The machine and feedback signals selection is done by using residue analysis (mode controllability/observability) [3], [4]. Residue analysis focuses on selecting the input/output pairs that are most sensitive to displace a targeted eigenvalue to the left side of the complex plane. A similar approach has been extended for the selection of the location of flexible

AC transmission systems (FACTS) and energy storage systems (ESS) [5]. In these works, and the majority of real system studies [6], only single-mode analysis is performed. This is based on the assumption that there is only one dominant mode, which is not guaranteed in scenarios with high penetration of NCRE. To consider multi-mode analysis optimization-based techniques have been implemented to tune and design system controls [7]. This has brought the idea of control allocation and coordination in power systems to distribute control effort among multiple actuators [8]. However, these optimization-based techniques lack of physical interpretation and depend on arbitrary designed parameters.

A different approach to study electromechanical oscillations consists in analyzing the kinetic oscillation energy of each machine by comparing the phase of selected energy modes to identify energy exchanges paths [9], [10]. Recent efforts also consider the distribution of the kinetic energy, branch potential energy [11] and the idea of energy dissipation and its relationship with oscillation damping [12]. Although more meaningful in terms of the system physical interpretation, these works still fail to provide a performance index considering all system modes. Moreover, they do not provide direct comparison of different control actuators and the effects on the oscillation energy as a measure of system performance.

This dissertation addresses the oscillation problem from three different perspectives: (a) the enabling of new electronically-interfaced resources (EIRs) to participate in oscillation damping control (DC) and their analysis through appropriate electromechanical models. (b) The development of a new dynamic performance measure to compare the performance of EIRs in systems with multiple critical modes—expected to occur for high penetration of NCRE—and the utilization of this index to coordinate in real time EIR-based damping controllers. (c) The probabilistic analysis of the location selection for EIR-based damping controllers in a planning stage to reinforce the system performance.

1.1.1 Electronically-interfaced resources

EIRs correspond to any active element in the grid that is connected through power converters. Because of the fast dynamic response of the converters, in the range of 20 ms, these EIRs potentially have the capability to quickly inject or absorb active and reactive power into the grid, making them ideal for fast regulation such as primary frequency control or DC—e.g.,

by implementing inertia emulation or a virtual synchronous machine [13, 14]. The impact of these devices on the grid dynamic performance will depend on size and number of elements in the system, which have both considerably increased during the last years.

One example of EIRs that are well-known in the system are Flexible Alternating Current Transmission System (FACTS), such as Thyristor-controlled series capacitor (TCSC) and Thyristor-controlled series reactor (TCSR), Static VAR compensator (SVC) and Static synchronous compensator (STATCOM). These devices are known to have the capability to improve power system dynamics [15, 16, 17, 18]. Another example of EIRs are energy storage systems (ESSs) [19, 20]. The maturity in the technologies and the need of storage while facing variable generation, make ESSs an active participant in the power system, where high power and energy densities are usually required. Considering these requirements, capacitor-based energy storage [21, 22, 23], battery energy storage (BES) and flywheel energy storage (FES) are the most attractive candidates. Applications of BES to improve power system dynamics go from stability analysis [24, 25] to primary frequency regulation [26, 27], and damping of electromechanical oscillations [28, 29, 30]. With regards to FES, similar controllers—beyond the main usage for energy management and power leveling—have been studied such as frequency regulation [31, 32, 33] and damping of electromechanical oscillations [34, 35] among others [36]. Although these works study applications of FES in power systems, there is a lack of an appropriate electromechanical model and control design for bulk power system simulations, as well as guidance for system operators to select installation sites considering the system dynamic performance.

The most radical example of increasing EIRs in the system is NCRE. Wind turbine generators (WTGs) have installed 612 MW in the U.s. just during the third quarter of 2018, resulting in a 15% increase in installation over the third quarter of 2017 [37]. Note that WTGs have been studied in the literature to improve dynamic performance and stability [38], [39]. Similarly, solar energy keeps growing with photo-voltaic (PV) installation forecast of over 14,000 MWdc for 2023—more than double the current installed capacity. This growth is driven by progressive reduction in manufacture prices together with environmental policies favoring the use of both, residential and utility PV [40]. The control strategies as well the effects of utility-scale solar power plants on the system dynamic performance have

been a recent focus of attention [41, 42, 43]. Some previous efforts have been done in the literature to damp electromechanical oscillations by modulating reactive power of PV plants [44, 45]. The control is designed to provide sufficient damping for a wide range of operating conditions through a robust control formulation [46, 47], as well as adaptive control and delay inclusion [48]. Despite the damping improvement achieved by these strategies, reactive power modulation is limited to applications where the injection is close to the electrical midpoint between machines along a well-defined power flow direction [49]. This is not traditionally the case for transmission level applications; then, active power modulation is preferred as a better oscillation damping actuation.

Active power control of PV plant is typically designed to extract maximum power from the PV panels. This is attained by maximum power point (MPP) tracking algorithms that provide an adequate power reference that considers changes in solar irradiance and temperature. Some researcher have proposed to enable large-scale PV plants with active power controllers to participate in frequency control [50, 51] and oscillation DC [52]. However, in order to provide these controls the PV plant has to operate under its MPP, curtailing solar power. Curtailment is undesired because reduces the effective capacity factor of the plant and the energy sold to the grid, which increase the cost of energy and generation-related carbon emissions [53, 54]. Therefore, a different approach to enable active power modulation from PV generation is needed.

Finally, as the number of EIRs increases in the system, the opportunity for using their fast power injection capabilities arises, in particular, while looking at their oscillation damping capabilities. The potential for enabling damping controllers into EIR—specially elements that require more investigation such as flywheels and PV plants—becomes an interesting problem. Additionally the coordination of these controls in real time and their site selection in a planning stage remains as a research problem that can importantly help system operators. These two new problems, and the literature review on them are described in the next sections.

1.1.2 Coordination problem

The coordination of different controllers is not a new problem in power systems. This coordination is specially necessary when the control objectives have conflicting effects on the performance, such as in the case of transient stability and voltage regulation. One approach to study this problem is the switching between different local controllers; this has been addressed in [55] for a single machine infinite bus system by defining membership functions for the switching. A robust control design for nonlinear controllers has also been proposed by using a Riccati equation approach to guarantee transient stability enhancement and voltage regulation [56, 57]. A similar conflict occurs in transient stability for adaptive controllers, where the authors propose a stable strategy for the switching between multiple models of a plant [58].

In regards to the damping of electromechanical oscillations addressed in this thesis, the coordination can have different purposes. The first common goal in the coordination of damping controllers is to achieve a desired dynamic performance, which avoids adverse dynamic behaviors, e.g., negatively impacting the damping of a local mode while targeting an inter-area mode. This coordination has been studied in terms of the optimal control of distributed resources [59, 60] and the use of wide-area DC (WADC) [61]. Another approach is to solve an optimization problem, either in terms of state trajectories or eigenvalue displacements to determine the tuning of the damping controllers [62, 63, 64, 65]. The second common purpose of the coordination of damping controllers is to achieve stability and robustness under a wide range of operation, such as in [66] where a supervisory level controller in a hierarchical structure using wide-area measurements coordinates local stabilizers by using multi-agent system theory. The supervisory level control can effectively damp system oscillations under a wide range of operating conditions. This idea of coordination, often mentioned as adaptive in terms of operation or unknown parameters, also considers the idea of switching selected controllers from a finite family of candidate controllers [67, 68].

A similar switching approach between different stabilizer controllers—in a more general sense than power systems—can be applied by using switched systems theory [69]. By this approach stability can be guaranteed for any switching sequence. Furthermore, this idea

of switching has also been used in robotics, where an adaptive switching learning control method achieves asymptotic convergence based on a Lyapunov's method [70]. Although all these approaches show potential for coordination of damping controllers, they often focus on stability rather than performance, which lead to suboptimal use of the DC resources. The main reason for this is that performance has not been formally defined in a global system sense, recurring to arbitrary operational definitions such as controlling to achieve a damping ratio higher than some benchmark for a dominant mode. This thesis uses the concept of oscillation energy and total action to propose an objective function for the switching of EIR-based damping controllers driven by dynamic performance.

1.1.3 Planning problem

This problem, referred to in this thesis as dynamic performance reinforcement planning (DPRP), consists of finding the optimal locations in the system to install EIRs-based damping controllers that would improve the power system dynamic performance. Traditionally, the allocation of EIRs has been driven by economics, such as load leveling [71], minimization of losses and loading levels in selected lines [72] or planning for ESS in energy and reserve markets to reduce the system operating cost [73]. However, as the dynamic control becomes more challenging, the consideration of dynamics in the location problem has gained attention. Some examples are the optimal allocation of ESS for Voltage Control in low voltage distribution networks [74], the site selection of shunt active filters for damping of harmonic propagation in power distribution systems [75] and the location of var sources to tackle fault-induced delayed voltage recovery issues under severe contingencies [76], among others.

Concerning the planning of EIR sites for enhancing damping of electromechanical oscillations, previous work has been done on the location of FES in multi-machine systems [5, 77], and FACTS in a bulk power system—Nashville area in the Tennessee Valley Authority system [78]. Preliminary results also show the importance of wind farm locations [79] and how to select these locations for any EIR based on eigenvalue sensitivity of a dominant mode by comparing the mode controllability of a set of candidate buses [80]. A similar problem is to consider the robust inertia allocation problem, where the optimization is

carried out accounting for the worst-case disturbance location using an energy amplification measure [81]. Aware of the empirical dependency between the location of EIR and the inertia distribution of the system, an explicit analytical relationship found that the optimal location of damping controllers corresponds to the point with largest distance to the center of inertia [82]. This conclusion was proved for a single machine infinite bus system and verified for a large scale system by using a phasor measurement unit (PMU) based index to estimate the inertia distribution [83].

The main disadvantage of these inertia-based approaches is the assumption of a unique dominant mode driving the oscillation and the energy exchange path. For large systems, there exist several inter-area modes which may become dominant depending on the current system operation and power flows. This results on two deficiencies of the model: (a) the need to combine the information provided by all relevant eigenvalues and (b) the need to include the variations on the root locus of the eigenvalues when the operation changes. This changes mainly occur because of the variability added by the large penetration of NCRG. Point (a) is addressed in this thesis by using the oscillation energy and total action analysis. Point (b) is addressed by using a probabilistic framework.

Traditionally, small signal stability analysis with sources of uncertainty has been modeled with probabilistic approaches by using eigenvalue sensitivities. Linear approximation of the relationship between system eigenvalues and a random system element, such as load or generation, allows one to characterize the distribution of system eigenvalues, given the probability density function (pdf) of the random variables of interest [84]. Analytical methods have been investigated to construct the pdf of critical modes, determining the probability of system instability under scenarios of wind generation [85]. Recently, nonlinear relationships have also been analyzed to obtain the cumulative distribution function (cdf) of the damping ratio of a dominant mode [86]. The stochastic information of system eigenvalues can be used to control the system, for example, through optimal tuning of actuators by defining probabilistic objective functions of all system eigenvalues [87]. Furthermore, more detailed models considering correlation between random variables can improve the accuracy of the results, which has been proved in problems such as transmission planning [88], generation scheduling [89] and available transfer capacity [90]. Typically, the correlation can

be added to the model by selecting the random number seeds in the moving average (MA) part of an autoregressive moving average (ARMA) model [91], or by Nataf transformation and copula theory [92, 93] through the sample generation in a Monte Carlo simulation.

This thesis addresses the DPRP problem for electromechanical oscillations using oscillation and total action to assess the dynamic performance considering all relevant oscillation modes. Moreover, the planning is solved in a probabilistic framework considering the variability of wind power by performing a chance-constrained optimization and analyzing the effects of spatial correlation between geographically distributed wind farms in the dynamic performance.

1.2 Thesis outline and main Contribution

The findings of this thesis are organized in three parts.

1.2.1 Part I

Part I describes the modeling and damping control of a flywheel energy storage system and a large-scale solar PV plant in Chapter 2 and Chapter 3, respectively. Chapter 2 presents a comprehensive Surface Permanent Magnet Machine (SPMM) based FES plant model for electromechanical dynamic analysis. The dynamic behavior of the flywheel motion, dc-link capacitor and controllers are incorporated to the model. Four local controllers are considered to regulate FES power output, flywheel SOC, dc-link voltage, and reactive power injection from the grid side converter. A plant-level controller is implemented to provide transient support during frequency excursions. A 50 MW FES plant with 50 flywheel parallel array equivalents is tested in the NCIS and its impact on inter-area oscillation is evaluated. To identify prospective locations to install the FES plant, an algorithm based on inter-area mode controllability is proposed and tested in time-domain simulations. Results show that ideal locations are more importantly related to system physical characteristics rather than operational conditions; this revealing finding has the potential to lead to useful criteria for power system planning in regards to storage systems. Chapter 3 proposes a method to enable large-scale PV solar plants for electromechanical oscillation DC without the need

for curtailment. The method consists of acting on the panel voltage to transiently reduce the PV power, creating a margin for modulation and then modulating power to damp the oscillations. The control design, panel voltage strategy and implementation is tested in the two-area system. A comparison of the SDM control with a curtailment-based PV damping control is also explored in a test case of the 179-bus WECC system with six large-scale PV plants, showing the great damping capability of the proposed method.

1.2.2 Part II

Part II introduces a new energy-based performance measure for oscillation damping analysis in systems with several critical electromechanical modes and proposes a method to coordinate EIR-based damping controllers. Chapter 4 describes the kinetic oscillation energy, total action to address the problem of multiple critical modes by obtaining weighting factors for the determination of the most relevant modes in the energy exchanged between generators. Then, the total action sensitivity is used to compare the performance of EIR-based DC. The most sensitive actuators/locations are proven to provide the best dynamic response for the system. Simulations in the IEEE 9-bus system and IEEE 39-bus systems verify the findings of this work. Chapter 5 designs a fault-adaptive coordination of damping controllers. The adaptive coordination provides switching signals (on/off) to the local damping controllers depending on the particular disturbance, enabling controllers that tackle only excited modes. The proposed control provides binary signals (on/off) rather than damping signals as in other approaches, which ease the computational burden and it makes the control robust against sensor and communication delay. Simulations in the 179-bus WECC system validate the results, proving that the adaptive coordination can improve the dynamic performance by utilizing existing damping control resources in a more effective way.

1.2.3 Part III

Part III focuses on the solution of the DPRP problem by developing a probabilistic framework in the selection of EIRs locations. Chapter 6 provides a new probabilistic measure to determine the optimal location of EIR in a DPRP problem considering variability in

systems with high penetration of wind power. The problem is solved by chance-constrained optimization, using a linear estimation of the total action as a system performance index in the objective function, and the probability of a set of disturbances. Simulations are performed in the IEEE-39 bus system with 30% of wind penetration. Monte Carlo simulations show the computational advantage of the linear estimation compared to the exact calculation for analyzing the location of an EIR-based DC. The optimization results show that the best location for EIR-based DC differs from that obtained with traditional stochastic analysis of dominant mode or arbitrary benchmark for damping ratios. This occurs because the proposed approach chooses the location that maximizes the probability that the best system dynamic behavior is guaranteed. Chapter 7 analyzes the effect of wind farm spatial correlation on the performance of electromechanical oscillations in the WECC system. Three correlation cases are investigated based on real wind speed data, with consideration of geographical distance between the wind farms. The dynamic performance is evaluated by means of the total action to naturally capture the dynamic behavior of all modes of interest in the system oscillation energy following a disturbance. The sensitivity of the results respect to the dependence structure using Copula theory is examined for a Gaussian copula and t-copula.

Figure 1.1 shows a flowchart highlighting the three parts of the dissertation.

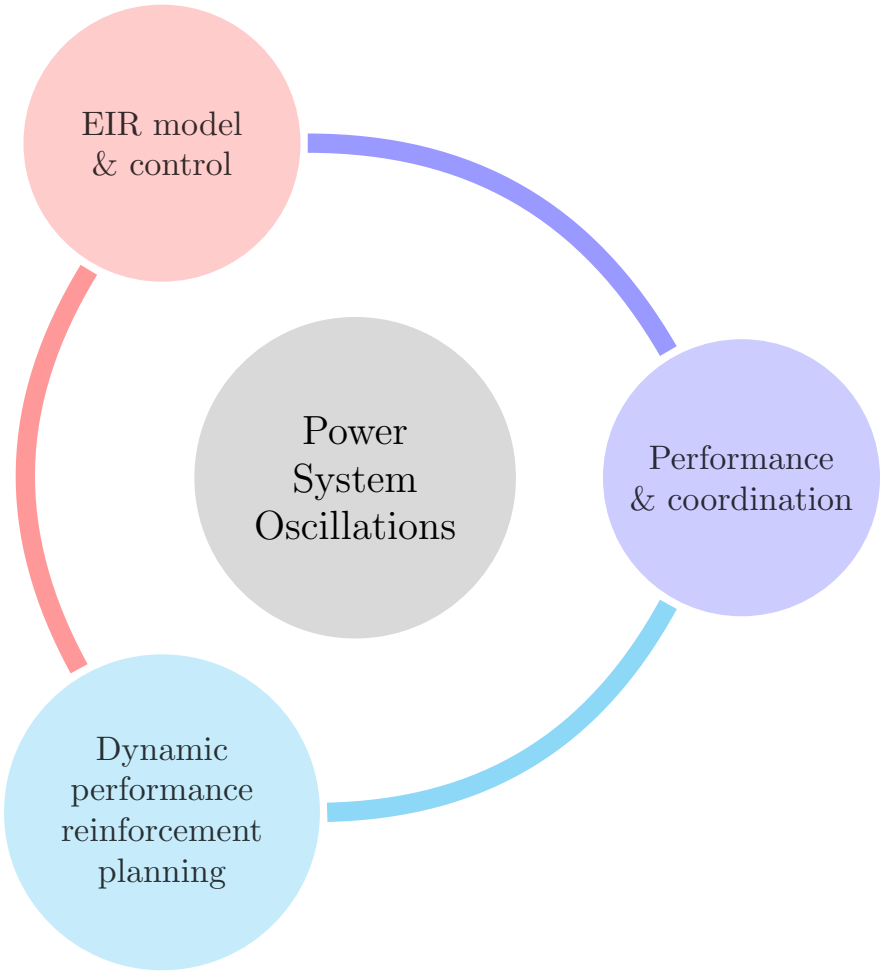

Figure 1.1: Diagram of the main parts of this thesis.

Part I

EIR model and control

Chapter 2

Flywheel energy storage model, control and location for improving stability: The Chilean case

A Flywheel Energy Storage (FES) plant model based on permanent magnet machines is proposed for electro-mechanical analysis. The model considers parallel arrays of FES units and describes the dynamics of flywheel motion, dc-link capacitor, and controllers. Both unit and plant-level controllers are considered. A 50 MW FES plant model is tested in the Northern Chile Interconnected System (NCIS) when connected to the Argentinian Interconnected System (AIS). The FES plant provides transient support for primary frequency regulation and its impact on stability is studied using small-signal analysis and time domain simulations. To identify the best location to install the FES plant, eigenvalue sensitivity for the inter-area mode is analyzed. The results are validated for different operation scenarios of wind and solar power. By installing the FES plant in the NCIS best location, the damping ratio of the inter-area mode is increased from 0.53% to 13.1% . Moreover, the power transfer from the NCIS to the AIS can be augmented from 90 MW to 180 MW while still keeping the damping ratio above 9%

2.1 Flywheel energy storage

A flywheel energy storage system consists mainly of three components: the flywheel itself, an electric machine and a back-to-back converter. The main characteristics of each component are summarized below:

Flywheel

This is a rotating mass that stores kinetic energy, which is proportional to the flywheel inertia and to the square of the rotating speed. FES can be classified in two types: low speed FES, with a speed less than 6×10^3 rpm, and high speed FES, which typically rotates in the range of $10^4 - 10^5$ rpm [94]. The flywheel is generally placed inside a vacuum container to eliminate friction-loss and suspended by magnetic bearings for a stable operation. To increase flywheel endurance at high operational speed, special materials such as carbon fiber composite are used [95].

Machine

This converts the kinetic energy into electricity. Induction machines [96], switched reluctance machines [97] or permanent magnet (PM) machines [98] have been employed—wound rotor machines are avoided due to the high speed. For grid connected applications, however, PM machines are more suitable due to their high power density and high efficiency. PM machines are classified either as interior or surface type [99]. Interior PM machines allow higher operational speed but they are harder to build compared to surface PM machines; thus, SPMM has become more common in the market. In regards to the control, for a wide range of rotational speed, PM machines are operated using field oriented control strategy. For extreme speed deviations, either very low or high speed, the control strategy of PM machines is turned to field weakening. In this work, for the sake of model simplicity, the SPMM with field oriented control is employed.

Converter

A back-to-back topology is generally considered. While the ac/dc converter on the grid side regulates the active and reactive power delivery to the grid, the other ac/dc converter controls the machine. As the purpose of this paper is to evaluate the impact of FES on power systems, with dynamics in a slower time-scale than those from the converter, full description of converter dynamics and control is not needed, instead, a simplified representation suffices.

2.2 Proposed FES model

A configuration with n_p flywheel-converter units connected in parallel to a common dc-bus is typically employed as shown in Figure 2.1(a) [100]. On the dc side, a parallel capacitor, a dc/ac converter and a step-up transformer provides the final grid connection of what is called the flywheel parallel array. In this paper, for modeling simplifications, the parallel units are aggregated to obtain a flywheel parallel array equivalent (FPAE) shown in Figure 2.1(b).

2.2.1 Mathematical representation of the FPAE

Consider the equivalent SPMM represented in a rotor reference frame, where the q-axis leads the d-axis by 90 degrees, and define currents leaving the machine (generator mode). By assuming also a single mass model which takes into account the masses of the equivalent flywheel and SPMM rotor, the open-loop FPAE model becomes:

$$\frac{1}{\omega_b} L_d \frac{di_d}{dt} = v_d - r_s i_d + \omega_r L_q i_q \tag{2.1}$$

$$\frac{1}{\omega_b} L_q \frac{di_q}{dt} = v_q - r_s i_q - \omega_r (L_d i_d + \Phi_f) \tag{2.2}$$

$$2H \frac{d\omega_r}{dt} = T_m - \underbrace{\Phi_f i_q}_{T_e} \tag{2.3}$$

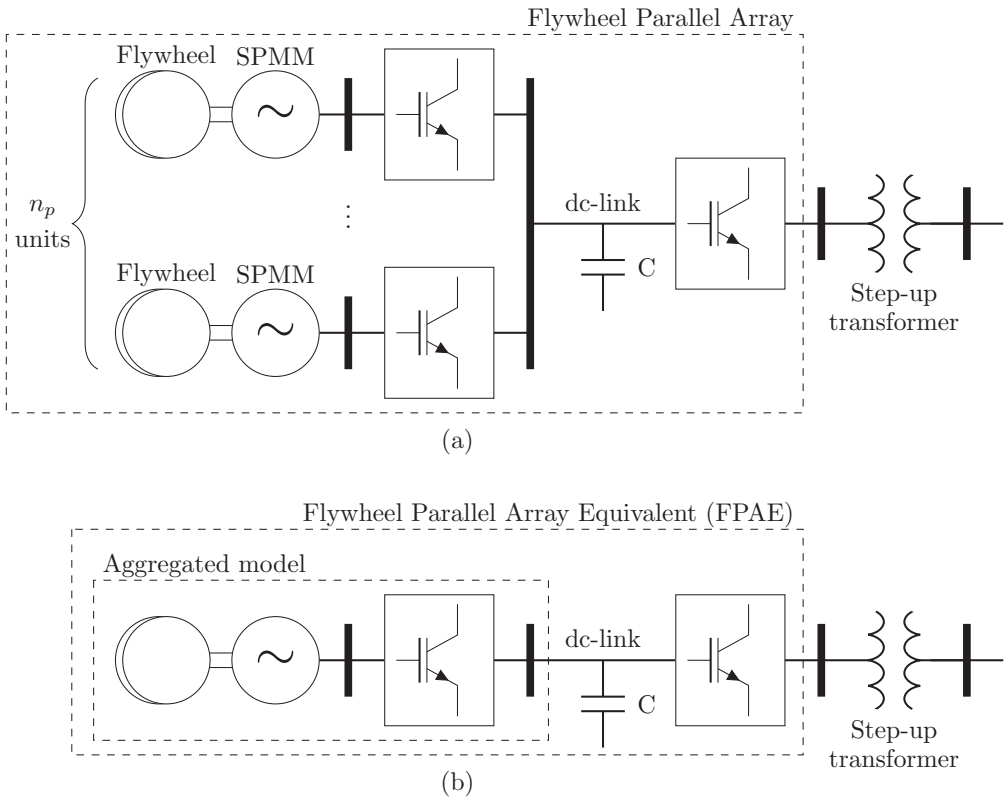

Figure 2.1: FES configuration: (a) Flywheel parallel array, (b) FPAE

$$C_{eq}\,\frac{dv_c}{dt} = \frac{\omega_r T_e}{v_c} - i_g \tag{2.4}$$

$$P_g = v_c i_g \tag{2.5}$$

Equations (2.1)-(2.3) represent the equivalent flywheel-SPMM. Here, r_s is the stator resistance; L, v, i the inductance, voltage and current in the d-q axis, respectively; T_e and T_m the electrical and mechanical torque; Φ_f the permanent flux; H the H-constant of inertia; ω_r the angular speed; and ω_b the SPMM electrical base frequency. Equations (2.4)-(2.5) represent the dc-link at the back-to-back converter. Here, v_c is the dc voltage; i_g and P_g the current and power through the grid-side (GS) converter; $C_{eq} = CV_{dc,b}^2/S_b$ where C is the dc-link capacitance, $V_{dc,b}$ the dc base voltage, and S_b the FPAE base power. Note that all variables and parameters are in per unit, except for H in seconds, ω_b in rad/s, C in F, $V_{dc,b}$ in V, and S_b in W. Some remarks about this model:

- Friction torque is not considered, which is a reasonable assumption due to the use of magnetic bearings [95].
- $T_m = 0$, as there is no external mechanical source exerting torque on the flywheel shaft.
- Power losses are negligible, thus, r_s is assumed to be zero and P_g becomes the power injected to the grid.
- Voltages v_d and v_q, provided by the machine-side (MS) converter, are controlled to maximize the SPMM efficiency. As a result, v_d and v_q are such that $i_d = 0$. With this consideration, stator flux is reduced and core loss minimized [101].

The H-constant of an equivalent flywheel is assumed to be $H = 450$ s on a 1 MW power base; this considers a stored energy of 250 kWh, so the flywheel would provide energy for approximately $2 \times 450 = 900$ s= 15 min [102]. To have an acceptable voltage ripple at the dc-link, the capacitance is chosen to be $C = 4 \times 10^{-3}$ F which implies a $C_{eq} = 2.25 \times 10^{-3}$ FΩ considering $S_b = 1$ MW and $V_{dc,b} = 750$ V —for dc-link capacitor sizing see reference [103]. With such a large H-constant and C_{eq}, and by considering that $L_d \ll \omega_b$ and $L_q \ll \omega_b$ as well, the model is time-scale separable as $\frac{L_d}{\omega_b} \ll \{C_{eq}, 2H\}$ and $\frac{L_q}{\omega_b} \ll \{C_{eq}, 2H\}$. By using a zero-order manifold for the dynamics in the d-q axis, the following relationships are obtained:

$$0 = v_d - \cancelto{0}{r_s} i_d + \omega_r L_q i_q \;\Rightarrow\; v_d = -\omega_r L_q i_q \tag{2.6}$$

$$0 = v_q - \cancelto{0}{r_s} i_q - \omega_r (L_d \cancelto{0}{i_d} + \Phi_f) \;\Rightarrow\; v_q = \omega_r \Phi_f \tag{2.7}$$

As a result, v_q must be proportional to the angular speed—related to the state of charge (SOC)—and v_d is controlled to have a desired current i_q—related to the FPAE power. The power extracted from the FPAE is then given by:

$$P_{fes} = \omega_r T_e = \underbrace{\omega_r \Phi_f}_{v_q} i_q = v_q i_q \tag{2.8}$$

Finally, the open-loop fundamental FPAE model is:

$$2H\frac{d\omega_r}{dt} = -\Phi_f i_q \tag{2.9}$$

$$C_{eq}\frac{dv_c}{dt} = \frac{\omega_r \Phi_f i_q}{v_c} - i_g \tag{2.10}$$

$$P_g = v_c i_g \tag{2.11}$$

The model fundamental variables are ω_r, i_q, v_c and i_g. The variables v_d and v_q are not explicitly required; converters are assumed to provide them in accordance to equations (2.6)-(2.7).

In order to validate the FPAE proposed model, a full detailed electromagnetic model was implemented in PLECS for comparison—this software is one of the standards to simulate nowadays power electronics and electric machines and is adopted by the most important manufacturers like ABB and Infineon. The PLECS simulation file considers accurate models of switching devices (IGBT/Diodes) and their fast controllers. Simulations were performed using a time step of 1 μs. The full detailed and proposed models are compared for the most relevant variables; machine d-q currents (top), DC voltage (middle) and flywheel speed (bottom) are shown in Figure 2.2; the bode plots of both models are presented in Figure 2.3. As the results show remarkable agreement between both models, despite the neglected dynamics and assumptions, the proposed fundamental FPAE model is validated.

2.2.2 FES plant model and control

The FES plant model considers n FPAE connected in parallel and coordinated by a plant-level controller shown in Figure 2.4. Due to the use of a washout filter, this plant-level controller allows providing transient support during frequency excursions and low frequency oscillations; it also includes a phase lead compensator to enhance oscillation damping, and a droop characteristic. The output signal, P_{ref1}, is sent to each one of the FPAE. At the unit-level, a state-of-charge (SOC) controller is considered which produces the output P_{ref2} and has as input the flywheel speed and the signal S_1. Here, S_1 can simply represent a reference speed related to the desired FPAE SOC or it can be a system-level signal for ACE

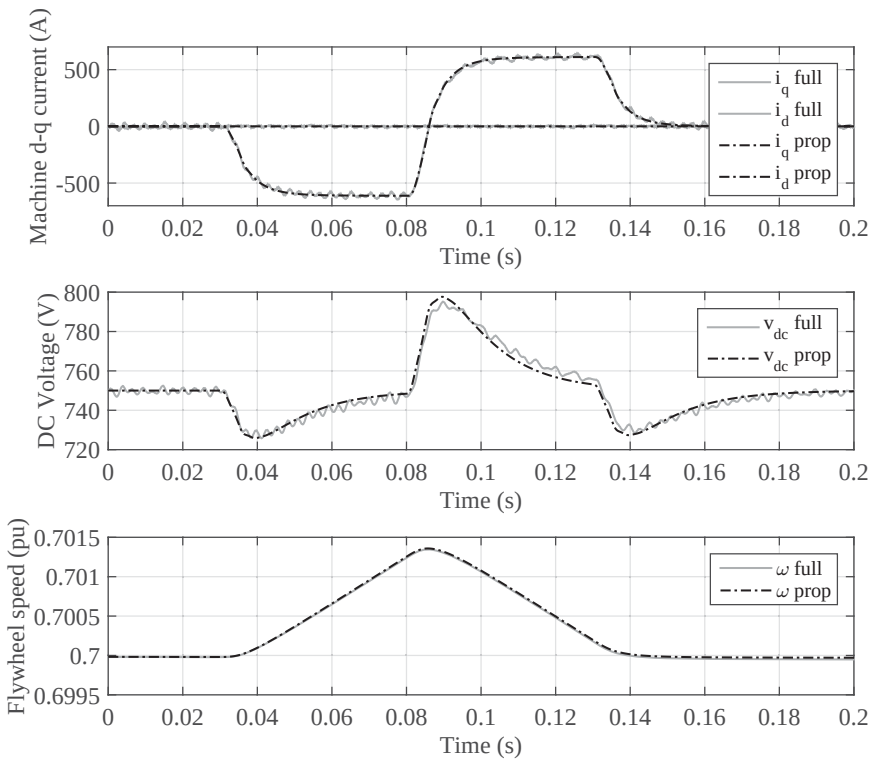

Figure 2.2: Comparison of FPAE variables response between the proposed and full detailed electromagnetic models

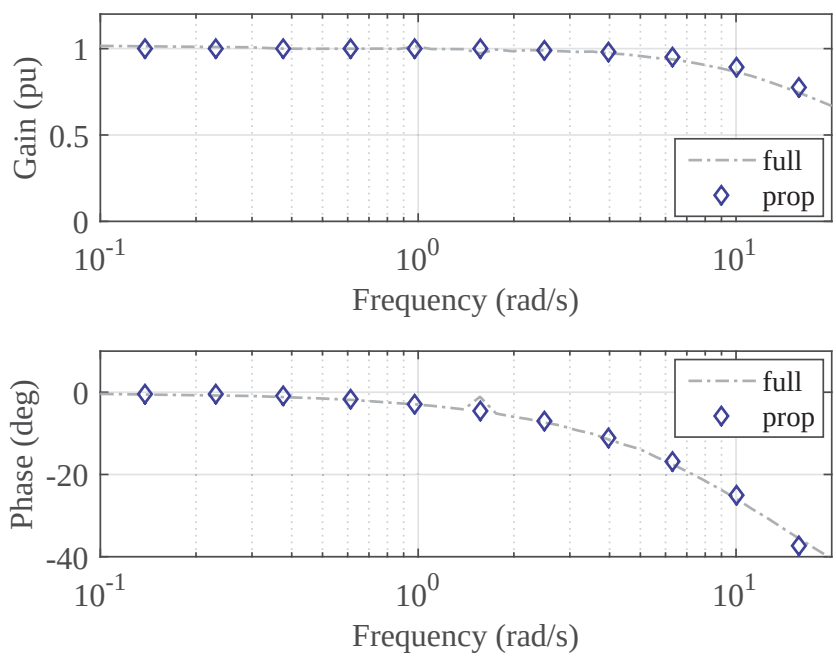

Figure 2.3: Bode plot comparison between the FPAE proposed and full detailed models

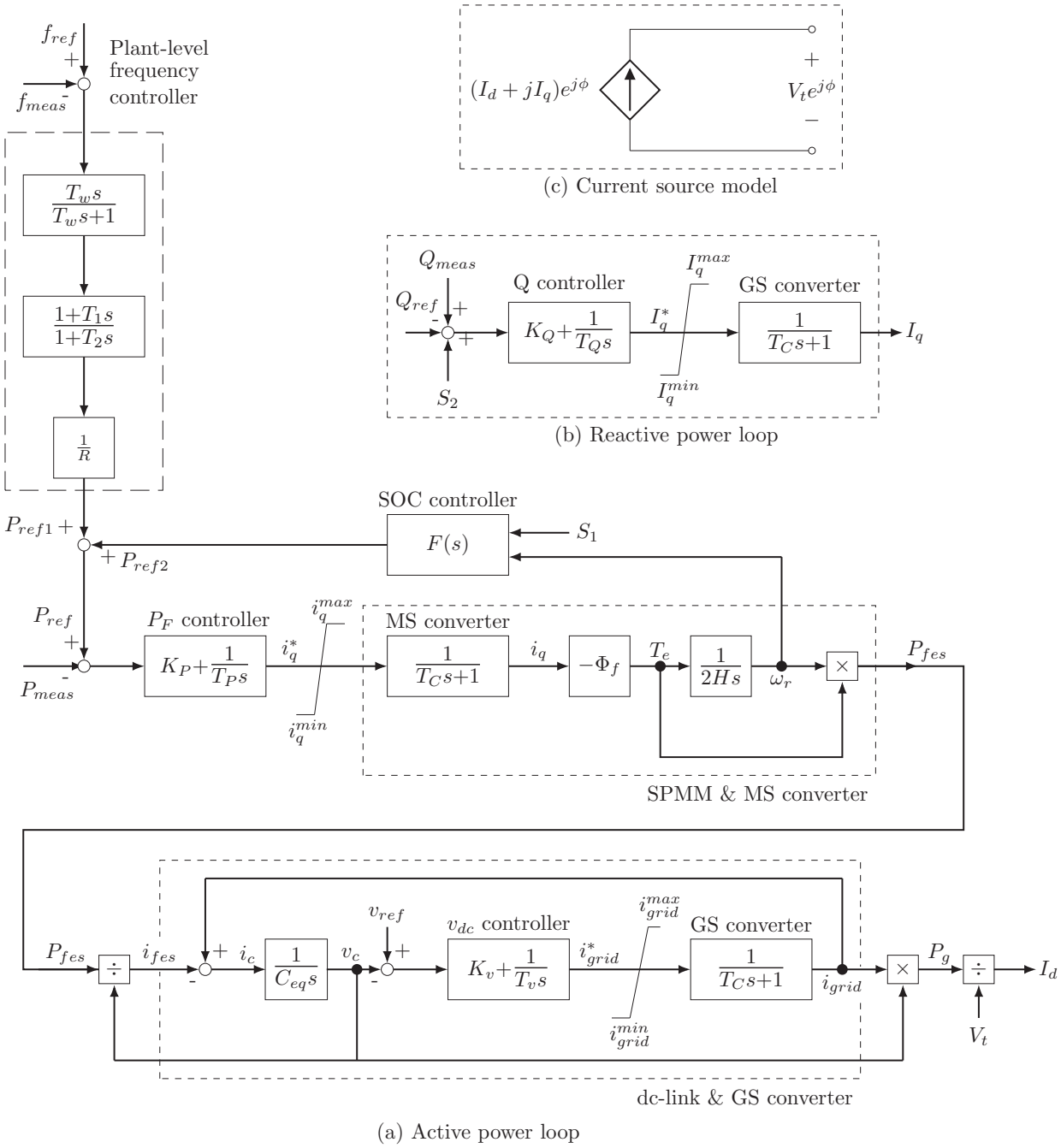

Figure 2.4: FPAE model and control

or secondary frequency control. The addition of these power references gives the total power reference, P_{ref}, that must be followed by FPAE. Note that these two controlling loops act on different timescales causing no controlling conflict—the impact of the SOC controller on frequency excursions or oscillations is marginal. For the purpose of this paper, $S_1 = \omega_{ref}$ so the SOC controller acts as a flywheel speed regulator, keeping the FPAE at a desired SOC level.

PI blocks are used to control P_{fes} and v_c to their respective reference values, i.e., P_{ref} and v_{ref}. The action of both MS and GS converters are modeled by a first order lag with a time constant of 0.5 ms. In addition, the GS converter may be used to provide reactive power support by using a PI-controller that acts on the quadrature current I_q based on the reactive power error. Furthermore, a system-signal S_2 may be employed to provide oscillation damping. As the capability of the GS converter may be limited, these actions require further evaluations. In this paper, both Q_{ref} and S_2 are assumed to be zero.

To represent the FPAE power injection to the grid through the GS converter, a controlled ideal current source is used (model on the power system side). The direct current I_d corresponds to the current component in phase with the FPAE terminal voltage $\overline{V}_t = V_t e^{j\phi}$, while the current I_q corresponds to the component in quadrature. The FPAE complex power injection is given by $S_g = \overline{V}_t \overline{I}_g^* = V_t I_d - j V_t I_q$; thus, I_d is related to the active power injection, and I_q to the reactive power injection.

2.3 Northern Chile Interconnected System (NCIS)

2.3.1 System characteristics

Some particular characteristics of this system are:

- This system is located in the northern regions of Chile, with an approximate total H-constant of 3.86 s base on its installed power.
- The installed capacity is about 4,150 MW, and the total demand around 2,400 MW—almost 90% of the demand is due to large mining companies. Due to minimum technical limits of generating units, there are typically a few power plants dispatched, each

one satisfying an important fraction of the load. Based on this, very large frequency excursions caused by generator outages or load rejections are possible, a situation that is critical considering the relatively slow governor responses of a mainly thermal system.

- The system is located in the Atacama desert, the driest in the world. As the solar energy potential is enormous, the installed capacity of zero-inertia generating sources is expected to increase in the near future; this is attractive from an energy point of view, but it is at least worrisome from a dynamic performance perspective due to the relative reduction of the system inertia.

- The system has two BES systems to meet grid reserve requirements: 12 MW Andes BES and 20 MW Angamos BES [104].

To export the generation surplus, the NCIS has been connected to the Argentinian Interconnected System (AIS) since 2015. The AIS is a large system with an installed capacity of about 31,000 MW. With the interconnection, frequency excursions are reduced on the NCIS side, but the problem of inter-area oscillations arises. In the case of disconnection, NCIS ISO must ensure that the system exhibits a frequency bounded by acceptable limits; as a result, ESS are still required to support primary frequency regulation.

2.3.2 Model, data and simulation

The characterization of each component of the NCIS has been obtained from the NCIS ISO website [105]—provided as a DIgSILENT simulation file. The model considers a sixth-order representation for generators, diverse governors and voltage regulators, and power system stabilizers to damp local oscillations at three power plants. In particular, the model includes a 90 MW wind farm and a total of 450 MW coming from several solar plants. In the data file, three load/conventional-generation scenarios are defined, which are called the high, medium and low demand scenarios. Power output from the RGS is assumed to be zero in these scenarios; however, system dynamic performance is later evaluated considering power output variability from the RGS. The full NCIS model has roughly 1,400 state variables and 2,700 algebraic variables. A simplified model for the AIS is used, which considers Salta Power

Plant connected through a 500 kV–1,500 km line to an equivalent generator—an equivalent H-constant of 6.77 s based on its installed power is assumed; typical parameters have been employed for the equivalent generator. Measured at the Andes busbar, a power transfer from the NCIS to the AIS of 90 MW is considered—this low power transfer is due to stability problems and is based on the current contractual agreement between both systems.

For time domain simulations a full non-linear representation of the NCIS is used, while for modal analysis the following linearized model is obtained:

$$\Delta\dot{x} = A\Delta x + B\Delta u \tag{2.12}$$

$$\Delta y = C\Delta x \tag{2.13}$$

where x is the vector of state variables, y the vector of output variables, u the vector of input variables and A, B and C are constant matrices. While the system matrix A is provided by commercial software packages such as DIgSILENT, the input matrix B is generally not available. In this paper, the coefficients of B are numerically estimated by observing the changes in the state variables, after a time step of 0.01 s, when a small and normalized change in the considered input is applied. Following a trial and error approach, this time step has been chosen after comparing the response of the full non-linear representation and the linearized model. The calculation of B is coded in DIgSILENT Programming Language. The coefficients of the output matrix C are explicitly defined.

2.4 NCIS dynamic analysis

A 50 MW FES plant is considered. This plant has 50 FPAE of 1 MW, with a 1.2 MVA–0.44/22 kV step-up transformer at each array. On the 22 kV side, all FPAE are connected in parallel, and the total power is sent to a collector bus through a 0.1 km line. At the line end, a 60 MVA–22/220 kV step-up transformer makes the final connection to the grid as shown in Figure 2.5. The FES plant data is shown in the Appendix A.

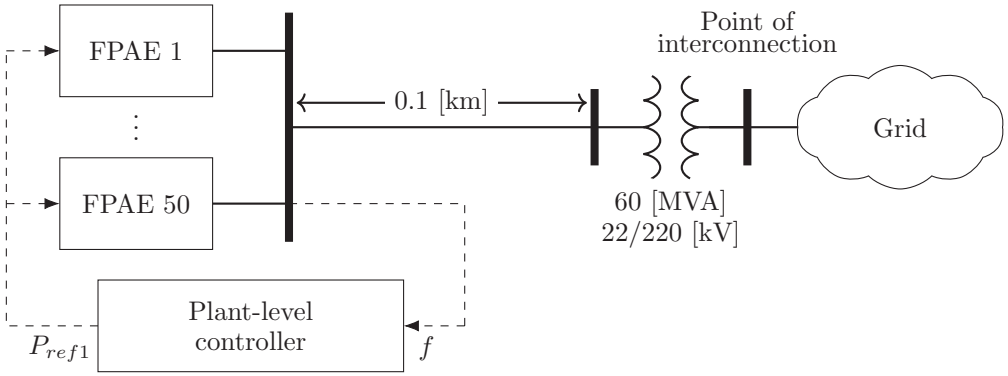

Figure 2.5: 50 [MW] FES plant model

2.4.1 Base case scenario

The high demand scenario without RGS production and FES plant is defined as the base case. Modal analysis reveals that the inter-area mode has a frequency of 0.37 Hz and a damping ratio of 0.53%—dangerous oscillations of the NCIS units against the AIS. All the analysis done in this section is related to this inter-area mode, as all other electromechanical modes, either intra-system, intra-plant, or local modes, have damping ratios above 9%. In regards to the NCIS BES plants, they have marginal effects on the inter-area mode damping due to the limitations imposed by dead bands.

2.4.2 FES location analysis

For frequency excursions, the location of these devices seems to be irrelevant, as any location would provide a similar performance. However, the location becomes crucial when these devices provide inter-area oscillation damping. To identify a preliminary ideal FES plant location, a plant-level controller with no wide-area measurement is assumed. This implies that, from a system point of view, the system input variable Δu (FES injected power) and the system output variable Δy (measured frequency) are unambiguously defined: these are the power and frequency at the busbar where the FES is installed. Let $\mathcal{L}$ be the set of all feasible locations to install a FES plant. Now, given a FES prospective location $\ell \in \mathcal{L}$,

consider the system open-loop transfer function given by:

$$G_\ell(s) = C_\ell(sI - A)^{-1}B_\ell \tag{2.14}$$

$$= C_\ell V(sI - \Lambda)^{-1}W^T B_\ell \tag{2.15}$$

$$= \sum_{i=1, i\neq j}^{n} \frac{C_\ell v_i w_i^T B_\ell}{s - \lambda_i} + \frac{C_\ell v_j w_j^T B_\ell}{s - \lambda_j} \tag{2.16}$$

Here, λ_i is the ith eigenvalue of A; v_i and w_i are the ith right and left column-eigenvector, respectively. The sub-index j represents the inter-area eigenvalue and eigenvectors. $\Lambda = \text{diag}\{\lambda_1, ..., \lambda_n\}$; $V = [v_1, ..., v_n]$; and $W = [w_1, ..., w_n]$—note that the sets of right and left eigenvectors are assumed to be orthonormal, thus, $W^T = V^{-1}$. The subscript ℓ in B_ℓ and C_ℓ indicates their dependency on the considered FES location.

The FES plant transfer function, from measured frequency to power injection, is defined as $KH(s)$; here, K is the FES-loop gain and $H(s)$ is a corresponding function. Then, the sensitivity of the inter-area eigenvalue λ_j of the closed-loop system with respect to the FES-loop gain is given by [106]:

$$\frac{\partial \lambda_j}{\partial K} = w_j^T \frac{\partial A}{\partial K} v_j = C_\ell v_j w_j^T B_\ell H(\lambda_j) \tag{2.17}$$

where $|C_\ell v_j|$ and $|w_j^T B_\ell|$ are called mode observability (MO_ℓ) and mode controllability (MC_ℓ) of the inter-area mode respectively. Having a SISO system, both indices are real scalar quantities. MO_ℓ does not change much with the location ℓ—which is reasonable as the inertia is smaller in the NCIS and all its units are coherently oscillating against those from the AIS. Based on this observation, the best locations ℓ can be simply chosen as those with the highest controllability index defined as $CI_\ell = MC_\ell / \max_\ell MC_\ell$, where $\max_\ell MC_\ell$ is the maximum MC out of all locations. Note that the angle of the sensitivity described by Equation (2.17) falls within $180 \pm \Delta\theta$; the phase compensation block shown in the FES plant model is tuned to cancel $\Delta\theta$—note that $|\Delta\theta| < 10°$ for all considered scenarios.

Using the base case scenario and defining the set $\mathcal{L}$ as all PQ buses of 220 kV, CI_ℓ for all $\ell \in \mathcal{L}$ are calculated and shown in Figure 2.6. Note that there are points of low controllability index in the south part of the system, close to the interconnection with the

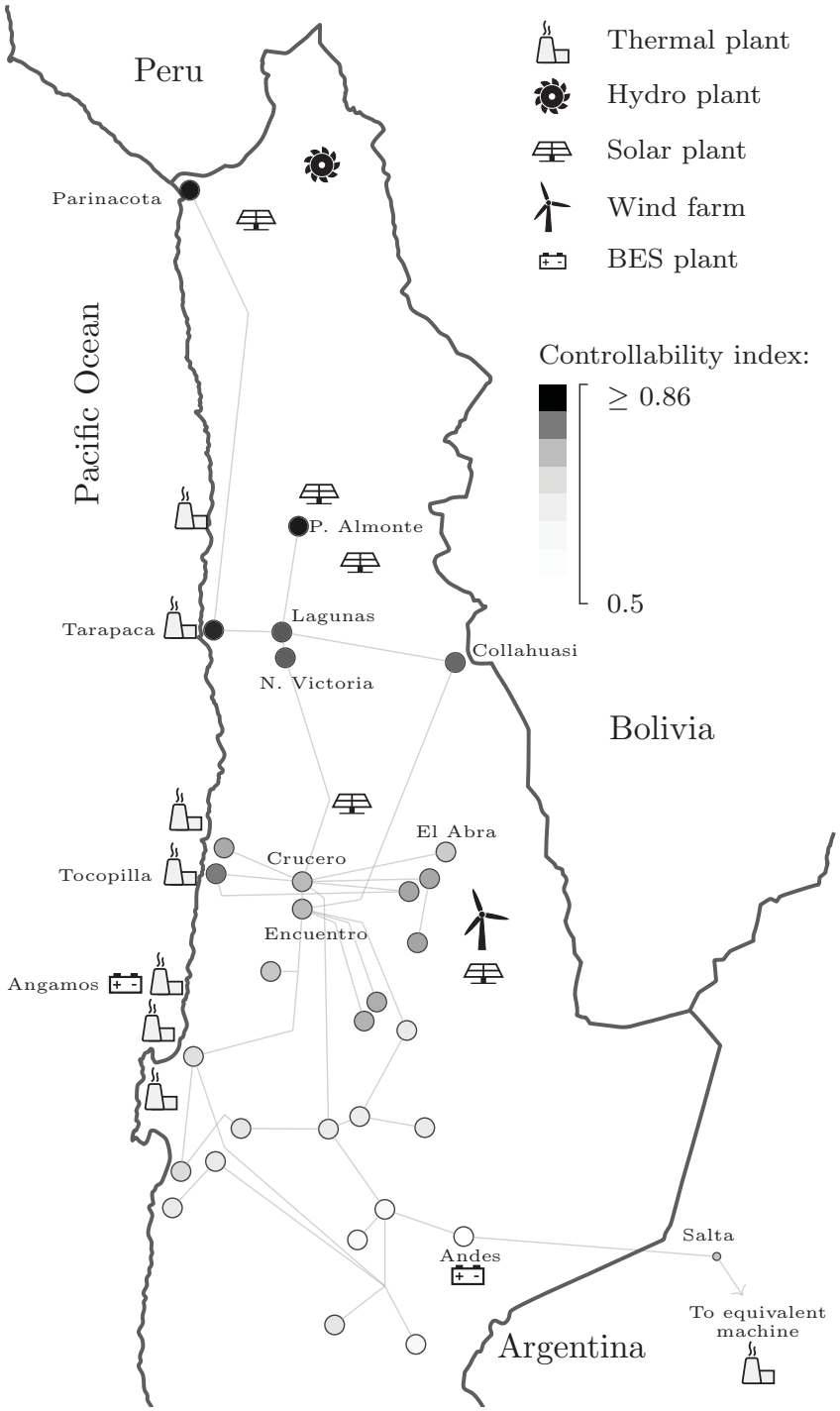

Figure 2.6: Controllability map

AIS (light gray), that gradually change to higher index points (dark gray to black) as the buses get farther away from the interconnection. This can be explained considering that the inertia of the AIS is several times higher than the inertia of the NCIS, and the inertia density on the NCIS side monotonically decreases in the north direction. Thus, the results point out that the least favorable location to control the inter-area oscillation is close to the center of inertia, while the best locations are those located in areas with low inertia density. This result is consistent with previous findings when wind turbines provide inertial response: the best wind farm locations are those areas with the smallest inertia [79].

To verify that this result mainly depends on the distribution of inertia rather than the system operational conditions, the analysis is repeated including power generation from the RGS and their variability. To create RGS generation scenarios, all solar plants are assumed to produce the same power no matter where they are located. This is a reasonable assumption as the NCIS is within a very narrow range in latitude and longitude, and the unlikely existence of clouds make the power production depend basically on the time of the day. Thus, specific levels of solar plant generation are created from 0 to 100% in steps of 20%. For each one of these power levels, the NCIS wind farm is assumed to also have power generation from 0% to 100% in steps of 20%—all in base of their own nominal power. As a result, and considering high, medium and low demand scenarios, 108 generation scenarios are used and defined as the set $\mathcal{S}$. In order to compensate the excess of generation due to the power coming from RGS, the dispatched power of those machines usually used for secondary frequency regulation is readjusted. Finally, CI_ℓ is determined for all $s \in \mathcal{S}$ and $\ell \in \mathcal{L}$, and the average value μ_ℓ and variance σ_ℓ^2 of the controllability index are calculated. Algorithm 1 summarizes the procedure.

A box plot of the controllability index for a sample set of buses under all the described scenarios is shown in Figure 2.7. Here the bottom and top of the box represent the first and third quartile, the band inside the box is the second quartile and the end of the whiskers show the minimum and maximum of all of the data. From this figure, observe the small variance of the controllability index, which shows that the result does not highly depend on the system operation, then it must somehow depend on the system physical characteristics [107], e.g., grid topology, geographical distribution of inertia, among others. In addition, within those

Algorithm 1 Procedure to determine FES plant locations

for each scenario $s \in \mathcal{S}$ **do**
    Calculate system equilibrium point
    Obtain inter-area eigenvalue and left eigenvector
    for each location $\ell \in \mathcal{L}$ **do**
        Determine B_ℓ through sensitivity
        Calculate $MC(\ell, s) = |w_i^T B_\ell|$
    end for
    Calculate $CI(\ell, s) = MC(\ell, s)/\max_{\ell} MC(\ell, s)\ \forall \ell$
end for
for each location $\ell \in \mathcal{L}$ **do**
    Calculate $\mu_\ell = \sum_s CI(\ell, s)/S$
    Calculate $\sigma_\ell^2 = \sum_s (CI(\ell, s) - \mu)^2/S$
end for
Select N candidates with the highest μ_ℓ and $\sigma_\ell^2 < \sigma_{max}^2$

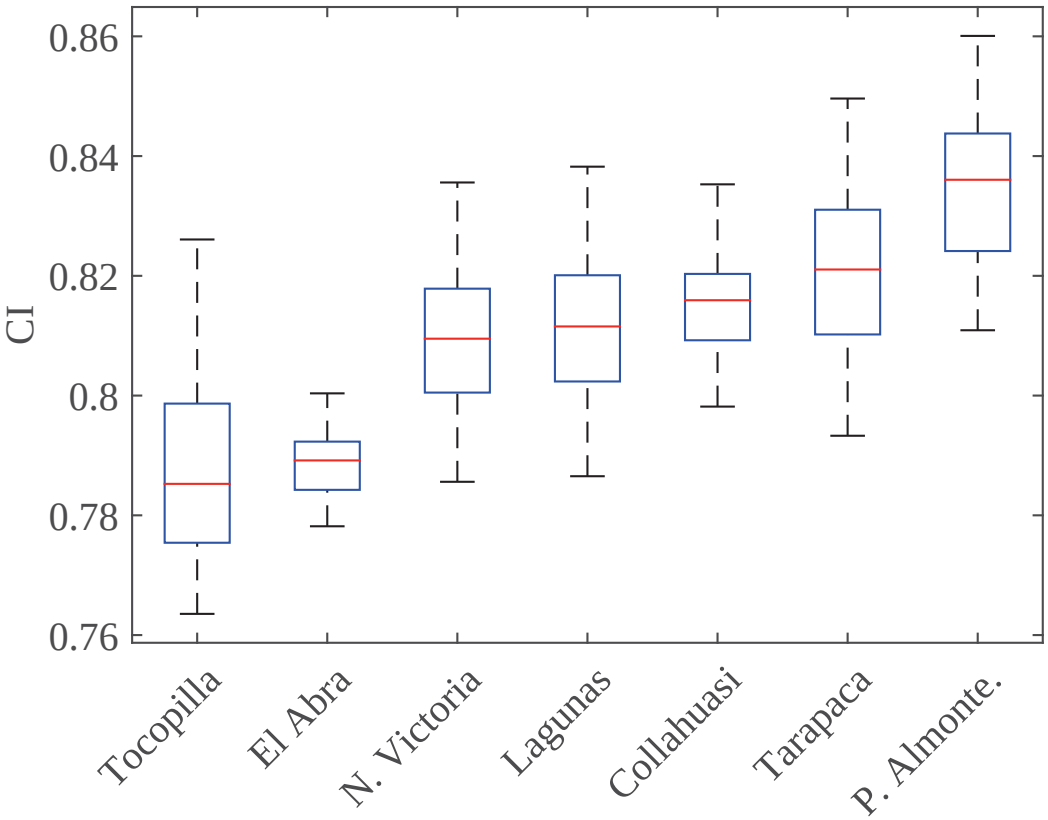

Figure 2.7: Box plot of mode controllability for a sample set of buses

small changes in the index, a positive correlation is found. This implies that the relative ranking of best candidates remains unchanged with respect to the load/generation scenario. With $N = 8$, the best FES locations are at the busbars: Parinacota, P. Almonte, Tarapaca, Collahuasi, Lagunas, N. Victoria, El Abra and Tocopilla.

2.4.3 FES plant impact on stability

The FES plant is added at some locations, and its impact on small signal stability and time-domain simulation is evaluated. Although several operating scenarios have been analyzed, only the base case with FES plant is presented here.

Small signal stability analysis

The best eight locations obtained with the previous algorithm are considered. For comparison purposes, Andes bus is also used as it has connected a BES plant. For all cases, the resulting inter-area eigenvalue with its corresponding frequency and damping ratio are presented in Table 2.1. Although the FES plant is controlled to provide primary frequency regulation, if properly located, it can have a tremendous impact on the inter-area oscillation, increasing the damping ratio from 0.53% to 13.1% in the best case. These results show a great agreement with those from the previous subsection; Andes bus having a low controllability index is only able to increase the damping ratio to 6.0%.

Time domain simulations

A three-phase short circuit with a clearing time of 64 ms is simulated at Crucero busbar to excite the inter-area oscillation between the NCIS and the AIS. Andes and Tarapaca are chosen as FES locations to contrast the system performance with and without FES plant. The time evolution of the generators speed for these cases is shown in Figure 2.8.

The results are consistent with those from Table 2.1 and Figure 2.6. The FES plant model proposed in this paper has a positive impact on the inter-area oscillation, especially when installed in the high controllability area. When the NCIS machines increase their speeds due to the fault, the FES plant absorbs energy that would be otherwise transformed

Table 2.1: Inter-area mode for different FES plant locations

Location	Eigenvalue	Frequency [Hz]	Damping [%]
No FES	$-0.012 + i2.297$	0.37	0.53
Parinacota	$-0.243 + i2.448$	0.39	9.9
P. Almonte	$-0.303 + i2.324$	0.37	12.0
Tarapaca	$-0.303 + i2.289$	0.36	13.1
Collahuasi	$-0.293 + i2.293$	0.36	12.7
Lagunas	$-0.295 + i2.282$	0.36	12.8
N. Victoria	$-0.294 + i2.284$	0.36	12.8
El Abra	$-0.283 + i2.319$	0.37	12.1
Tocopilla	$-0.294 + i2.228$	0.35	13.1
Andes	$-0.139 + i2.294$	0.37	6.0

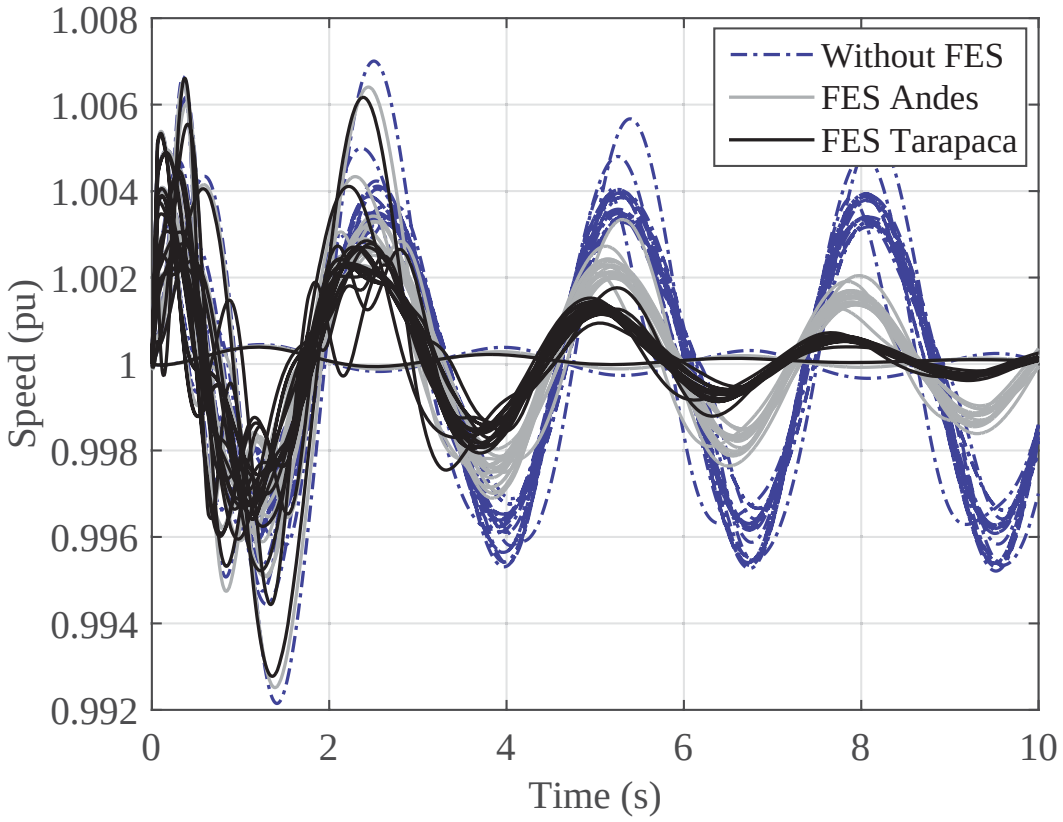

Figure 2.8: Generators speed after a 64 [ms] short circuit in Crucero busbar

into kinetic energy accelerating even more the machines. When the machines decelerate and the FES supplies energy, an excessive deceleration of the machines is avoided by the FES plant. It seems that the quick response during the first deciseconds of the FES plant connected in Tarapaca enables the control to achieve a better performance when compared to the FES connected in Andes. As a matter of fact, the FES plant in Tarapaca is more effective even though it uses in average 3% less of energy per discharge/charge cycle—see Figure 2.9. Despite the low capacity of the FES plant in comparison with the total power of both systems, the 50 MW plant is proven to be successful to drive the system from an almost unstable operation to a safe one with damping ratio above 10% and even been able to double the power transferred to the AIS with a damping ratio still above 9%. In all cases the FES acts just a few seconds; SOC of the FES plant is almost unaffected which ensures full capability for mid-term regulation such as ACE control.

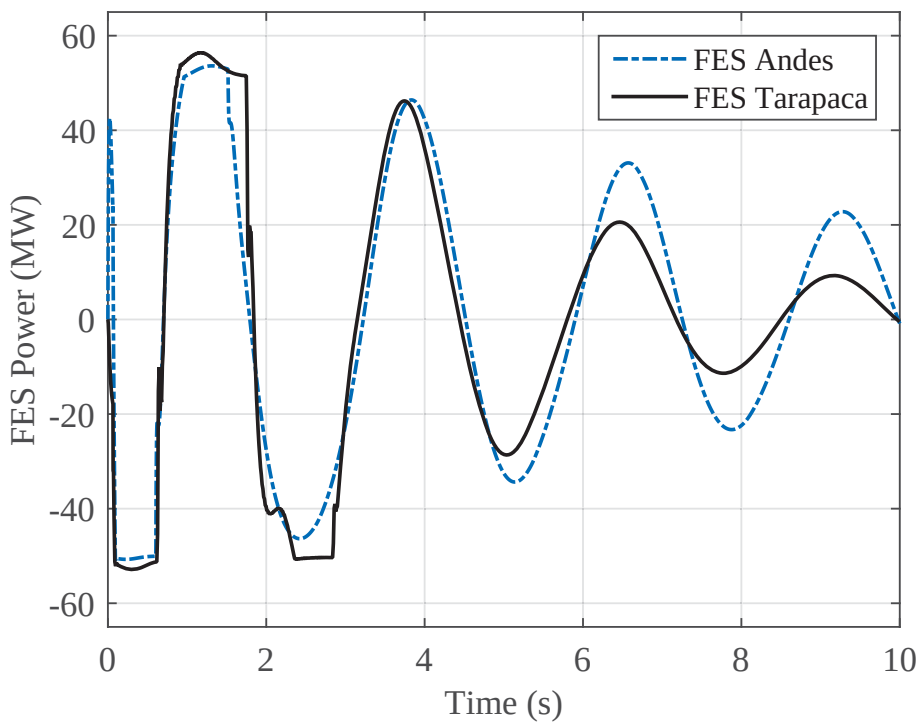

Figure 2.9: FES power after a 64 [ms] short circuit in Crucero

2.5 Summary

A comprehensive electro-mechanical model of a FES plant proper for power system dynamic analysis is presented. FES units based on surface permanent magnet machines are considered with both unit- and plant-level controllers. While FES units are capable of providing regulation for minutes, the focus in this work is on transient support for primary frequency control and its impact on oscillation damping. The FES performance is evaluated on the operation of the NCIS-AIS for various scenarios of load and conventional/renewable generation. The impact of FES plant location on oscillation damping is explored. Location candidates are screened by using inter-area mode controllability. For verification and final selection, small-signal stability analysis and time-domain simulations are performed. The results reveal that there exists a pattern showing regions from low to high controllability which is not importantly altered by the operational conditions. This implies that the observed pattern is strongly related to the system physical characteristics and, thus, an optimal location for the deployment of ESS can be found. This attractive finding has the potential to lead to useful criteria for power system planning in regards to storage systems. Although the FES plant is controlled to provide primary frequency regulation, this work provides evidence that if the FES is properly located, the oscillation damping can be importantly increased. By installing the FES plant in the NCIS best location, the damping ratio of the inter-area mode is increased from 0.53% to 13.1%. Furthermore, the power transferred from the NCIS to the AIS may be even doubled while still having a damping ratio above 9%.

Chapter 3

Enabling utility-scale solar PV plants for electromechanical oscillation damping

This chapter presents a new control method to enable large-scale solar photovoltaic (PV) plants to damp electromechanical oscillations. The step-down modulation (SDM) control method, based on active power modulation, does not require curtailment as in other approaches. After an oscillation event is detected, the PV panel voltage is controlled to transiently deviate the power from the its maximum power point (MPP), this power margin is used to modulate active power until the oscillation event is mitigated. Then, the SDM control restores the PV power to its MPP, and it is reset to operate for the next event. The control design, panel voltage strategy and implementation is tested in the two-area system. A comparison of the SDM control with a curtailment-based PV damping control is also explored in a test case of the 179-bus WECC system with six large-scale PV plants, showing the great damping capability of the proposed method.

3.1 SMIB Step-down Modulation control

Consider a lossless single-machine infinite bus (SMIB) system with a PV solar plant connected to the terminal bus of the synchronous generator as shown in Figure 3.1.

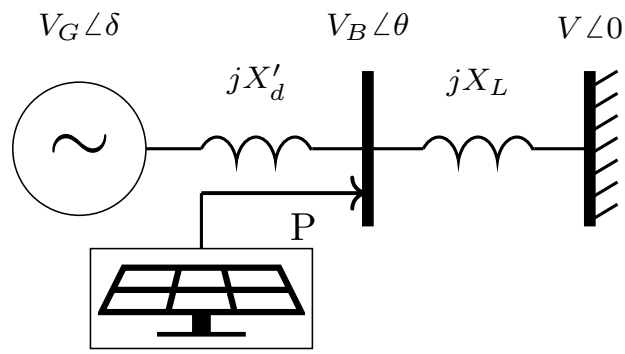

Figure 3.1: SMIB system with a PV solar plant.

Assume a classical model for the synchronous generator, with a constant induced voltage magnitude V_G behind the d-axis transient reactance X'_d. The transmission line has an impedance jX_L and the PV solar plant injects an active power $P = P_{max}$, where P_{max} is the maximum power extraction from the panel for a given solar irradiance and temperature. The system dynamics are governed by the following set of differential algebraic equations (DAE):

$$\frac{d\delta}{dt} = \omega_s(\omega - \omega_{ref}) \tag{3.1}$$

$$2H\frac{d\omega}{dt} = P_m - \frac{V_G V_B}{X'_d}\sin(\delta - \theta) \tag{3.2}$$

$$0 = -P + \frac{V_B V_G \sin(\theta - \delta)}{X'_d} + \frac{V_b V \sin(\theta)}{X_L} \tag{3.3}$$

$$0 = \frac{V_B^2 X'_d X_L}{(X'_d + X_L)} - \frac{V_B V_G \cos(\theta - \delta)}{X'_d} - \frac{V_B \cos(\theta)}{X_L} \tag{3.4}$$

where δ is the machine loading angle in rad, ω is the rotational speed in pu, $\omega_s = 120\pi$ is the synchronous speed in rad/s, H is the inertia constant in s and P_m is the fixed mechanical power in pu. Consider the following data taken from [108]: $H = 3.5$, $X'_d = 0.3$, $X_L = 0.65$ and also assume $P_m = 0.75$, $V = 1$, $V_G = 1$ and $P_{max} = 0.5$. Under this representation, the system behaves like an undamped harmonic oscillator. The phase portrait is shown in Figure 3.2 (a), where $\Delta\omega = \omega - \omega_e$ and $\Delta\delta = \delta - \delta_e$. Now consider the PV solar plant is shifted from its maximum power point such that its power injection is reduced to $P_0 = 0.7P_{max}$. As a result, the PV solar plant has sufficient power margin to provide power regulation without

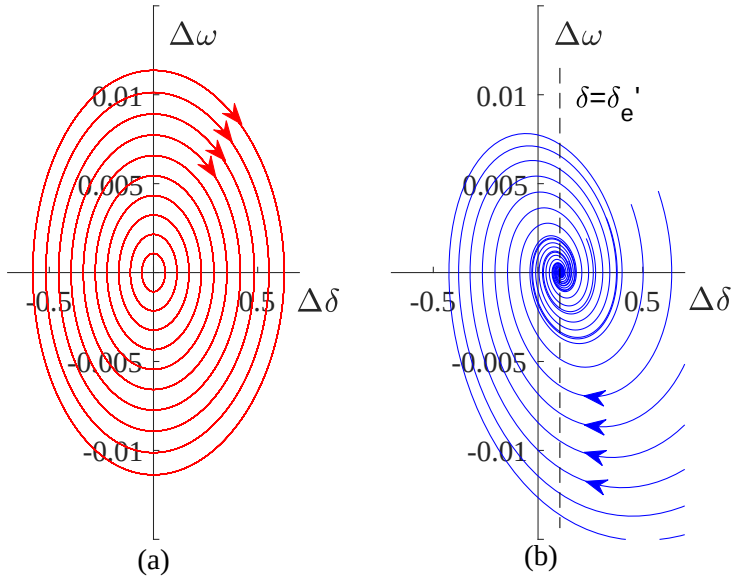

Figure 3.2: System phase portrait for PV solar plant injection equal to: (a) maximum power, and (b) reduced power and modulation.

reaching the limit. The power now can be modulated to react to speed deviations adding damping to the system and making the operating point asymptotically stable. Figure 3.2 (b) shows the phase portrait when the solar plant injects $P = P_0 + K_D(\omega - 1)$. As $P_0 = 0.7P_{max}$, the new equilibrium angle δ'_e is shifted to the right.

By combining both operating strategies displayed in Figure 3.2, a new damping control logic is proposed: transient step-down of the steady state power injection from the PV solar plant followed by power modulation to add damping to the system—this is feasible because the power step-down creates enough margin for power modulation. After the system is stabilized a recovery mode takes the system back to its original equilibrium point. The step-down modulation can be stated as a piece-wise function of the power:

$$P(t) = \begin{cases} P_{max}, & t \leq t_2 \\ P_{max} - P_{step} + P_{osc}, & t_2 \leq t < t_3 \\ P_{max} - P_{step} + P_{osc} + P_{rec}, & t \geq t_3 \end{cases} \tag{3.5}$$

with,

$$P_{step}(t) = K_R P_{max}(1 - e^{-(t-t_2)/\tau_1}) \tag{3.6}$$

$$P_{osc}(t) = -K_D(\omega - 1)(1 - e^{-(t-t_2)/\tau_2}) \tag{3.7}$$

$$P_{rec}(t) = K_R P_{max}(1 - e^{-(t-t_3)/\tau_3}) \tag{3.8}$$

where $K_R = 0.3$, $K_D = 30$, $\tau_1 = 0.01$, $\tau_2 = 0.1$ and $\tau_3 = 2$. Note that the control parameters K_R and K_D are designed to provide a desire amount of damping without reaching its limits. The times expressed in equation (3.5) are based on the following events:

- $t_0 \rightarrow t_1$: Short-circuit.
- t_1: Short-circuit is cleared.
- $t_2 \rightarrow t_3$: Step down modulation is enabled.
- t_3: Recovery mode is activated.

For simulation of the SMIB system, the times are chosen to be $t_0 = 1$, $t_1 = 1.1$, $t_2 = 1.3$ and $t_3 = 3$. Note that $t_2 > t_1$ includes an activation delay of 0.2 s related to the detection of the fault and oscillation. Figure 3.3 shows the state-space trajectories when applying the proposed step-down modulation. Note that the time constant τ_3 is chosen to be slow enough such the restoration of the PV power back to its maximum value does not excite undesired oscillations. Figure 3.4 shows the time domain evolution of the rotational speed of the synchronous generator and the PV power for both fixed power and step-down modulation approaches.

The step-down modulation control successfully damps the critical oscillation in less than 4 seconds and drives the system back to its original operation without the reappearance of the oscillation in less than 10 seconds. The convenience of transiently enabling a power margin for modulation can radically change the stability condition of the system, transforming the way PV systems participate in oscillation damping control, without requiring power curtailment.

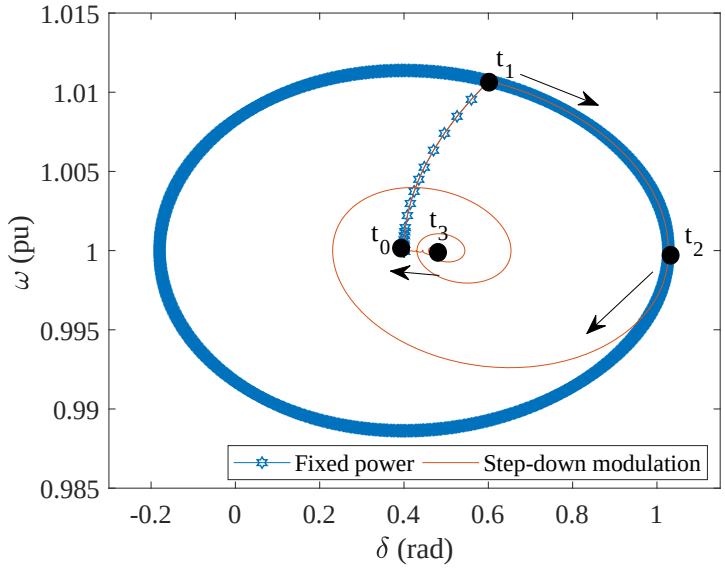

Figure 3.3: State-space trajectories for the proposed step-down modulation.

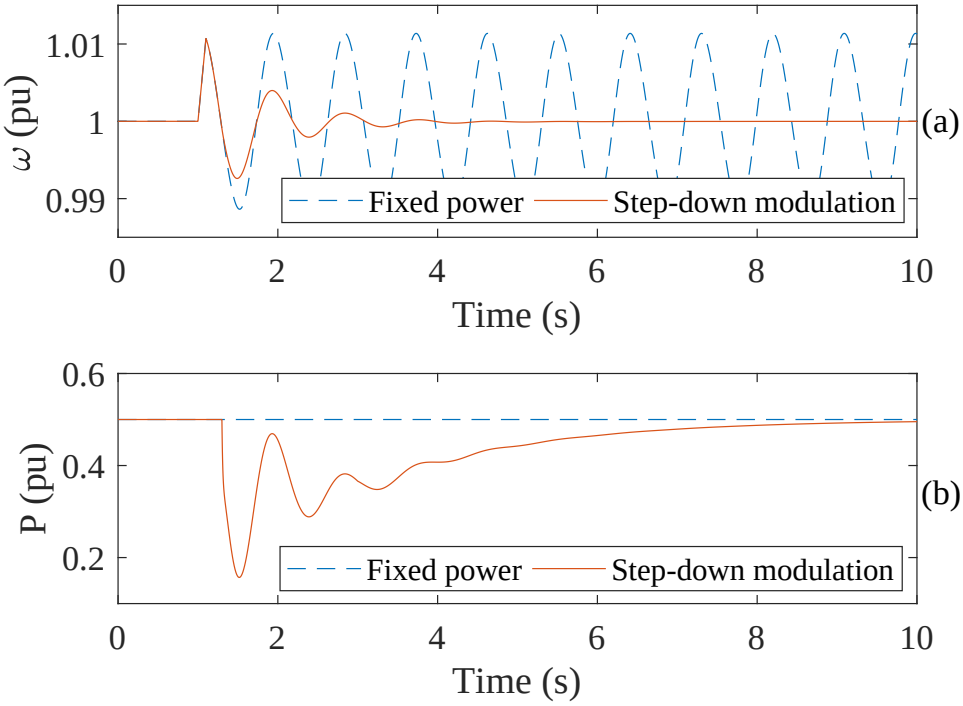

Figure 3.4: (a) Machine speed and (b) PV power.

3.2 PV-SDM implementation

3.2.1 PV model

Utility-scale PV plants consist of hundreds of PV arrays connected through power inverters and step-up transformers to a common coupling point to the grid. For power system analysis, it is customary to consider an aggregated model that represents the combined dynamic effect of all components within the PV plant, as this reduces the modeling and computational complexity. Consider an equivalent model with one PV array, one capacitor and one inverter connected directly to the grid. Figure 3.5 shows the aggregated model with the variables of interest.

3.2.2 PV power control

For a given fixed temperature and fixed solar irradiance, the PV panels behave according to their voltage and current characteristics [109]. This relationship is algebraic and determines the current and power output from the PV panels. Figure 3.6 displays the current i_{pv} and power P_{pv} for different values of the PV array voltage v_{dc} for a typical PV array.

A PV solar plant is generally operated to extract maximum power from the PV panels as this increases profit for electricity production; this is done by controlling the inverter to maintain the panel voltage at the maximum power point (v_{mpp}). Nevertheless, any value below the maximum power can be achieved by deviating from this operating voltage point. Take as an example the power reduction P_{step} shown in Figure 3.6 (b). The new reduced

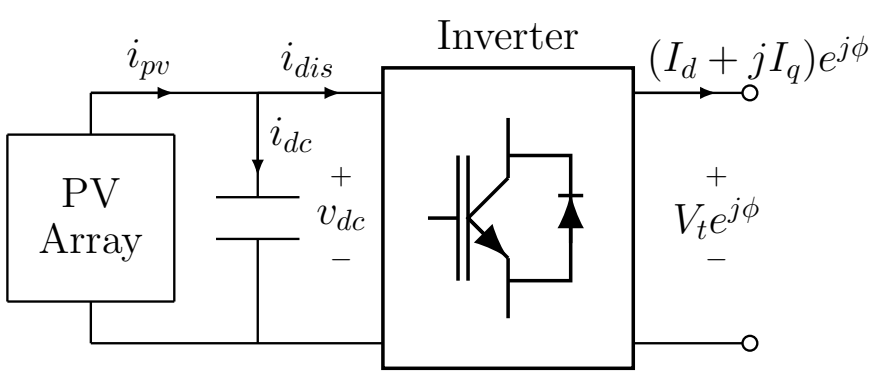

Figure 3.5: Aggregated PV system topology.

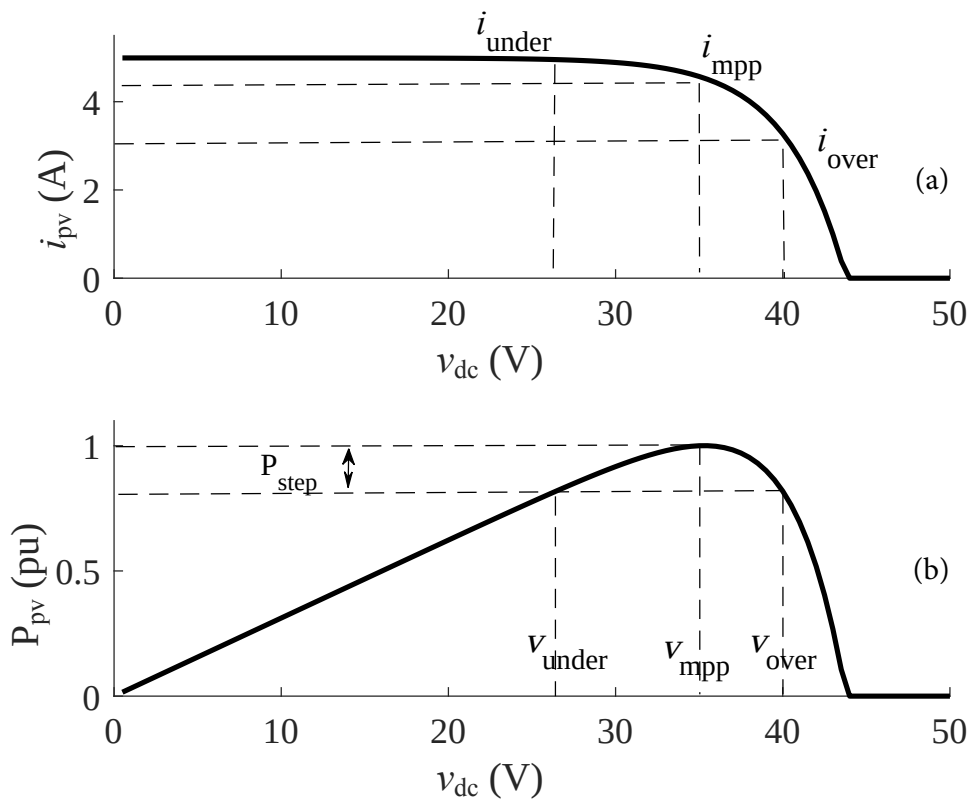

Figure 3.6: Typical PV panel characteristics: (a) current, and (b) power as a function of the PV voltage.

power can be obtained by two different approaches: (a) under voltage control or (b) over voltage control. In steady-state, both alternatives generate the same power output from the panels; however, these approaches behave differently during transient state because of the slope and control efforts associated with the corresponding panel voltage set point.

3.2.3 SDM implementation

The step-down modulation control is implemented by acting on the reference power P_{ref} in Figure 3.7. The reference power inputs a PI controller that determines an oscillation voltage signal v_{dc} that deviates from the maximum power point voltage reference. Note that in steady state $P_{ref} = P_{mpp}$ and $v_{osc} = 0$. The proposed control consists of three operation modes: pre-fault, activation and recovery mode. The different operation modes are activated by enabling different dynamics through the switches S_1, S_2 and S_3 shown in Figure 3.8.

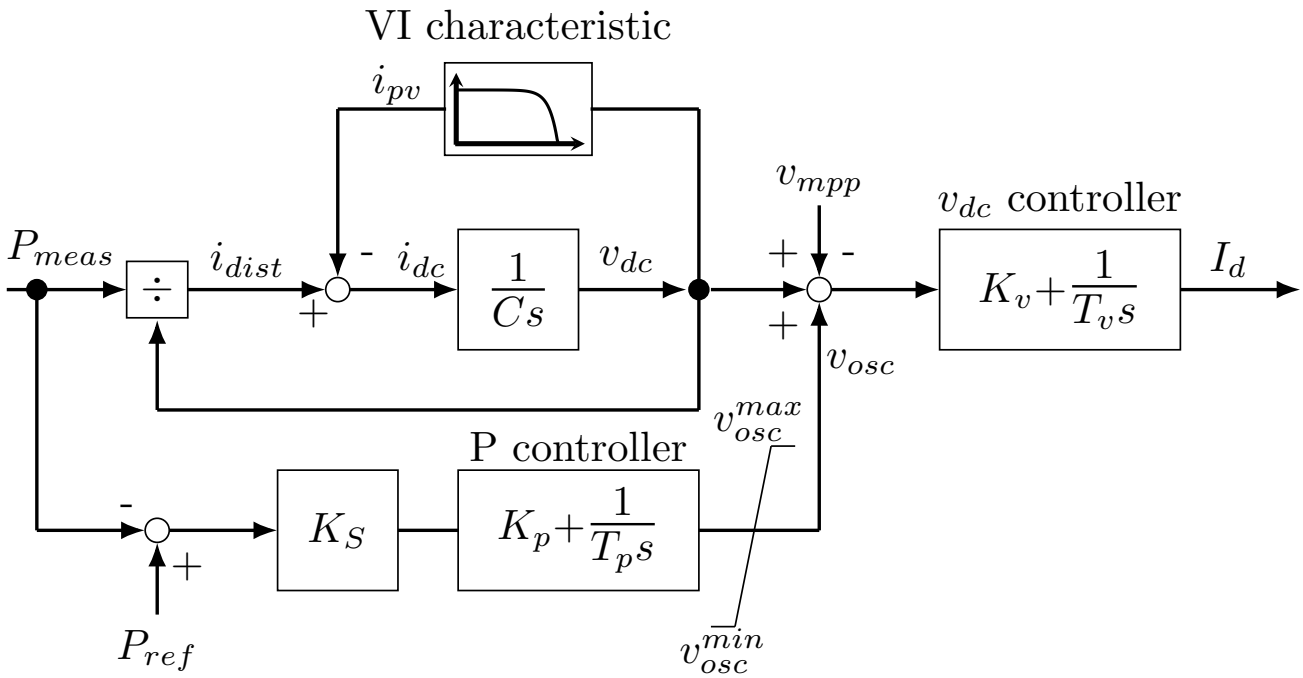

Figure 3.7: PV plant model for electromechanical simulations.

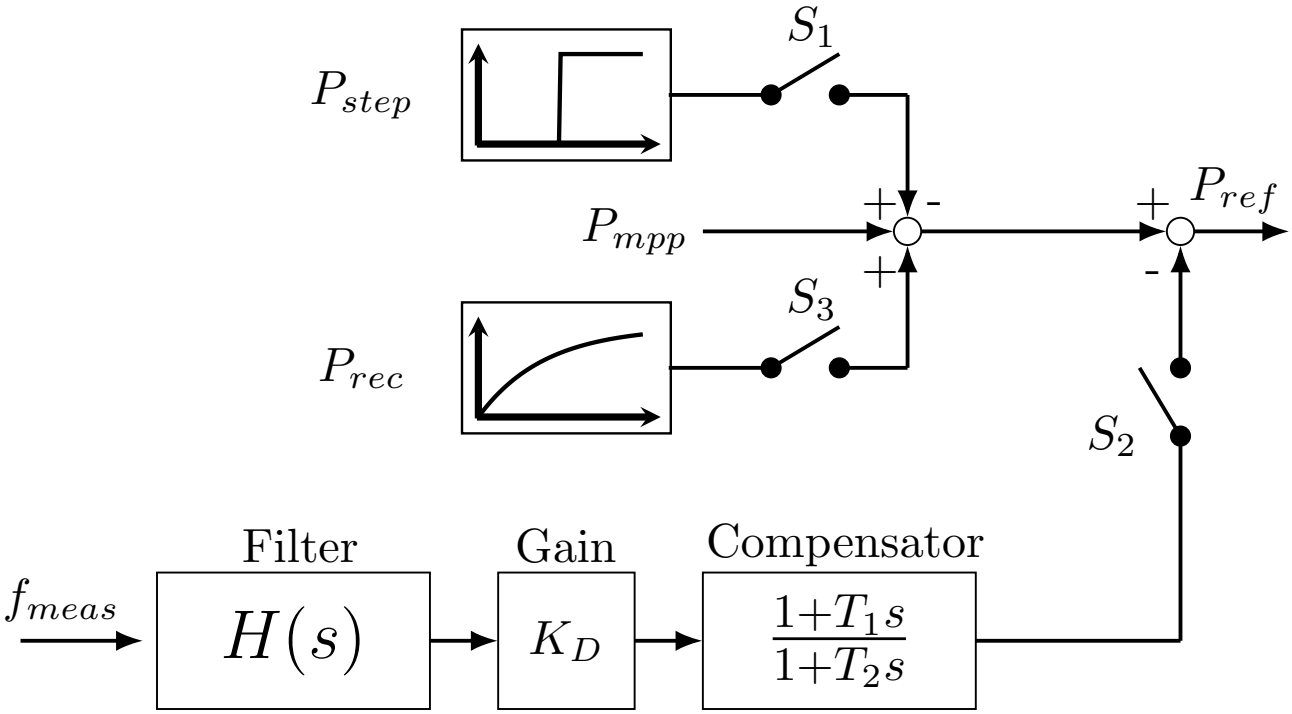

Figure 3.8: Block diagram of the step-down modulation control.

In pre-fault mode the three switches are in the open position and $P_{ref} = P_{mpp}$. When an event such as a short-circuit occurs in the system, the oscillation detection module detects the oscillation by measuring local frequency and comparing it to a positive threshold. The detection works only for an creasing frequency to avoid miss-operation during frequency excursions, which can worsen the frequency excursion by stepping-down the PV power. After an oscillation is detected the control enables the activation mode by closing S_1, this adds a fast step reduction in the power reference that creates enough margin to modulate but without compromising the stability of the system. The power imbalance as result of the step reduction should be small compared to the size and inertia of the system to avoid collateral large frequency excursions. After some time τ_1 when the PV power has reached the new reference value, S_2 is activated to enable the damping control. The damping control loop consists of a filter that discards low and high frequency components—if needed—of the a local frequency measurement, a gain and a phase-lead compensator. When the oscillation is damped after some time τ_2, the control enables the recovery mode, and S_3 is set to the close position. The recovery mode adds an additional signal to the power reference that compensates for the initial step reduction. The dynamic evolution of P_{rec} is slow such that oscillations are not excited during the process of restoring the PV system to its maximum power. A first order transfer function is used for the recovery. After some time τ_3 larger than the recovery time, all the switches $S_i, \forall i \in \{1, 2, 3\}$ and time counters $t_i, \forall i \in \{1, 2, 3\}$ are reset to pre-fault mode. Figure 3.9 summarizes the proposed logic for switching sequence between operation modes.

3.3 Case study

3.3.1 Two-area system

The two-area system in [108] is used to validate the proposed SDM control for a 100 MW PV power plant. Simulations are carried out in DigSILENT PowerFactory using a 6-th order model for the synchronous generators with IEEE Type AC4A Excitation System and IEEE Standard Governor model. Power system stabilizers are not incorporated to highlight the

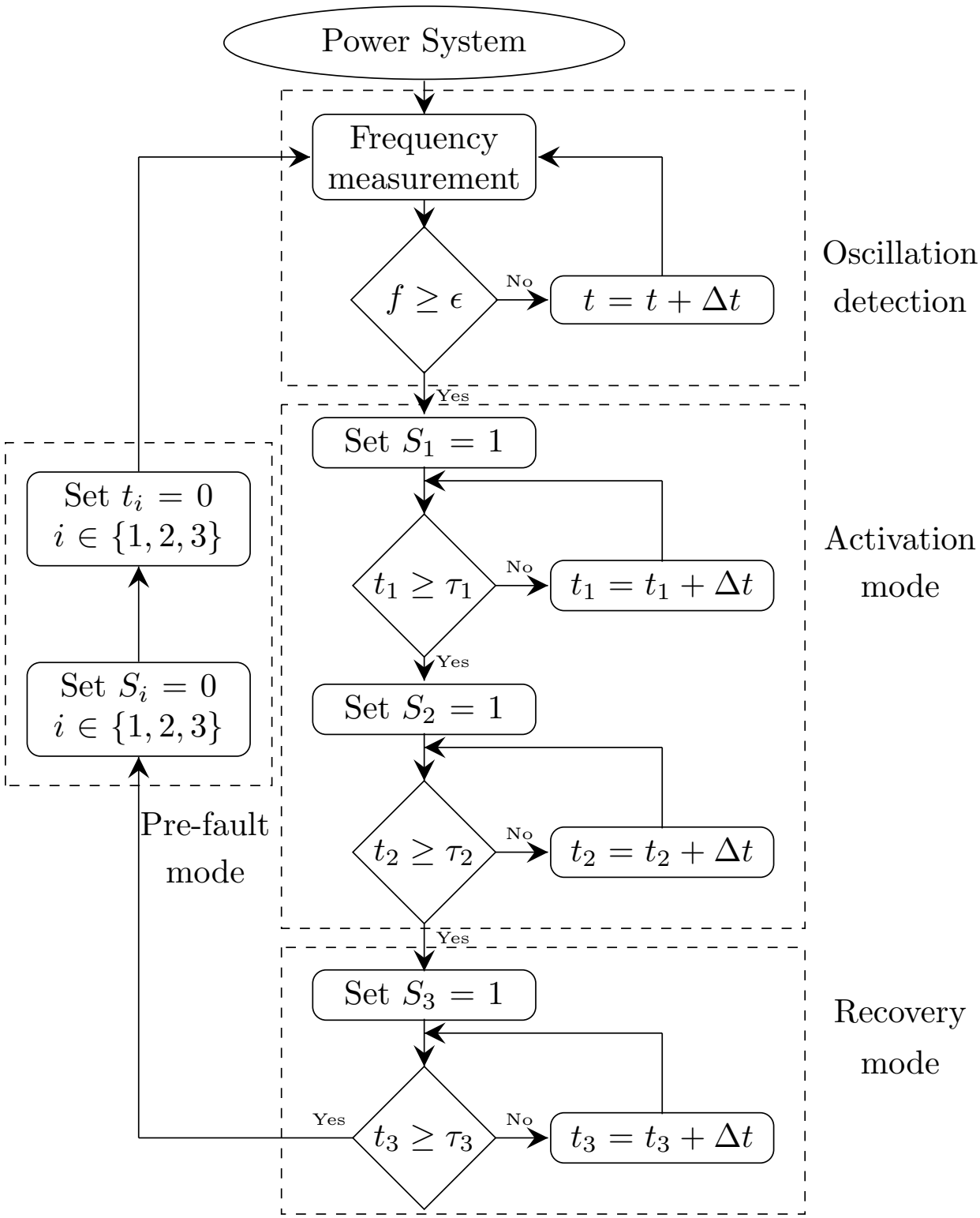

Figure 3.9: Flow chart calculation for the switches.

benefits of the SDM PV control. The PV panel characteristics and parameters are taken from the Software library [110] with 20 series modules and 28000 Parallel modules. Figure 3.10 shows the system topology, generators inertia, load, generation and location of the 100 MW PV plant. The original system exhibits a poorly damped inter-area oscillation between generators G1&G2 and G3&G4 with a frequency of 0.63 Hz and a damping ratio of 2.8%. The following subsections analyze the dynamic performance improvement achieved by different SDM variations, and the limitations of a typical reduced PV model when controlling active power for the SDM control.

Filter and voltage strategy comparison

The SDM control in Figure 3.8 can be customized to modulate the panel voltage with either under v_{mpp} or over v_{mpp} control strategy. Moreover, the control can be tailored for the particular system by designing an appropriate filter for the input signal. This filter is the particular importance when measuring frequency at the PV terminal bus, because the step-wise reduction in the PV power output creates an additional frequency error that is not part of the oscillation. This frequency error needs to be filtered out in order to properly stabilize the system. For comparison two filters are analyzed: a washout filter with time constant of 10 s and a second order Butterworth bandpass filter with cut-off frequencies of 2 and 6 rad/s (0.3 and 1 Hz). The performance improvement is tested in modal analysis—by linearazing the power system equations after stepping down the PV power from rated power to 70% without recovery. Table 3.1 shows the damping ratio of the inter-area mode obtained with SDM control for different filter and panel voltage strategy. Note that for both filters the over v_{mpp} voltage strategy provides better results achieving a maximum displacement of the

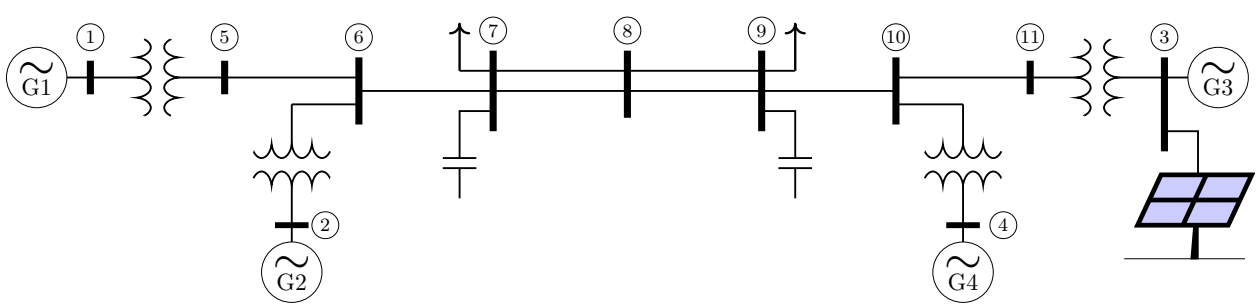

Figure 3.10: Two-area system with PV plant.

Table 3.1: Performance comparison for inter-area mode.

Filter	Voltage strategy	Damping ratio (%)
-	-	$\epsilon_0 = 2.8$
Butterworth	**over v_{mpp}**	$\boldsymbol{\epsilon = 11.2}$
Butterworth	under v_{mpp}	$\epsilon = 6.7$
Washout	over v_{mpp}	$\epsilon = 8.8$
Washout	under v_{mpp}	$\epsilon = 7.1$

inter-area mode from 2.8% to 11.2% in the case with the Butterworth filter. This occurs because of the PV voltage and power characteristic shown in Figure 3.6. The power and voltage relationship is steeper in the right side of the maximum power point, which makes the over v_{mpp} control more sensitive, requiring smaller variations in voltage to modulate the same variation in power.

Regarding the filter selection, the Butterworth filter shows superior improvement because its narrower frequency band and flat response. This characteristic allows SDM control to react exclusively to the oscillation signal, while the washout filter transiently provides a reaction to the artificial stationary frequency error worsening the damping performance and increasing the risk of saturation. Despite the benefit of using the Butterworth filter, its application needs to be studied for the particular system of interest, because it can produce a negative effect on modes with frequency close to the target mode.

The SDM PV control is tested in dynamic simulation for a 100 ms short-circuit at $t = 1$ in one of the transmission lines between bus 7 and 8. The positive dead band for the oscillation detection module is set to 40 mHz, the activation time is $t_1 = 40$ ms, the restoration time is $t_2 = 5$ and the reset time is $t_3 = 30$. The time constant of the slow recovery signal is set to 2 s. Figure 3.11 (a) shows the panel voltage and power for both voltage strategies using the Butterworth filter. Note that for the under v_{mpp} strategy the voltage changes up 300 V, while the over v_{mpp} strategy only requires 100 V to modulate the power. Moreover, in Figure 3.11 (b) the over v_{mpp} strategy is more effective even with smaller power modulations. Figure 3.12 shows the machine speeds for both voltage strategies using the Butterworth filter. The time domain simulation shows that both SDM voltage strategies successfully provide better damping than the system without PV control. For the over v_{mpp} control strategy in Figure

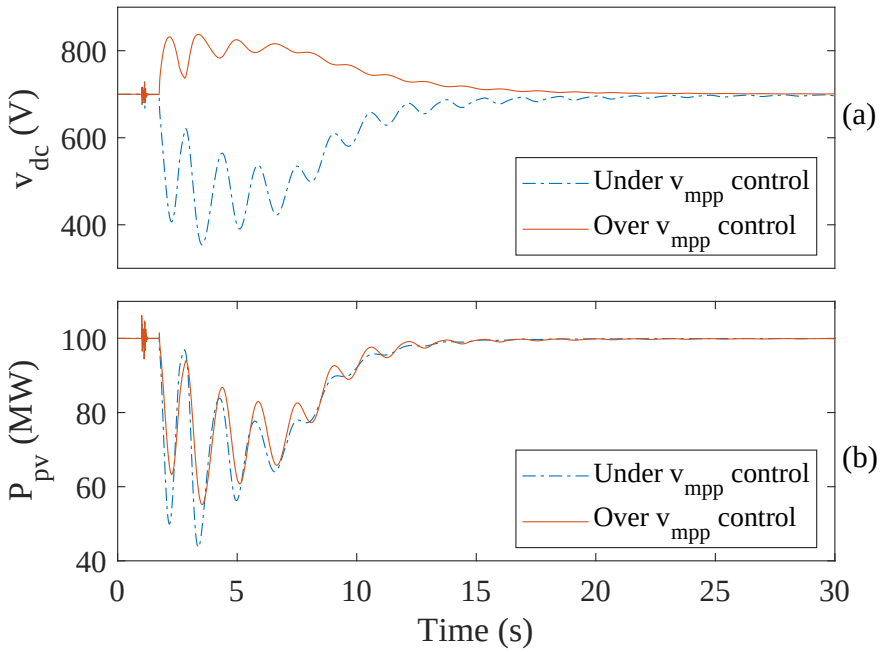

Figure 3.11: (a) Panel voltage and (b) PV output power for both voltage control strategies.

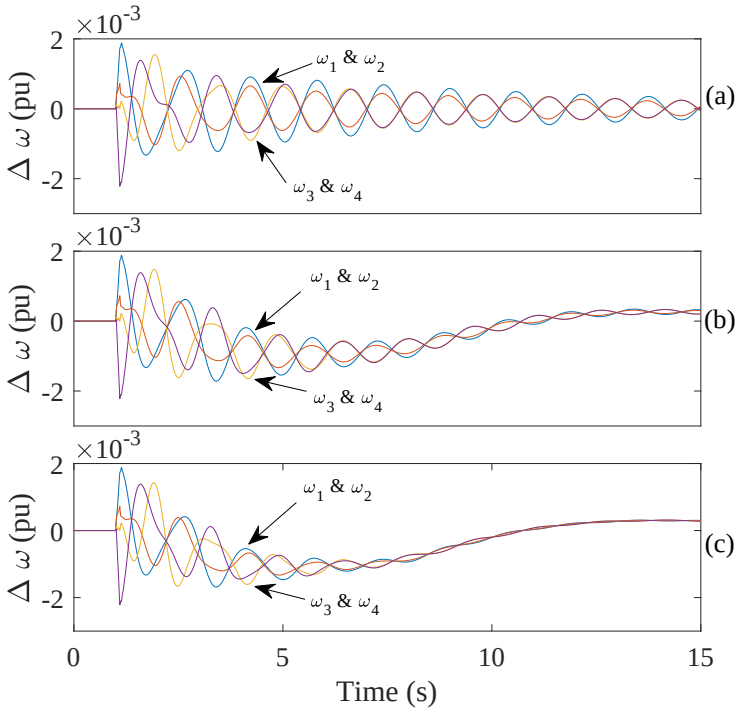

Figure 3.12: Speeds comparison: (a) No control, (b) SDM with under voltage strategy and (c) SDM with over voltage strategy.

3.12 the oscillation between G1&G2 and G3&G4 is stabilized in less than 10 s and recovered within 15 mHz from nominal value only after 15 s.

Limitations of WECC PV model for SDM control

The WECC PV model is a generic Photovoltaic system model developed by the Renewable Energy Modeling Task Force within the Western Electricity Coordinating Council [111]. The dynamic models in WECC PV model have been implemented by multiple commercial software vendors and experimentally tested to represent the power flow and dynamic behavior of large PV plants in the transmission system. However, as it is mentioned by its developers, the active power control module is still experimental and more research needs to be done. Consider the implementation of the SDM control in the WECC PV model. The power reference P_{ref} in Figure 3.8 passes through a first-order low-pass filter that determines the current that is injected to the grid. Assume the control sets a low limit for the power reference of 10 MW and the time constant of the first-order low-pass filter is adjusted to match the dynamic behavior or the PV panel model for under v_{mpp} voltage strategy. Figure 3.13 (a) shows the modulated PV power for the panel and Wecc model after a 130 ms short-circuit in the tie-line between G1&G2 and G3&G4. The SDM control implemented in the WECC PV model successfully match the performance of the SDM PV panel mode, achieving an improvement o the inter-area mode to 6.6%, similar to the 6.7% obtained with the panel model. Now consider the same fault, but when the solar radiation is such that the maximum power point of the PV panels is 60 MW. Figure 3.13 (b) shows the modulated PV power for the SDM control implemented in both models. Note that the panel model shows a saturated behavior and the WECC model dynamics are less accurate when the solar radiation is lower. This occurs because the panel voltage limit is reached, which is not modeled in the WECC PV model. Moreover, while the panel voltage limit is fixed, the power for which that voltage is reached depends on the solar radiation. Table 3.2 shows the variable minimum power for different maximum power point values. The results obtained show the limitation of the WECC PV model when controlling active power for SDM control. For a better characterization, without increasing the model complexity, a variable power limit needs to be incorporated to the model.

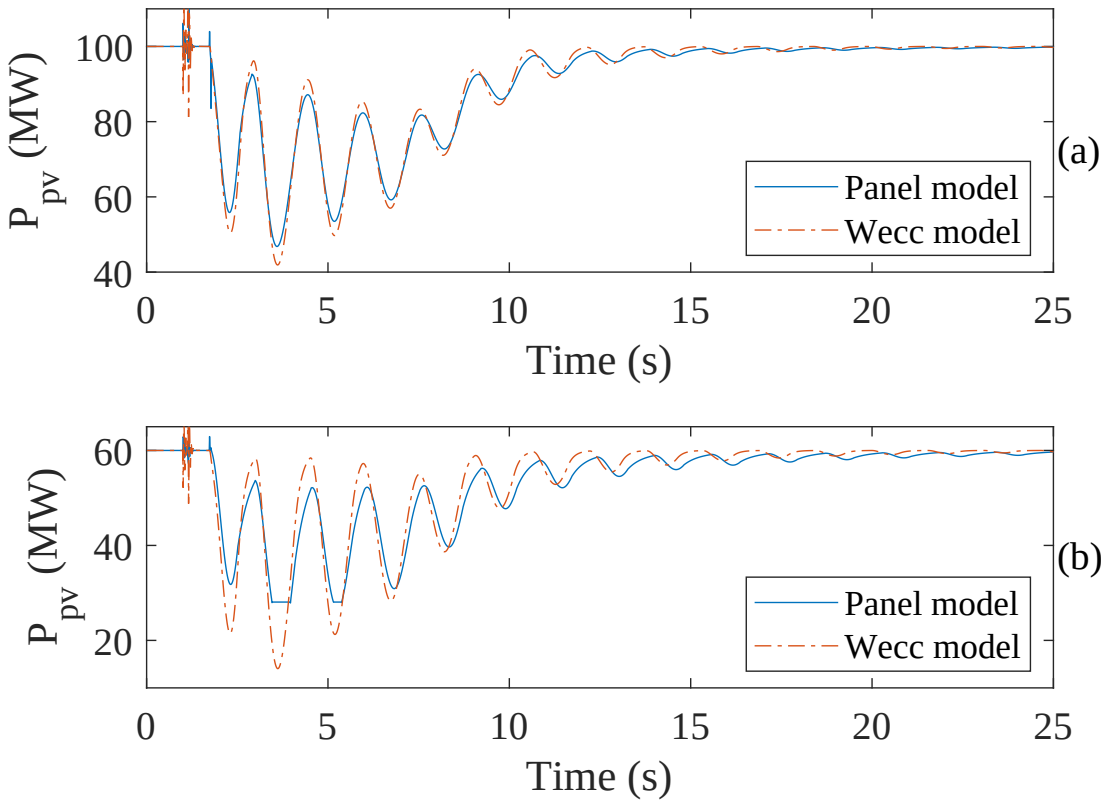

Figure 3.13: Model comparison for different radiation level: (a) $P_{mpp} = 100$ MW, (b) $P_{mpp} = 60$ MW.

Table 3.2: Power limit for different radiation levels.

Min Voltage (V)	MMP Power (MW)	Min Power (MW)
300	30	14
300	60	30
300	80	38
300	100	47

3.3.2 WECC system

The performance of the proposed SDM PV control is investigated in a test case of the wNAPS using the 179-bus WECC system. The network data and dynamic parameters are taken from [112]. Six large-scale 1100 MW PV plants are incorporated to the system. Note that this large plants represent the effect of aggregated smaller plants as well as future large-size plants that are already in study for the real system. Figure 3.14 shows the system topology and location of PV plants. For the scenario of analysis the solar radiation is such that in steady state the PV plants injects $P_{mpp} = 500$ MW. The system without PV has several inter-area modes with critical dmaping ratio between 10% and 4%,with one critical mode with 4.8% damping ratio. The SDM is set for a 10% power step reduction, washout filter—to avoid negative effect on neighboring modes—and over v_{mpp} control strategy. Figure 3.15 shows the eigenvalue plot for the case without PV control and with SDM PV control when all PV plants are activated.

The proposed SDM PV control greatly improves the small-signal stability of the system. By only modulating power under a small portion of the maximum power point, several critical modes are displaced to the left side of the complex plane. Some inter-area modes increase their damping ratio more than twice their original values and the most critical mode is changed from 4.8% to 7%. The control is now tested in time domain simulations for a 100 ms short-circuit at the transmission line between bus 138 and 141. The positive dead band is set to 40 mHz, the activation time is 40 ms, the recovery time is 10 s with a time constant for the slow recovery of 10 s and a reset time of 60 s. Furthermore, the SDM PV control is compared with a PV damping control (DC) proposed in [52] that uses power curtailment to allow a positive power margin for modulation. Figure 3.16 and 3.17 show the dynamic evolution of the speed of SG10 and PV power injection of the activated PV plants during the oscillation and recovery respectively. The results in Figure 3.16 show how the SDM PV control effectively damps the electromechanical oscillations in less than 10 s. Moreover, the performance of the SDM control closely resemble the performance of the curtailment DC, which is used as a benchmark for its perfect modulation capability created by the curtailment. Nevertheless, the cost of curtailment is high and undesired. Note that

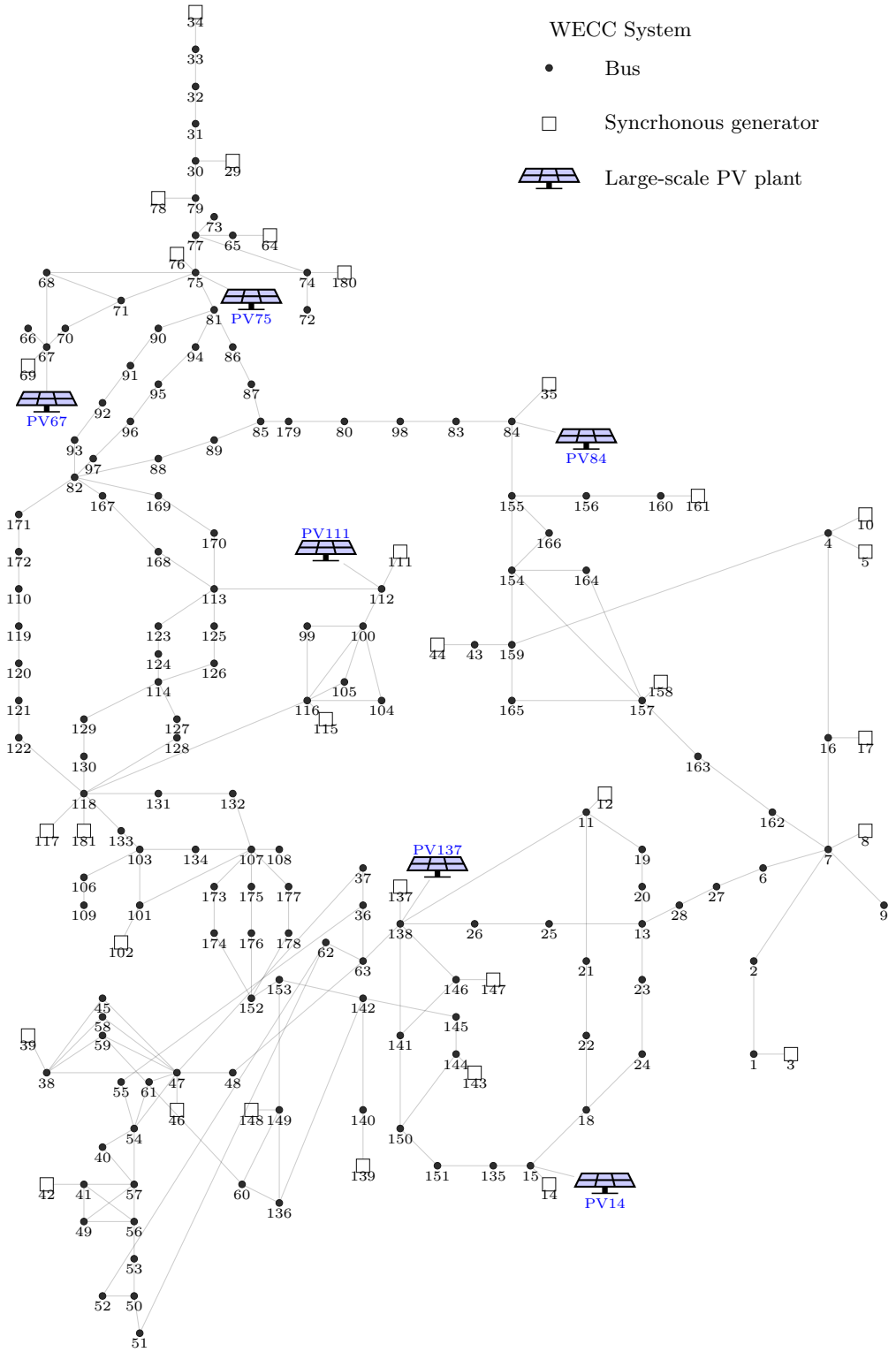

Figure 3.14: WECC system with utility-scale PV generation.

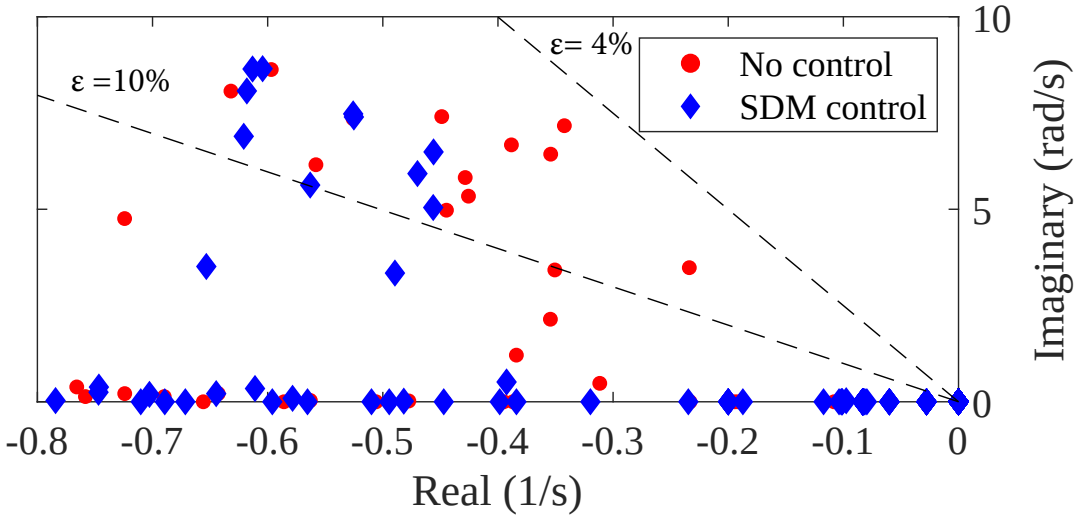

Figure 3.15: Eigenvalues of WECC system.

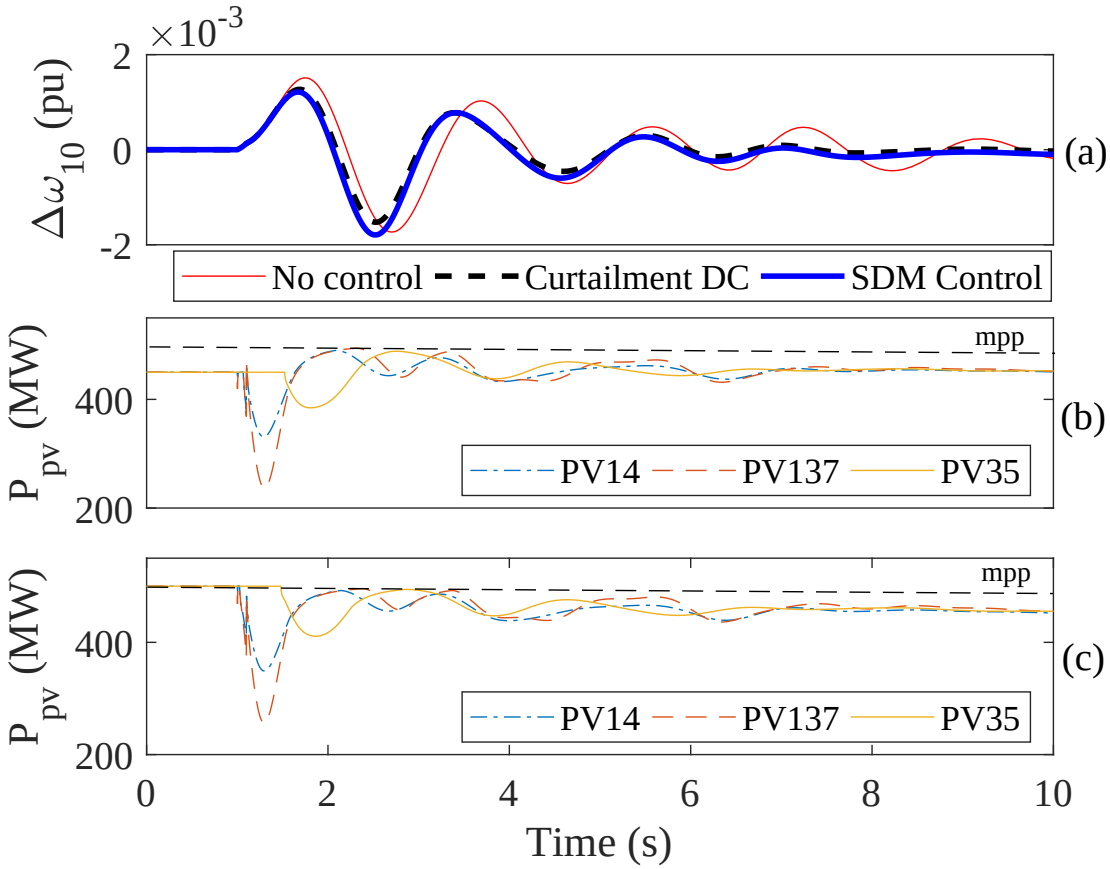

Figure 3.16: Control performance during oscillation: (a) Machine speed and (b) PV power injection for curtailment DC and (c) Power injection for SDM control.

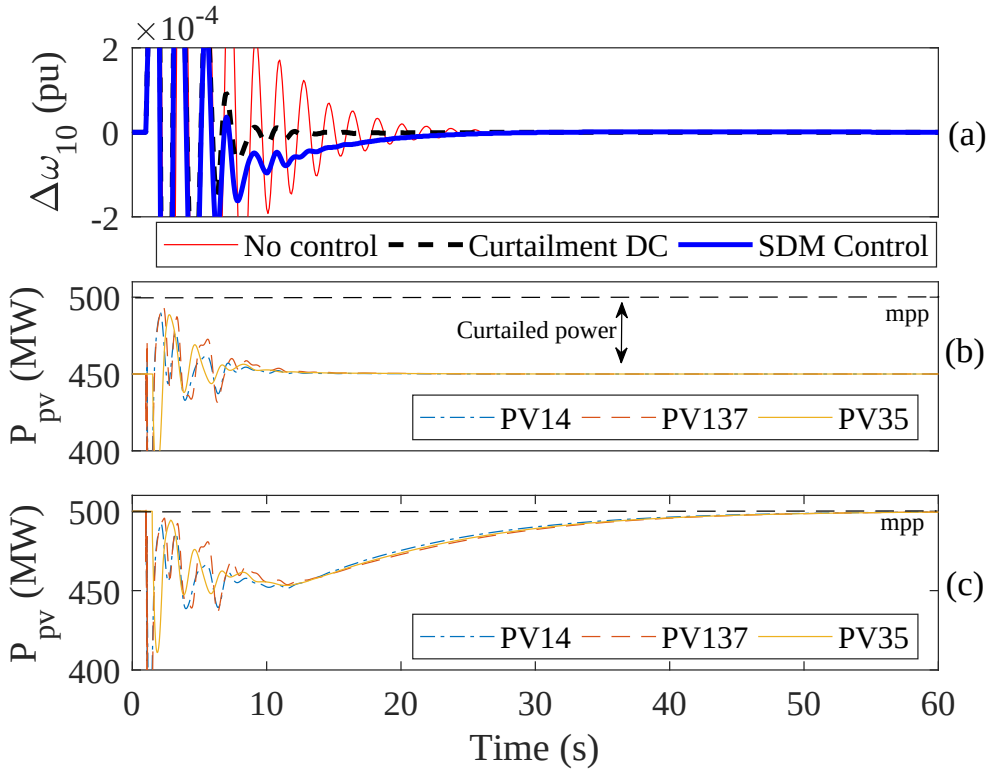

Figure 3.17: Control performance during recovery: (a) Machine speed and (b) PV power injection for curtailment DC and (c) Power injection for SDM control.

although only 3 PV plants are activated to support the oscillation control with SDM, the curtailment DC requires the six PV plants to maintain a power margin below its maximum power point. Figure 3.17 shows the same variables during the in a longer time window to exhibit the behavior during the recovery mode. The SDM control quickly drives the PV generation back to its maximum power point, stabilizing the system without the negative effects of curtailment such as increasing system operation costs and generation-related carbon emissions [54].

3.4 Summary

This chapter proposes a new method to enable utility-scale PV plants for modulating active power in DC. The approach allows the PV plant to operate at their maximum power point, changing its power output only when an oscillation event is detected. By controlling the PV panel voltage, the power is first stepped down to transiently create a margin, and then

modulated around this new equilibrium point. Once the oscillation is stabilized, the PV power is restored to its maximum power value—given by the solar radiation—and the control is reset in preparation for the next oscillation event. The performance of the SDM control for under v_{mpp} and over v_{mpp} panel voltage control is tested in the two-area system. The tests show the importance of the voltage-power characteristic of the panel, which provides a more sensitive and effective control in the right-side of the maximum power. Similarly, the filter selection becomes crucial for the performance of the SDM control. The performance is improved by filtering out frequencies exogenous to the electromechanical oscillations, which are induced by the change in the equilibrium point. Additionally, the effect of variable power limits in SDM control using the WECC PV system model is discussed and illustrated with the panel model used in this paper. The results suggest that the WECC PV system model can be improved to more accurate represent the PV plant dynamics without increasing its model complexity. Finally, the SDM control is tested in the WECC 179-bus system and compared with a PV DC that requires curtailment. The simulations show that the SDM control successfully damps the inter-area oscillations with similar performance to the curtailment-base DC, but without the undesired effects of curtailment.

Part II

Performance evaluation and coordination

Chapter 4

Dynamic performance index

This chapter describes a novel approach to analyze and control systems with multi-mode oscillation problems. Traditional single dominant mode analysis fails to provide effective control actions when several modes have similar low damping ratios. This work addresses this problem by considering all modes in the formulation of the system kinetic oscillation energy. The integral of energy over time defines the total action as a measure of dynamic performance, and its sensitivity allows comparing the performance of different actuators/locations in the system to select the most effective one to damp the oscillation energy.

4.1 Single machine infinite bus system

Consider the lossless SMIB system shown in Figure 4.1. Assume a classical model for the machine, i.e., constant induced voltage magnitude behind the d-axis transient reactance (X'_d). The state equations that governs the system dynamics are:

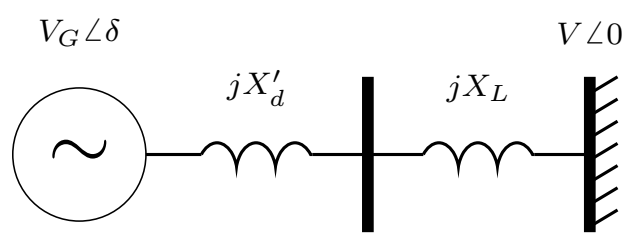

Figure 4.1: Single-machine infinite bus system.

$$\frac{d\delta}{dt} = \omega_s(\omega - \omega_{ref}) \tag{4.1}$$

$$2H\frac{d\omega}{dt} = P_m - K_D(\omega - \omega_{ref}) - K_S \sin(\delta) \tag{4.2}$$

where δ is the machine loading angle in rad, ω the rotational speed in pu, $\omega_s = 120\pi$ the synchronous speed in rad/s, $\omega_{ref} = 1$ is the reference speed in pu, H the inertia constant in s, K_D the damping torque coefficient in pu, $K_S = \frac{V_G V}{X'_d + X_L}$ the synchronizing torque coefficient in pu and P_m the fixed mechanical power in pu. Let $E(\delta, \omega)$ be the system energy function defined as [113]:

$$E(\delta, \omega) = \underbrace{H\omega_s\left(\omega - \omega_e\right)^2}_{E_k} + \underbrace{\left(-P_m\delta - K_S\cos(\delta)\right)\big|_{\delta_e}^{\delta}}_{E_u} \tag{4.3}$$

where E_k and E_u correspond to the kinetic energy and potential energy functions in pu, respectively, with $\omega_e = \omega_{ref} = 1$ pu and $\delta_e = \arcsin\left({}^{P_m}/_{K_S}\right)$ rad being the system equilibrium point. Note that $E(\delta, \omega) > 0 \; \forall \; \omega, \delta \in \mathbb{R} \setminus \{\omega = \omega_e \wedge \delta = \delta_e\}$ and $E(\delta, \omega) = 0$ for $\omega = \omega_e \wedge \delta = \delta_e$. Moreover, simulations have shown that during a fault, E_k has a more significant increase than E_u; right after the fault is cleared, E_k and E_u have a damped oscillatory exchange of energy. As a result, for a stable system, $E(\delta, \omega)$ can be bounded as,

$$0 \leq E(\delta(t), \omega(t)) \leq E(\delta(t_0), \omega(t_0)) \approx E_k(\omega(t_0)) \tag{4.4}$$

where t_0 is the time when the fault is cleared. Based on all the above and as $E(\omega, \delta) \to 0$ when $t \to \infty$, the system dynamic can be improved if E_k is compelled to converge faster to zero. A simplified analytical solution for E_k can be obtained using a linear estimation for the rotational speed as $\omega(t) = \omega_e + \Delta\omega(t)$. Assume $t_0 = 0$ (the fault clearing time). As shown in Appendix B, the explicit solution of the linearized system, $\Delta\omega(t)$, is given by:

$$\Delta\omega(t) = -\frac{\Delta\delta_0 e^{\lambda_x t}|\lambda|}{\omega_s \sin(\theta)}\sin(\lambda_y t) + \frac{\Delta\omega_0 e^{\lambda_x t}}{\sin(\theta)}\sin\left(\lambda_y t + \theta\right) \tag{4.5}$$

where $\lambda = \lambda_x + j\lambda_y$, $|\lambda| = \sqrt{\lambda_x^2 + \lambda_y^2}$, $\theta = \arctan\left({}^{\lambda_y}/_{\lambda_x}\right)$, and $\Delta\delta_0$ and $\Delta\omega_0$ are the linearized state variables when the fault is cleared (initial condition). Therefore, the kinetic energy function becomes $E_k(t) = H\omega_s(\omega(t) - \omega_e)^2 = H\omega_s\Delta\omega(t)^2$. From the observation of the states deviations right after a short circuit ${}^{\Delta\delta_0|\lambda|}/_{\omega_s} \ll \Delta\omega_0$, then, the following simplified expression is obtained:

$$E_k(t) \approx \frac{H\omega_s\Delta\omega_0^2 e^{2\lambda_x t}}{\sin(\theta)^2} \sin\left(\lambda_y t + \theta\right)^2 \tag{4.6}$$

Equation (4.6) is used to assess the system dynamic performance. This is done by defining the action $S(\tau)$ as the area under the oscillation kinetic energy curve from $t_0 = 0$ to some time τ,

$$\begin{aligned} S(\tau) &= \int_0^\tau E_k(t)dt \in \mathbb{R} \\ &= \int_0^\tau \frac{H\omega_s\Delta\omega_0^2 e^{2\lambda_x t}}{\sin(\theta)^2} \sin\left(\lambda_y t + \theta\right)^2 dt \quad = \frac{H\omega_s\Delta\omega_0^2}{4\lambda_x}\left(\frac{|\lambda|e^{2\lambda_x\tau}}{\lambda_y^2}\left(|\lambda| + \lambda_x\cos(2\lambda_y\tau + \theta)\right) - 1\right) \end{aligned}$$

Consider $K_D > 0 \implies \lambda_x < 0$, then the total action S_∞ in seconds is

$$S_\infty = \lim_{\tau\to\infty} S(\tau) = -\frac{H\omega_s\Delta\omega_0^2}{4\lambda_x} = \frac{H^2\omega_s\Delta\omega_0^2}{K_D} \tag{4.7}$$

The total action in equation 4.7 increases as the system becomes closer to instability. In fact, at the limit when $K_D \to 0$ ($\alpha \to 0$), then $S_\infty \to \infty$. Thus, the calculation of the total action can be used to assess and compare dynamic performance. Note that the same result in equation (4.7) is obtained in Appendix C by using the potential energy. This suggests that both kinetic and potential energy are equivalent in assessing the system dynamic performance.

Additionally, the dependency with the initial condition can be avoided by expressing the total action in per unit of the initial energy. Thus,

$$\frac{S_\infty}{E_k(0)} = \frac{H^2\omega_s\Delta\omega_0^2}{K_D}\frac{1}{H\omega_s\Delta\omega_0^2} = \frac{H}{K_D} \tag{4.8}$$

Consider $H = 5$, and $K_S = 2$. Let us examine the effect of the damping torque coefficient in the oscillation energy after an initial disturbance of $\Delta\omega_0 = 0.1$ by plotting the eigenvalues, oscillation energy and action for three different values: (a) $K_D = 20$, (b) $K_D = 10$ and (c) $K_D = 1$. Figure 4.2 shows the system eigenvalues. As the damping torque coefficient is decreased, the eigenvalue moves towards the imaginary axis, with minimal changes in frequency (λ_y).

Figure 4.3 shows the oscillation energy and action for cases (a), (b) and (c). The cases corresponds to the well damped, medium damped and critically damped oscillations with damping ratio σ of 11.5%, 5.8% and 0.6% respectively. For the first two cases, the oscillation energy is quickly damped after 4 seconds and the total action stabilizes at 0.25 and 0.5, which are also the values determined by equation (4.8), i.e., $S_\infty/E_k(0) = 5/20 = 0.25$ pu for case (a) and $S_\infty/E_k(0) = 5/10 = 0.2$ pu for case (b). In case (c) the reduction in the damping torque coefficient affects the oscillation energy by requiring extensive time to be damped, which results in a higher dissipation of energy over time and a higher total action $S_\infty/E_k(0) = 5/1 = 5$ pu.

The previous example shows how the total action is increased as the system becomes closer to instability. In fact, at the limit when $K_D \to 0$ ($\alpha \to 0$), then $S_\infty \to \infty$. Thus, the calculation of the total action can be used to assess and compare dynamic performance.

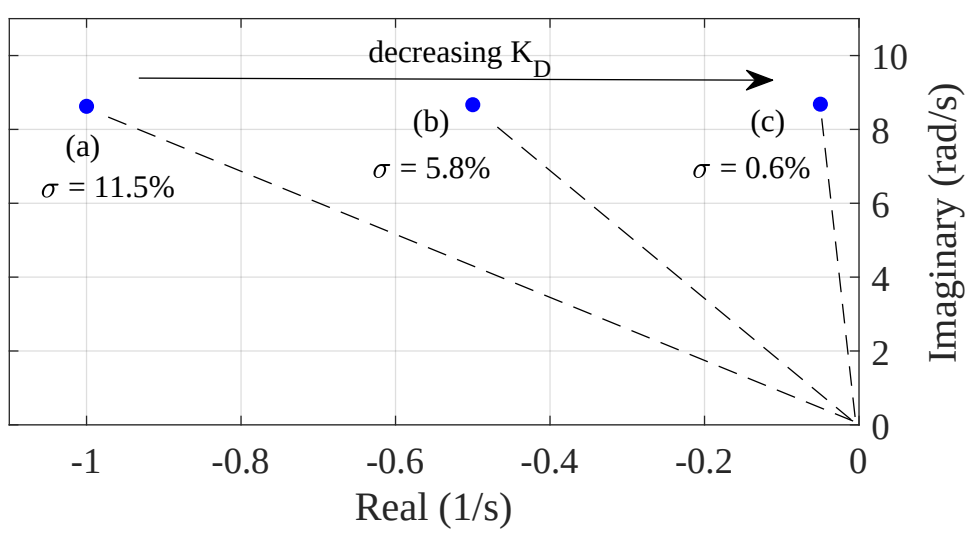

Figure 4.2: SMIB system eigenvalues for different values of K_D.

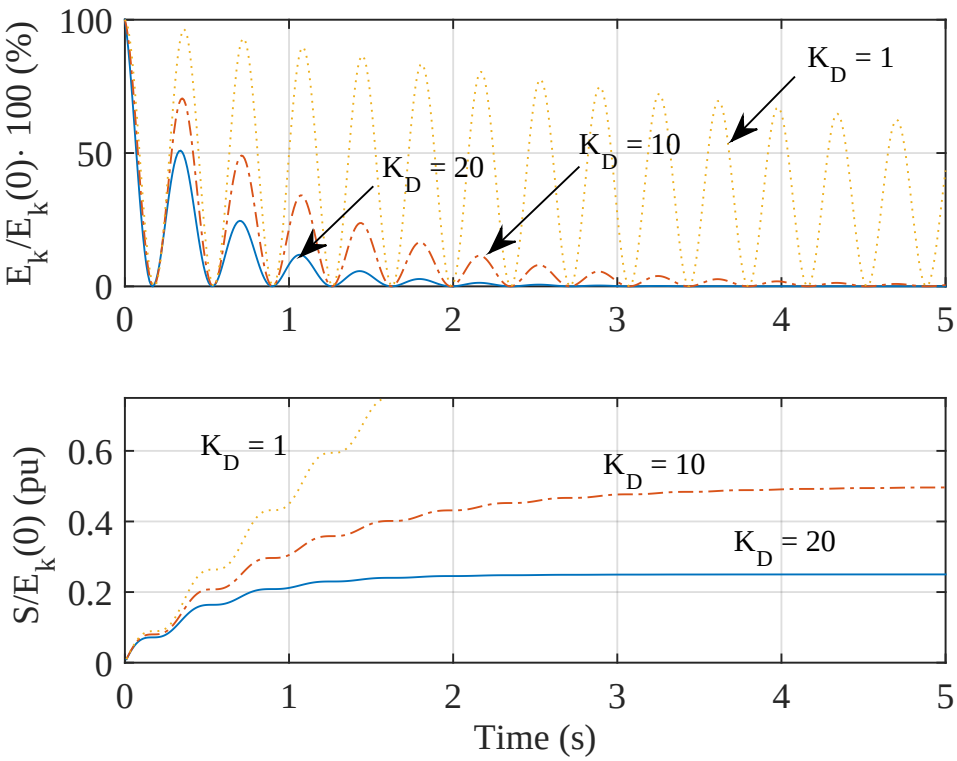

Figure 4.3: Oscillation energy and action for different values of K_D in the SMIB system.

4.2 Multi-machine systems

4.2.1 Oscillation energy and action

Consider the set of linearized power system equations with p synchronous generators and n total number of states:

$$\Delta\dot{x} = A\Delta x \tag{4.9}$$

By using the transformation $\Delta x = M\Delta z$, where $M = \{v_1, v_2, ...v_n\}$ is the matrix of right eigenvectors, the system equations can be decoupled as:

$$\Delta\dot{z} = \underbrace{M^{-1}AM}_{\Lambda}\Delta z = \Lambda\Delta z \tag{4.10}$$

Here $\Lambda = \text{diag}\{\lambda_i\}$, where λ_i is the i-th system eigenvalue. Thus, the solution of each state of the decoupled system can be easily written in terms of its corresponding eigenvalue:

$$\Delta z = e^{\Lambda t}\Delta z_0 \rightarrow \Delta z_i = e^{\lambda_i t}\Delta z_{0i} \in \mathbb{C}, \forall i \in \{1, ..., n\} \tag{4.11}$$

where $\Delta z_0 = [\Delta z_{01}, ..., \Delta z_{0i}, ..., \Delta z_{on}]^T = M^{-1}\Delta x_0$. The kinetic energy of the linearized system becomes:

$$E_k(t) = \sum_{j=1}^{p} H_j \omega_s \Delta\omega_j^2 = \Delta x^T H \omega_s \Delta x \tag{4.12}$$

$$= (M\Delta z)^T H \omega_s (M\Delta z) \tag{4.13}$$

$$= \frac{1}{2}\Delta z^T G \Delta z \in \mathbb{R} \tag{4.14}$$

where $\Delta\omega_j$ is the speed deviation of generator j in pu., H is the inertia matrix in s—with nonzero elements only in the diagonal terms $H_{jj} = H_j \; \forall \; j \in \Omega_\omega$, where Ω_ω is the set of speed indices of all synchronous generators. The transformed inertia matrix $G = 2M^T H \omega_s M$ is in general non diagonal and complex. Note that after a disturbance, the speed trajectories describe the oscillation energy defined by equation (4.14) such that $E_k(t) > 0 \quad \forall \; t$ and E_k is zero in steady state. Consider now the mathematical definition of action (S), which is typically represented by an integral over time and taken along the system trajectory [114]. This integral has units of (energy)·(time) and for our problem can be written as:

$$S(\tau) = \int_0^\tau E_k(t)dt = \int_0^\tau \frac{1}{2}(\Delta z^T G \Delta z)dt \in \mathbb{R} \tag{4.15}$$

$$= \int_0^\tau \frac{1}{2}(e^{\Lambda t}\Delta z_0)^T G (e^{\Lambda t}\Delta z_0)dt \tag{4.16}$$

$$= \frac{1}{2}\int_0^\tau \left(\sum_{j=1}^{n}\sum_{i=1}^{n} e^{(\lambda_i+\lambda_j)t} z_{0i} z_{0j} g_{ij} \right) dt \tag{4.17}$$

where z_{0i} is the i-th element of Δz_0 and g_{ij} is the entry in the i-th row and j-th column of G. The action evaluated at a fixed time τ becomes:

$$S(\tau) = \frac{1}{2}\sum_{j=1}^{n}\sum_{i=1}^{n}\frac{e^{(\lambda_i+\lambda_j)t}}{(\lambda_i+\lambda_j)}z_{0i}z_{0j}g_{ij}\Big|_0^{\tau} \tag{4.18}$$

Considering stable modes, the total action until the oscillations vanish is obtained as,

$$S_\infty = \lim_{\tau\to\infty} S(\tau) = -\frac{1}{2}\sum_{j=1}^{n}\sum_{i=1}^{n}\frac{z_{0i}z_{0j}g_{ij}}{(\lambda_i+\lambda_j)} \tag{4.19}$$

4.2.2 Total action sensitivity (TAS)

Assume that a damping control device is installed in the system. The dynamics of this controller are fast and can be represented as a proportional gain θ_k. Consider the analysis of the effect of the control gain θ_k in the total action, which is a measure of how quick the oscillation energy is damped. The sensitivity of the total action with respect to the control gain is expressed as:

$$\begin{aligned}\frac{\partial S_\infty}{\partial \theta_k} = &-\sum_{j=1}^{n}\sum_{i=1}^{n}\frac{z_{0j}g_{ij}}{(\lambda_i+\lambda_j)}\frac{\partial z_{0i}}{\partial \theta_k} - \sum_{j=1}^{n}\sum_{i=1}^{n}\frac{z_{0i}z_{0j}}{2(\lambda_i+\lambda_j)}\frac{\partial g_{ij}}{\partial \theta_k}\\ &+\sum_{j=1}^{n}\sum_{i=1}^{n}\frac{z_{0i}z_{0j}g_{ij}}{2(\lambda_i+\lambda_j)^2}\left(\frac{\partial \lambda_i}{\partial \theta_k}+\frac{\partial \lambda_j}{\partial \theta_k}\right)\end{aligned} \tag{4.20}$$

where $\partial z_{oi}/\partial\theta_k$ and $\partial g_{ij}/\partial\theta_k$ are the entries of the following vector and matrix, respectively:

$$\frac{\partial z_o}{\partial \theta_k} = \frac{\partial M^{-1}}{\partial \theta_k}x_0 \tag{4.21}$$

$$\frac{\partial G}{\partial \theta_k} = \frac{\partial M^T}{\partial \theta_k}JM + M^TJ\frac{\partial M}{\partial \theta_k} \tag{4.22}$$

Calculations of the eigenvector derivatives are obtained by solving a set of linear equations that are a function of the eigenvalues, their derivatives, the eigenvectors and the system matrix derivative [115]. Similarly, eigenvalue sensitivities can be calculated by means of the residue or equivalently using the concepts of mode controllability and mode observability

[5], [82]. For simplicity, equation (4.20) can be rearranged as a linear combination of the eigenvalue sensitivities plus one term that depends on the eigenvector sensitivities.

$$\frac{\partial S_\infty}{\partial \theta_k} = \alpha_k + \sum_{i=1}^{n} \beta_i \frac{\partial \lambda_i}{\partial \theta_k} \tag{4.23}$$

where $\alpha_k \in \mathbb{R}$ is the summation of the first two terms in equation (4.20) and the modal coefficients β_i are given by

$$\beta_i = \sum_{j=1}^{n} \frac{z_{0i} z_{0j} g_{ij}}{(\lambda_i + \lambda_j)^2} \tag{4.24}$$

Note that $\partial S_\infty / \partial \theta_k$ is a real number, although β_i and $\partial \lambda_i / \partial \theta_k$ are all complex quantities. As $E_k \geq 0 \quad \forall\, t$, the best dynamic performance, from an energy point of view, occurs when E_k quickly approaches to zero—which is equivalent to minimize the total action. Therefore, the control gain θ_k for which $\partial S_\infty / \partial \theta_k < 0$ and $|\partial S_\infty / \partial \theta_k|$ is maximum, provides the optimal control solution.

4.3 Simulation results and analysis

The IEEE 9-bus system and IEEE 39-bus systems are used for simulations. Models and parameters are obtained from the library in DIgSILENT PowerFactory. A Battery Energy Storage System (BESS) is used to provide oscillation damping. Only a control gain is considered in the closed loop. The location of this BESS is analyzed for each bus i at a time, and speed of the closest generator is used as feedback signal.

4.3.1 Single mode analysis versus oscillation energy analysis

The IEEE 9-bus test system in Figure 4.4 is studied to show the advantage of the TAS over the traditional single-mode eigenvalue sensitivity analysis. The system dynamics of the linearized model are dominated by two electromechanical modes: one local oscillation between Gen 2 and Gen 3 with an initial eigenvalue $\lambda_{23} = -0.027 + j13.4$, and one inter-area oscillation between Gen 1 and (Gen 2, Gen 3) with an initial eigenvalue $\lambda_{123} = -0.038 + j8.73$.

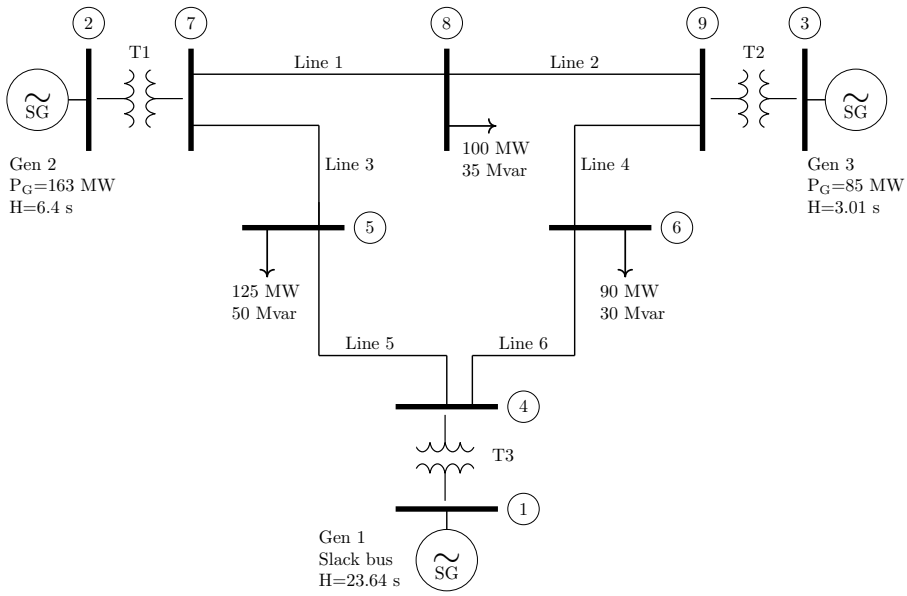

Figure 4.4: 3-machine, 9-bus system.

Note that both electromechanical modes have critical damping ratios of 0.19% and 0.43% respectively.

Traditional eigenvalue sensitivity analysis

The location of an equivalent 100 MW BESS is studied at buses 4, 7 and 9 using the speed of generators 1, 2 and 3 as feedback signal, respectively. For each case, the control gain θ_i is increased from 0 to 50 in steps of 5, and the displacement of the local and inter-area mode are analyzed. Figure 4.5 shows the eigenvalues displacement for an increasing control gain. A traditional approach would prioritize damping the inter-area oscillation, as both oscillations have low damping ratios and the inter-area oscillation involves more generators. Then, part (b) of the figure would be considered as the best case, i.e., increasing θ_7 displaces further to the left-side plane the inter-area mode. The eigenvalue sensitivity shown in Table 4.1 points out θ_7 as the most effective gain to control the inter-area oscillation as well, while θ_9 is more effective to control the local oscillation. Thus, from the point of view of eigenvalue sensitivity and each eigenvalue displacement, the prospective BESS location at bus 7 should be chosen to improve the system oscillations. However, as shown in the next subsection, this selection based on a single system eigenvalue is not always optimal.

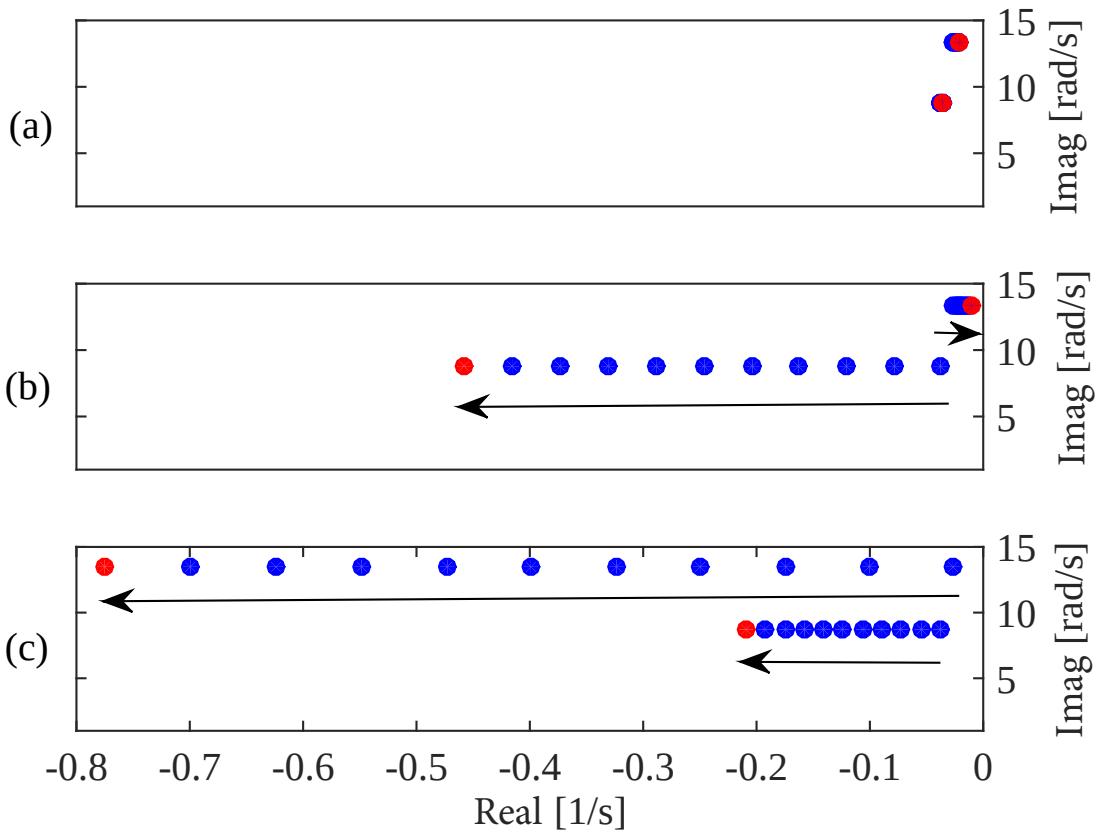

Figure 4.5: Eigenvalue plot of the IEEE 9-bus system for prospective locations of BESS by increasing control gain: (a) changing θ_4, (b) changing θ_7, (c) changing θ_9.

Table 4.1: Eigenvalue sensitivities.

	$\lvert\partial\lambda_i/\partial\theta_4\rvert$	$\lvert\partial\lambda_i/\partial\theta_7\rvert$	$\lvert\partial\lambda_i/\partial\theta_9\rvert$
λ_{23}	3.23×10^{-5}	9.59×10^{-5}	**0.0045**
λ_{123}	1.25×10^{-5}	**0.0025**	0.0010

Oscillation energy analysis

The proposed oscillation energy and TAS analysis considering all modes is performed to provide insight about which BESS location—or combination of BESS locations—should be employed. Table 4.2 shows the TAS for three different initial states disturbances $\Delta\omega_0 = (\Delta\omega_{01}, \Delta\omega_{02}, \Delta\omega_{03})$, where $\Delta\omega_{0j}$ denotes the initial speed deviation of machine j.

In order to verify the results obtained by the TAS analysis, time domain simulations are performed using the full set of nonlinear differential equations for each of the disturbances in Table 4.2. Figure 4.6 shows the system kinetic energy for each prospective BESS location at a time.

The results from figure 4.6 show agreement with those from Table 4.2. For the first and second disturbance in part (a) and (b) of the figure, the BESS located at bus 9 is more effective to damp the system kinetic energy while BESS located at bus 4 and 7 have marginal improvements. For the third disturbance shown in part (c) of the figure, the BESS located at bus 7 is the most effective to quickly drive the system to steady state. These differences occur because the disturbances excite modes in different proportions, aspect which is completely captured by the modal coefficients β_i in equation (4.23). To sum up, for some disturbances the single mode analysis fails to identify the best actuator/location, while the proposed approach is able to consider the combined effect of all eigenvalue displacements.

4.3.2 Application: IEEE 39-bus test system

The TAS analysis is applied in the IEEE 39-bus test system shown in Figure 4.7. The original inertia of generator G_1 is reduced to 30 s in a 100 MVA base to allow a more symmetric case. The dynamics of the system are described by the eigenvalues shown in Figure 4.8. There

Table 4.2: Total action sensitivities.

	$\partial S_\infty/\partial\theta_4$	$\partial S_\infty/\partial\theta_7$	$\partial S_\infty/\partial\theta_9$
$\Delta\omega_0^1 = (0.01, 0, -0.01)^T$	-2.151	-21.42	$\mathbf{-40.18}$
$\Delta\omega_0^2 = (0, 0.01, -0.01)^T$	-0.419	-8.158	$\mathbf{-57.56}$
$\Delta\omega_0^3 = (0.01, -0.01, 0)^T$	-4.364	$\mathbf{-42.63}$	-17.11

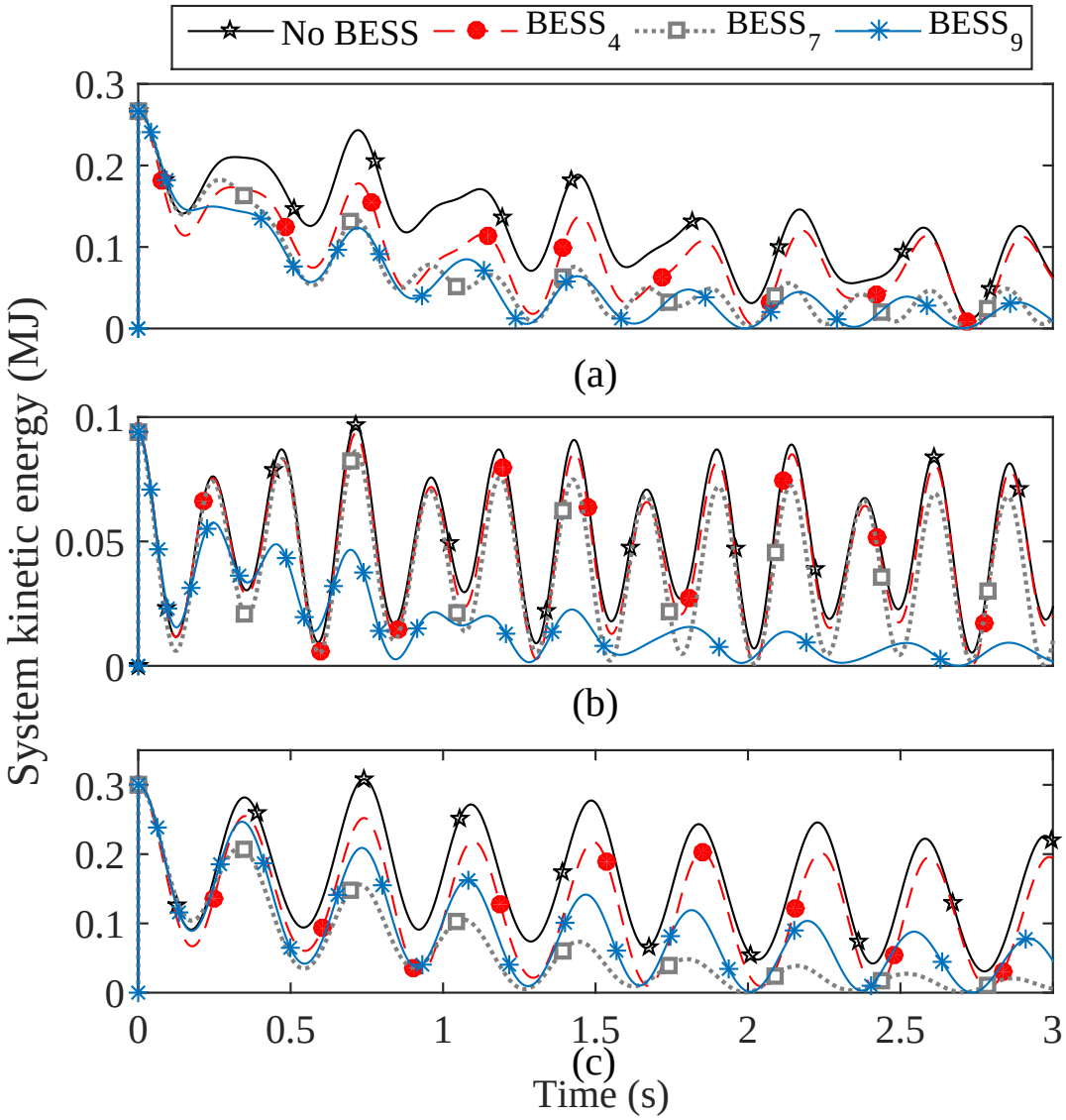

Figure 4.6: System kinetic energy for different initial disturbances and BESS locations: (a) $\Delta\omega_0^1$, (b) $\Delta\omega_0^2$, (c) $\Delta\omega_0^3$.

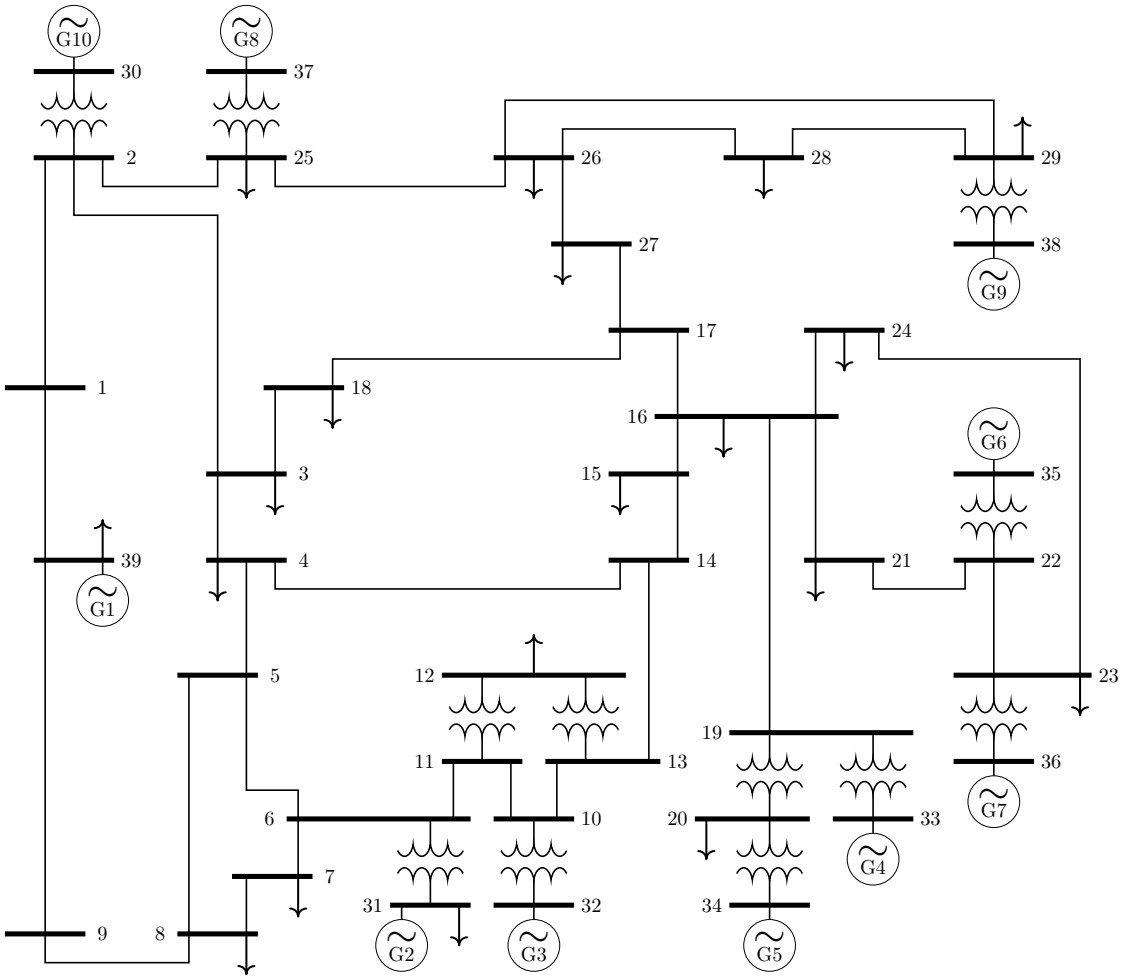

Figure 4.7: IEEE 39-bus test system.

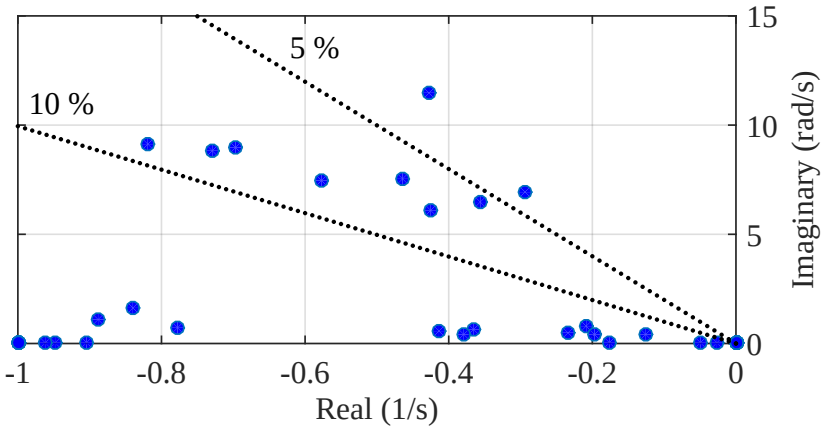

Figure 4.8: System eigenvalues of the IEEE 39-bus test system.

are 9 electromechanical, most of them have damping ratios between 5% and 10% except one local mode of G_1 with frequency 11.5 rad/s and one inter-area mode between G_{10} and (G_2, G_3, G_9) with frequency 6.9 rad/s.

Calculations for the TAS analysis are performed for a 64 ms short-circuit at bus 12—fault clearing time for a two-cycle circuit breaker. Generator buses are chosen as prospective control buses. Machine speeds and angles are monitored and their values right after clearing the short-circuit are used as initial states in the sensitivities calculation. Table 4.3 shows the TAS $\partial S_\infty/\partial\theta_k$ for each bus sorted from the best to the worst bus candidate to damp the oscillation energy. Additionally, the first and second column show the same calculation neglecting the sensitivity coefficient α, i.e, assuming the eigenvector derivatives are zero, which comes from the assumption that the mode shapes are not affected by the control gain θ_k. As the table shows, both the exact and approximated results point out bus 39 as the best choice to control the system oscillations after this disturbance. Besides bus 30, all other buses play a similar role in damping the oscillation energy with relatively small differences. Note that the information provided in Table 4.3 can be also used to choose a set of optimal actuators in a centralized control scheme.

Time domain simulations are performed using the full set of nonlinear differential algebraic equations. A 200 MW BESS is connected at bus 39, 36 and 34 at a time to

Table 4.3: Total action sensitivities for short-circuit at bus 12 in the IEEE 39-bus system.

Bus	$\sum \beta_i \partial\lambda_i/\partial\theta_k$	Bus	$\partial S_\infty/\partial\theta_k$
39	−0.0192	39	−0.0136
30	−0.0141	30	−0.0082
36	−0.0123	32	−0.0067
35	−0.0119	31	−0.0061
34	−0.0116	37	−0.0060
38	−0.0115	36	−0.0057
33	−0.0114	38	−0.0057
37	−0.0112	33	−0.0057
32	−0.0111	35	−0.0056
31	−0.0104	34	−0.0056

compare the results with those obtained by the TAS analysis. A delay block is added to the BESS control loop so it only reacts after the short circuit is cleared, which gives enough time to update the initial state vector in the TAS calculation and to send a signal to the best BESS location in the case of a centralized control scheme. Figure 4.9 shows the system kinetic energy for the case without BESS and with BESS at each of the selected locations. The results show that the BESS at bus 39 is the most effective to quickly damp the oscillation energy, while the BESS at bus 36 and 34 have similar dynamic responses. Although this simulation is performed including the nonlinear equations and using a large droop gain for the BESS, still follows the expected results from the TAS analysis. Therefore, the TAS framework is proven to find the best actuator in the system. Note that, the accuracy of the results depend on the linearity of the eigenvalues and eigenvector trajectories. For nonlinear trajectories—usually for larger droop gains—second order sensitivities or linear piecewise approximation for the total action may be needed.

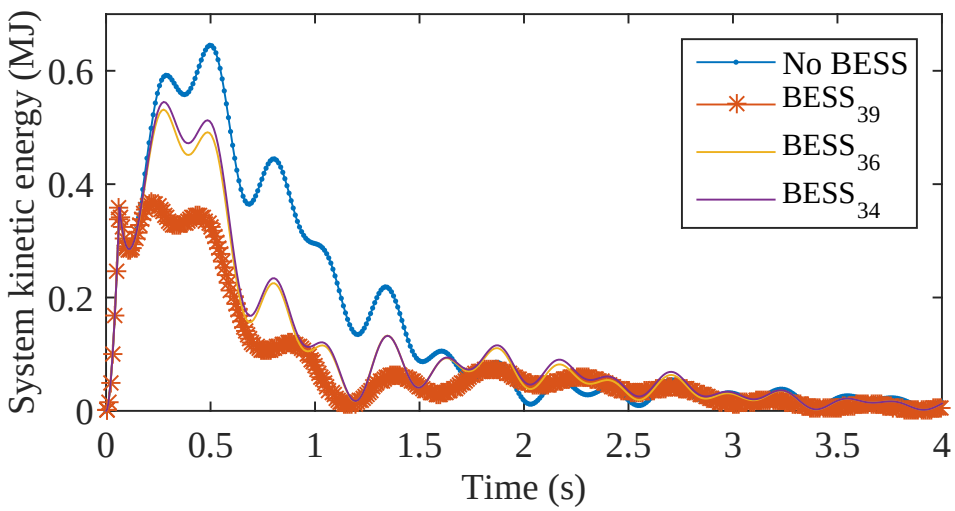

Figure 4.9: System kinetic energy of the IEEE 39-bus system after a 64 ms short-circuit at bus 12.

4.3.3 Final remarks

The proposed TAS analysis described in this chapter successfully identifies the best control actuator/location in order to minimize the system kinetic energy variation over time. This can be used in several application, such as:

- Oscillation damping control allocation: on-line TAS evaluation can determine single or multiple actuators, either conventional or non conventional such as RE resources or energy storage.
- Optimal tunning: phase lead compensator of different actuators can be tuned to optimize a total action-based cost function by changing the direction of eigenvalue trajectories.
- System planning: off-line TAS analysis for common disturbances can lead to criteria for the deployment of regulating devices to dynamically strength the system.

4.4 Summary

This chapter describes an oscillation energy analysis to identify the best actuator/location in systems with multi-mode oscillation problems. By expressing the system kinetic energy in terms of the system eigenvalues and eigenvectors, and by calculating the sensitivity of the total action, an algebraic function of the initial states is obtained. The TAS results are validated in the IEEE 9-bus and IEEE 39-bus systems. Time domain simulations show that the TAS analysis is successful to provide the optimal solution in terms of the most effective actuator/location to quickly damp the oscillation energy, and therefore, damp all electromechanical oscillations. Promising applications of the TAS analysis in control and system planning are discussed.

Chapter 5

Adaptive coordination

This chapter introduces an adaptive coordination of damping controllers. The coordination uses phasor measurement units (PMUs) to adapt to different disturbances by selecting the switching status (on/off) of damping controllers that minimizes an energy-based dynamic performance measure. This dynamic performance measure, referred to as total action (TA), uses a physical interpretation of excited modes rather than fixed targeted modes as in the traditional damping control design. The coordination is formulated as a binary integer programming problem, which is solved by using the total action sensitivity (TAS). The concept of oscillation energy and the implementation of the adaptive coordination scheme is tested in the western North America power system (wNAPS). The results show that the proposed adaptive control scheme can improve oscillation damping for different disturbances even in the presence of large communication delays.

5.1 Switching formulation and total action

Examine the linearized power system equations $\dot{x} = Ax + Bu, \quad x(t_0) = x_0$ where $A \in \mathbb{R}^{n\times n}$ is the system matrix in open loop, $x \in \mathbb{R}^n$ is the vector of state variables, $x_0 \in \mathbb{R}^n$ is the vector of initial conditions, $B \in \mathbb{R}^{n\times m}$ is the input matrix and $u \in \mathbb{R}^m$ is the vector of input signals from different damping controllers. The vector of input signals is obtained by measuring frequency, which can be estimated as a linear combination of the system states such that $u = Q_q \Theta C x$, with $C \in \mathbb{R}^{m\times n}$ being the output matrix, $\Theta = \text{diag}\{\theta_1, ..., \theta_k, ...\theta_m\}$ the matrix

of damping controllers gains, and $Q_q = \text{diag}\{q_1, ...q_k, ...q_m\}$ the switching matrix with q_k the switching signal that activates ($q_k = 1$) or deactivates ($q_k = 0$) the k-th damping controller. The closed loop system matrix becomes $A_q = (A + BQ_q\Theta C)$. Furthermore, for a given switching combination of damping controllers consider the similarity transformation $\Lambda_q = M_r^{-1}A_qM_q = \text{diag}\{\lambda_{qi}\}$, where λ_{qi} is the i-th system eigenvalue and $M_q = \{v_{q1}, v_{qr}, ...v_{qn}\}$ is the matrix of right eigenvectors. As a result, the state space model is transformed to $\dot{z} = \Lambda_q z, \quad z_0 = M_q^{-1}x_0$ and $z = M_q^{-1}x$. Then, the system kinetic energy for the given switching combination is defined as [116]:

$$E_k(t) = \sum_{j=1}^{p} H_j\omega_s\Delta\omega_j^2(t) = x^T H\omega_s x \tag{5.1}$$

$$= \frac{1}{2}z^T G_q z \in \mathbb{R} \tag{5.2}$$

where p is the number of synchronous generators, $\omega_s = 120\pi$ is the synchronous speed in rad/s, $\Delta\omega_j$ is the speed deviation of generator j in pu, H is the inertia matrix in s—with only nonzero elements in the diagonal terms $H_{ii}\ \forall\ i \in \Omega_\omega$ for Ω_ω the set of speed indices of all synchronous generators—and matrix $G_q = M_q^T 2H\omega_s M_q$ is an equivalent transformed inertia matrix. The action for the switching combination is obtained as:

$$S(\tau) = \int_0^\tau E_k(t)dt = \int_0^\tau \frac{1}{2}(z^T G_q z)dt \in \mathbb{R} \tag{5.3}$$

$$S(\tau) = \frac{1}{2}\sum_{j=1}^{n}\sum_{i=1}^{n}\frac{e^{(\lambda_{qi}+\lambda_{qj})t}}{(\lambda_{qi}+\lambda_{qj})}z_{0i}z_{0j}g_{ij}\Big|_0^\tau \tag{5.4}$$

where z_{0i} is the i-th element of z_0 and g_{ij} is the entry in the i-th row and j-th column of G_q. Finally, for an stable system the general expression for the total action becomes:

$$S_\infty = \lim_{\tau\to\infty} S(\tau) = -\frac{1}{2}\sum_{j=1}^{n}\sum_{i=1}^{n}\frac{z_{0i}z_{0j}g_{ij}}{(\lambda_{qi}+\lambda_{qj})} \tag{5.5}$$

To enhance the system dynamic performance, the best combination of $q_k \in [0,1]\forall k \in \mathcal{K} = \{1, ..., m\}$ that minimizes S_∞ for a given disturbance must be found.

5.2 Adaptive switching

5.2.1 Mathematical description

The adaptive coordination problem for an initial disturbance $x(t_0) = x_0$ is formulated as a binary integer programming (IP) problem that finds the optimal switching combination $Q_{q^*} = \text{diag}\{q_k\}, \forall k \in \mathcal{K}$ that minimizes the total action of $\dot{x} = A_q x$. Formally, we have:

$$\min_{q_k \forall k \in \mathcal{K}} S_\infty \tag{5.6}$$

subject to:

$$\dot{x}(t) = A_q x(t), \quad x(t_0) = x_0 \tag{5.7}$$

$$q_k \in \{0, 1\} \forall k \in \mathcal{K} \tag{5.8}$$

As in actual systems, the number of damping controllers is large, this becomes a non-deterministic polynomial time (NP) hard problem. Exhaustive evaluation for all combinations $q_k \in \{0, 1\} \forall k \in \mathcal{K}$ is prohibited and the goal is transformed into obtaining the best solution possible with guarantee of optimality.

5.2.2 Proposed solution

Consider an equivalent problem where the gains $\theta_k, \forall k \in \mathcal{K}$ of the damping controllers are analyzed. These gains can change continuously in $[0, \theta_{nk}]$, where θ_{kn} is the nominal gain. Note that the extreme values of θ_k are equivalent to the effect of $q_k = 0$ and $q_k = 1$ respectively. By using this continuous variable now the problem can be solved by a first order estimation of the Taylor expansion of S_∞—which has shown to be adequate [117]—around an initial switching condition with signals q_{k0} and initial gains θ_{k0}.

$$\begin{aligned} \Delta S_\infty &\approx \underbrace{\Delta S_\infty(\Delta\theta_1)} + \underbrace{\Delta S_\infty(\Delta\theta_2)} + ... + \underbrace{\Delta S_\infty(\Delta\theta_m)} \\ &\approx \quad \frac{\partial S_\infty}{\partial \theta_1}\Delta\theta_1 + \quad \frac{\partial S_\infty}{\partial \theta_2}\Delta\theta_2 + ... + \quad \frac{\partial S_\infty}{\partial \theta_m}\Delta\theta_m \end{aligned} \tag{5.9}$$

Equation (5.9) is used to minimize the total action by looking at the independent effect of each damping gain. The TAS with respect to the gain θ_k is defined as:

$$\frac{\partial S_\infty}{\partial \theta_k} = \alpha_k + \sum_{i=1}^{n} \beta_i \frac{\partial \lambda_{q0i}}{\partial \theta_k} \tag{5.10}$$

with

$$\alpha_k = -\sum_{j=1}^{n}\sum_{i=1}^{n} \frac{z_{0j} g_{ij}}{(\lambda_{q0i} + \lambda_{q0j})} \frac{\partial z_{0i}}{\partial \theta_k} - \sum_{j=1}^{n}\sum_{i=1}^{n} \frac{z_{0i} z_{0j}}{2(\lambda_{q0i} + \lambda_{q0j})} \frac{\partial g_{ij}}{\partial \theta_k} \tag{5.11}$$

$$\beta_i = \sum_{j=1}^{n} \frac{z_{0i} z_{0j} g_{ij}}{(\lambda_{q0i} + \lambda_{q0j})^2} \tag{5.12}$$

The first term α_k in equation (5.10) depends on the eigenvector derivatives, which can be obtained by solving a set of linear equations in terms of the eigenvalues [115]. Although the existence and uniqueness of eigenvector derivatives are not guaranteed for general systems, in power systems they are usually well behaved around a stable operating point. Nevertheless, from simulations is observed that the terms α_k that are associated with eigenvector derivatives are relatively small and can be neglected. The last term in (5.10), which is usually larger than α_k, depends on the eigenvalue derivatives, calculated as ${}^{\partial \lambda_{q0i}}/_{\partial \theta_k} = l_{q0i}^T \frac{\partial A_q}{\partial \theta_k} v_{q0i}$ with l_{q0i}^T the left eigenvector transpose associated with λ_{q0i}. The adaptive coordination scheme proposed in this thesis is sketched in Figure 5.1 and the detailed switching law for each damping controller is presented in the following subsections.

5.2.3 Implementation: Off-line procedure

This stage is model-based and provides the necessary information to calculate the total action sensitivities of all damping controllers for any disturbance. The outcomes of the off-line procedure are the collections $\mathcal{G}_k$, $\forall k \in \mathcal{K}$ that include eigenvalues, eigenvalue sensitivities, eigenvectors, eigenvector sensitivities and the predefined actuator initial switching status q_{k0}. The sensitivities are obtained from the numerical approximation of ${}^{\partial A_q}/_{\partial \theta_k}$ for small gain changes $\Delta\theta_k$ around an initial value θ_{k0}.

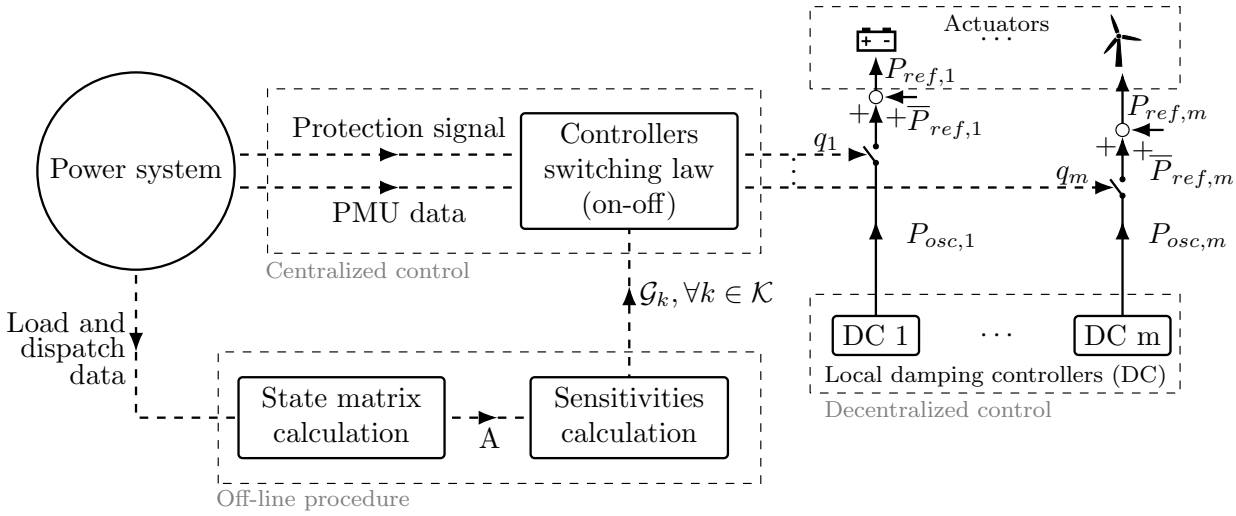

Figure 5.1: Proposed adaptive coordination of damping controllers.

These initial values are zero for actuators that do not participate in the damping control in the base case and equal to the nominal gain θ_{kn} for actuators that participate. Note that the predefined initial switching status of damping controllers and nominal gain are determined from traditional design control. Algorithm 2 shows the procedure to obtain the database of collections.

5.2.4 Implementation: On-line procedure

The proposed adaptive coordination consists of a 2-level hierarchical control: 1st level decentralized control, and 2nd level centralized control.

Decentralized control

This corresponds to the traditional local damping controllers (DC) added to actuators in the system, some of which may be fed by wide-area signals. The control is generally fed by a frequency measurement, and consists of a washout filter, a gain and a phase-lead compensator tuned for one particular mode. The control provides a supplementary reference signal of active power ($P_{osc,k}$) in addition to a main reference signal with slower dynamics

Algorithm 2 Procedure for off-line calculations

Set q_{k0} and θ_{kn} $\forall k \in \mathcal{K} = \{1, ..., m\}$
for each actuator $k \in \mathcal{K} = \{1, ..., m\}$ **do**
    Calculate system equilibrium point for θ_{k0}
    Linearize power system equations
    Obtain system matrix A_0
    Obtain λ_{q0i}, v_{q0i} and l_{q0i}^T $\forall i \in \{1, ..., n\}$
    Set $\Delta\theta_k \approx \gamma\theta_{kn}$ (with $\gamma < 1$, e.g., 10%)
    Calculate system equilibrium point for $\theta_k = \theta_{k0} + \Delta\theta_k$
    Linearize power system equations
    Obtain system Matrix A_1
    Calculate $\frac{\partial A_q}{\partial \theta_k} \approx \frac{A_1 - A_0}{\Delta\theta_k}$
    for each eigenvalue $i \in \{1, ..., n\}$ **do**
        Get $\frac{\partial \lambda_{q0i}}{\partial \theta_k}$, $\frac{\partial v_{q0i}}{\partial \theta_k}$ and $\frac{\partial l_{q0i}^T}{\partial \theta_k}$
    end for
    Save the collection $\mathcal{G}_k$:
    $\{\lambda_{q0i}, v_{q0i}, l_{q0i}^T, q_{k0}, \frac{\partial \lambda_{q0i}}{\partial \theta_k}, \frac{\partial v_{q0i}}{\partial \theta_k}, \frac{\partial l_{q0i}^T}{\partial \theta_k} \forall i \in \{1, ..., n\}\}$
end for

($\overline{P}_{ref,k}$), such as power dispatch or secondary frequency control. Note that reactive power can also be used as a supplementary reference signal [8]. The actuator model (ESSs, WT, etc.) and control parameters are considered in the system model for implementation of Algorithm 2.

Centralized control

This corresponds to one of the main contribution of this thesis. After the system is disturbed and the fault is cleared—a short-circuit for example—a protection signal is sent to the centralized control with time stamp t_0. PMU frequency measurements at the generator buses at t_0 are used to estimate the initial state vector x_0. This vector is estimated by using the frequency changes as machine speed changes. Changes in other state variables are neglected as they have little contribution to the kinetic energy at the beginning of the post-fault system. Given the initial state vector and the collections obtained through Algorithm 1, the TAS in equation (5.10) can be calculated for the estimation of ΔS_∞. Note that this is an algebraic relationship and does not involve computationally expensive calculations, which is why it can be performed on-line. Nevertheless, a sensor delay τ_a is added to model the time lapse from the short-circuit clearance until its detection to obtain $x_0(\tau_a)$. Similarly, a delay τ_b is included to represent the combined effect of three different delays: the latency from transmitting the PMU data to the centralized control, the computation time of ΔS_∞ and the latency from transmitting the new switching signals q_k to each actuator in $\mathcal{K}$. For a given disturbance, the switching signal $q_k \in \{1, 0\}$ is sent by the centralized control to determine whether the actuator participates in the damping control. Note that this affects only the supplementary signal P_{osc} of the local DC.

The following switching law is based on the estimated change in the total action when a damping controller k changes its switching status by choosing the direction in the independent vector space of the damping control gains that minimizes ΔS_∞ in (5.9). For $\Delta\theta_k > 0$ and $\Delta S_\infty(\Delta\theta_k)$ in percentage of the base case S_∞^0 the switching law is:

- Available actuators ($q_{k0} = 0$) change their status to "on" ($q_k = 1$) when $\Delta S_\infty(\Delta\theta_k) < \Delta\check{S}_\infty < 0$.

- Actuators that originally participate in the damping control ($q_{k0} = 1$) change their status to "off" ($q_k = 0$) when $\Delta S_\infty(\Delta\theta_k) > \Delta\hat{S}_\infty > 0$.

where $\Delta\check{S}_\infty$ and $\Delta\hat{S}_\infty$ are thresholds—designed from observation of the system—intended to avoid status switching leading to marginal improvements. After the control is implemented and the system goes back to steady state, all changes in switching status are reset back to q_{k0}.

5.3 Case study

The proposed adaptive coordination scheme is tested in the wNAPS using the 179-bus WECC system with 20% of wind power penetration. Network data, operational data and dynamic parameters of the system are found in [112]. The model successfully captured the typical modes observed in the system, including the four well-known inter-area modes: "NS mode A", "NS mode B", "BC mode" and "Montana mode", among others [118], although with a more critically undamped behavior for the sake of analysis. The 20% of wind penetration is achieved by connecting 11 equivalent DFIG-based wind turbines to the system [8]. Figure 5.2 shows the one-line diagram of the WECC system and the wind turbine sites. Simulations are performed in DIgSILENT PowerFactory. Synchronous generators use a 6th order model with IEEE standard governor model (IEESGO) and different excitation systems. Power system stabilizers are also incorporated in some machines. Loads in the system are modeled as constant power. Wind turbines use the general DFIG template from the software library [110], which includes a detailed mechanical model (pitch control, turbine model, shaft), MPPT and speed control, active, reactive power control together with measurement and protection devices.

5.3.1 Local damping control actuators

Seven equivalent EIRs with capability to participate in damping control through injection of active power in the range of ±200 MW are connected to the WECC system. Note that these equivalent EIRs can represent the aggregated effect of several EIRs in the connection

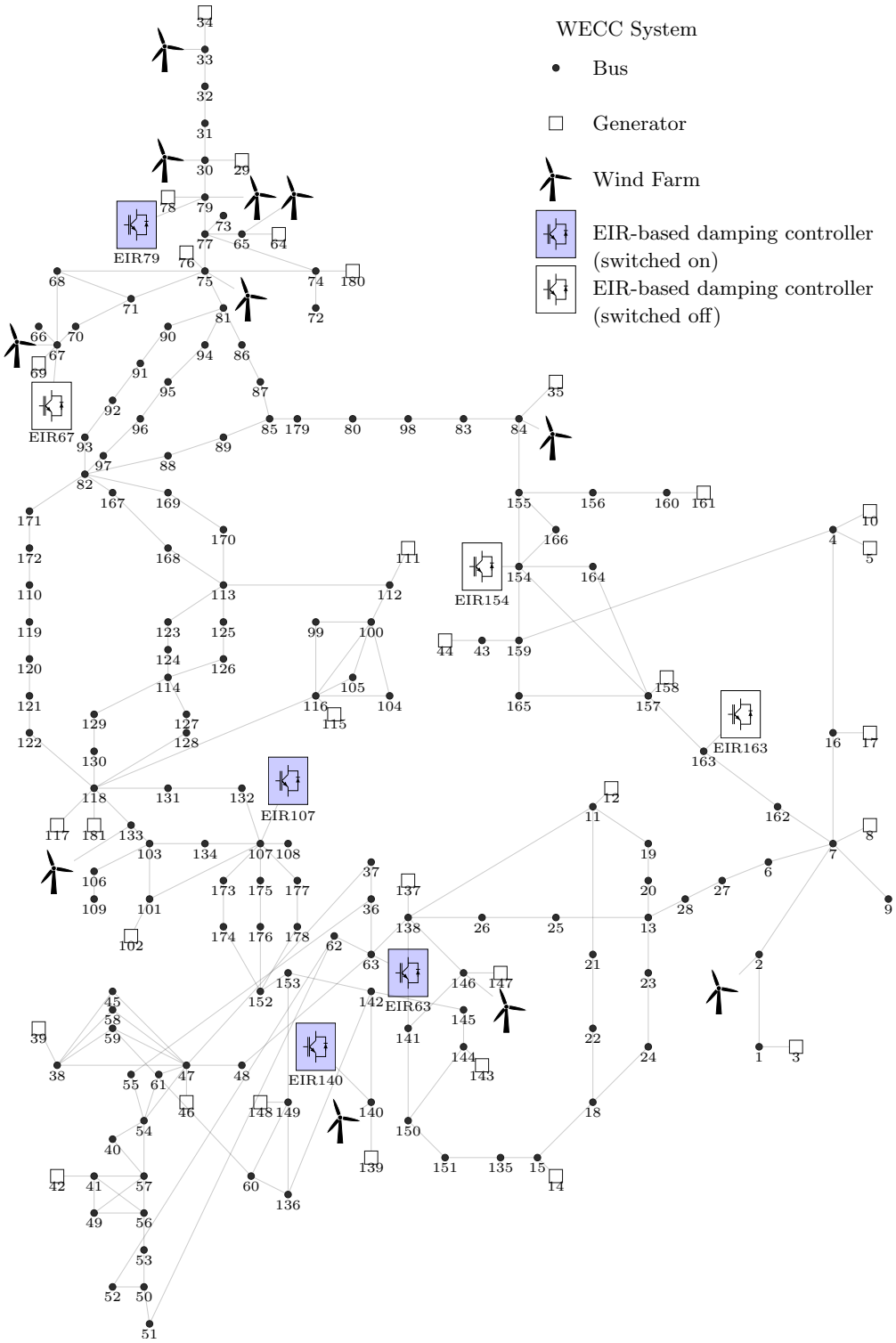

Figure 5.2: WECC system with base case configuration.

point. Figure 5.2 displays the EIRs sites and their base case on/off switching status in the damping control. Available actuators ($q_{k0} = 0$, $k = \{1, 2, 3\}$) are EIR67, EIR154 and EIR163 respectively. The actuators that originally participate in the damping control ($q_{k0} = 1$, $k = \{4, 5, 6, 7\}$) are EIR79, EIR107, EIR63 and EIR140. All damping controllers are tuned to damp local oscillations in the neighboring area, except EIR140 which uses a wide-area measurement of frequency at bus 4 to damp the inter-area mode between East and South. For simplification purposes, each equivalent EIR is modeled as an equivalent battery energy storage which is taken from the DIgSILENT PowerFactory library; the dynamics associated with this model are very fast in comparison to electromechanical dynamics and does not create any exogenous dynamic behavior which may lead to erroneous conclusions. Each EIR is controlled as well to keep a unity power factor. The active power loop is modified as shown in Figure 5.3 with typical parameters, $\overline{P}_{ref} = 0$ and and $\theta_k = \theta_{kn} = 400$, for $k = \{1, ..., 6\}$ and $\theta_7 = \theta_{7n} = 100$.

5.3.2 Preliminary results

After linearization, the WECC system consists of 973 state variables. Figure 5.4 shows the system eigenvalues of the base case. As the system has several critical modes in the range of 2-5% damping ratio (σ), an adequate selection of the limited damping resources becomes very important. Consider two initial disturbance cases for analysis: case (I) disturbing the machine speed of SG69 ($\Delta\omega_{69} = 0.05$) and case (II) disturbing machine speed of SG29 ($\Delta\omega_{29} = 0.05$). Table 5.1 shows the linear estimation of the total action variation $\Delta S_\infty(\Delta\theta_k)$ in percentage of the S^0_∞ for a small gain increment $\Delta\theta_k = 40$ for each damping controller in the system.

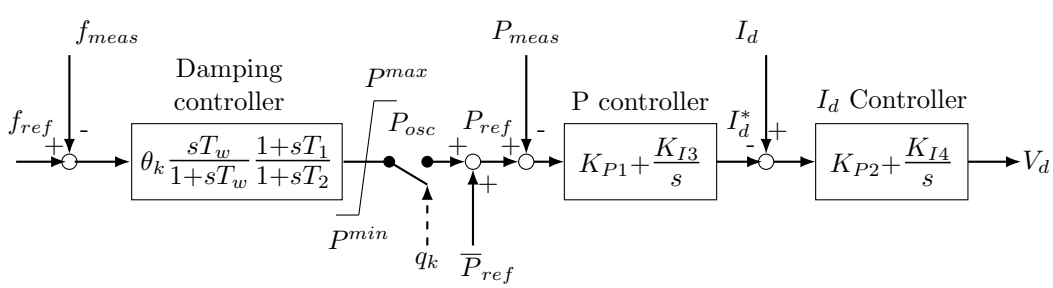

Figure 5.3: Active power loop of k-th EIR.

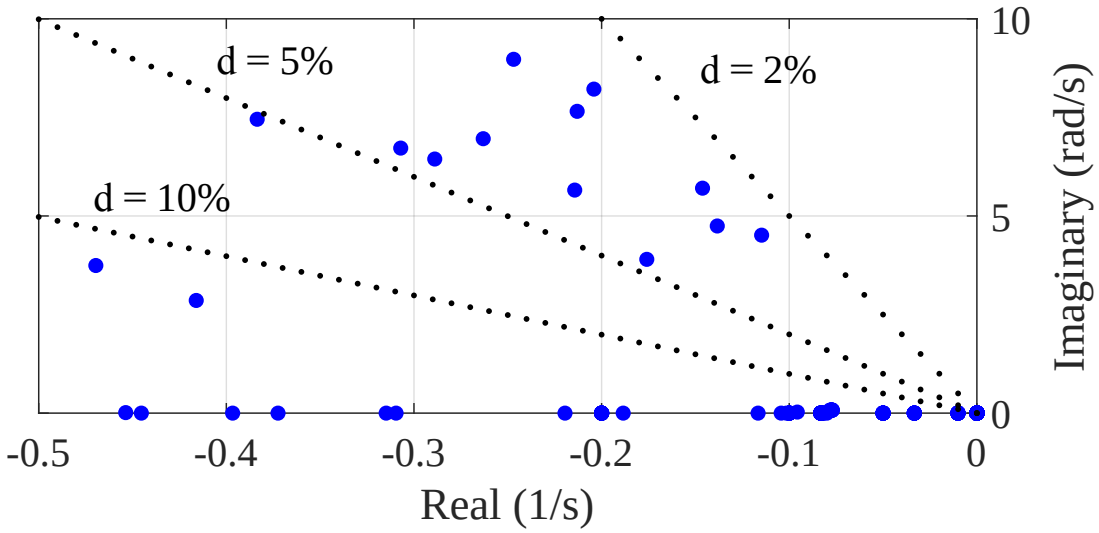

Figure 5.4: WECC system eigenvalues.

Table 5.1: Estimated change of the total action.

EIR off		$\Delta S_\infty(\Delta\theta_k)$ (%)		EIR on		$\Delta S_\infty(\Delta\theta_k)$ (%)	
k	bus	Case I	Case II	k	bus	case I	case 2
1	67	**-14.04**	**-14.36**	4	79	1.27	-3.71
2	154	-2.63	-5.24	5	107	-0.39	-0.64
3	163	-0.08	-1.94	6	63	-3.07	-5.67
-	-	-	-	7	140	5.96	**49.9**

For case (I) the most negative variation from the available set corresponds to EIR67. Figure 5.5 compares the total action of EIR67 and EIR163 with respect to the total action of the base case S^0_∞ when the gain is increased. As expected, EIR163 is less sensitive, while EIR67 can reduce up to 30% the total action. Note that for a gain increment of 10% of the nominal gain, the reduction in the exact total action approximately matches the estimated variation of -14.04 from Table 5.1. Although the total action changes nonlinearly for large gains, its first order sensitivity provides a good approximation to switch the most sensitive damping controllers.

Figure 5.6 shows the oscillation energy and the rotor speed deviation of SG76 for the base case, by switching on EIR67 and EIR163, respectively. The results show that by switching on EIR63 there is an improvement in the oscillation energy. In particular, when a local oscillation involving SG69 is excited, the selection of EIR67 to participate in the control importantly reduces the local oscillation in the north part of the system. This is shown in the damping improvement of $\Delta\omega_{76}$.

For case (II) in Table 5.1, observe that EIR140 produces a large positive variation of the total action. Thus, the disconnection of the damping controller in EIR140 can drastically improve the dynamic performance for the given disturbance. Figure 5.7 compares the parametrization of the total action for two EIRs that originally participate in the damping control.

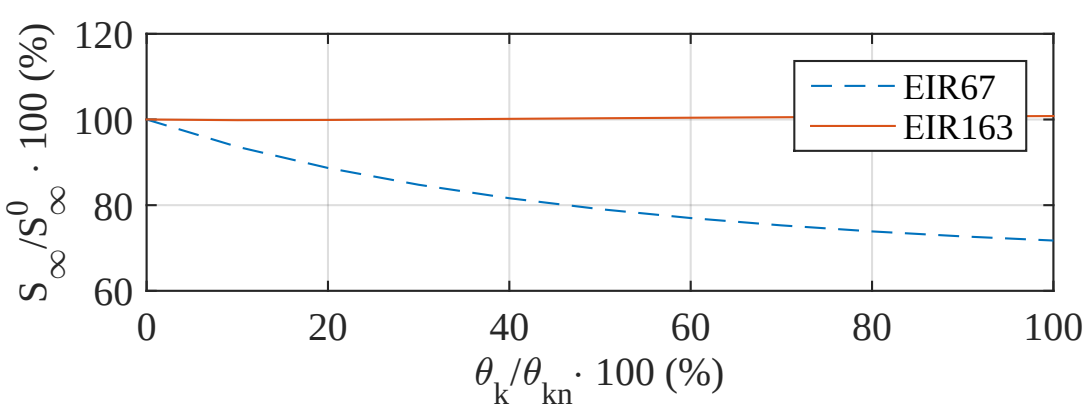

Figure 5.5: Parametrization for disturbance in speed of SG69.

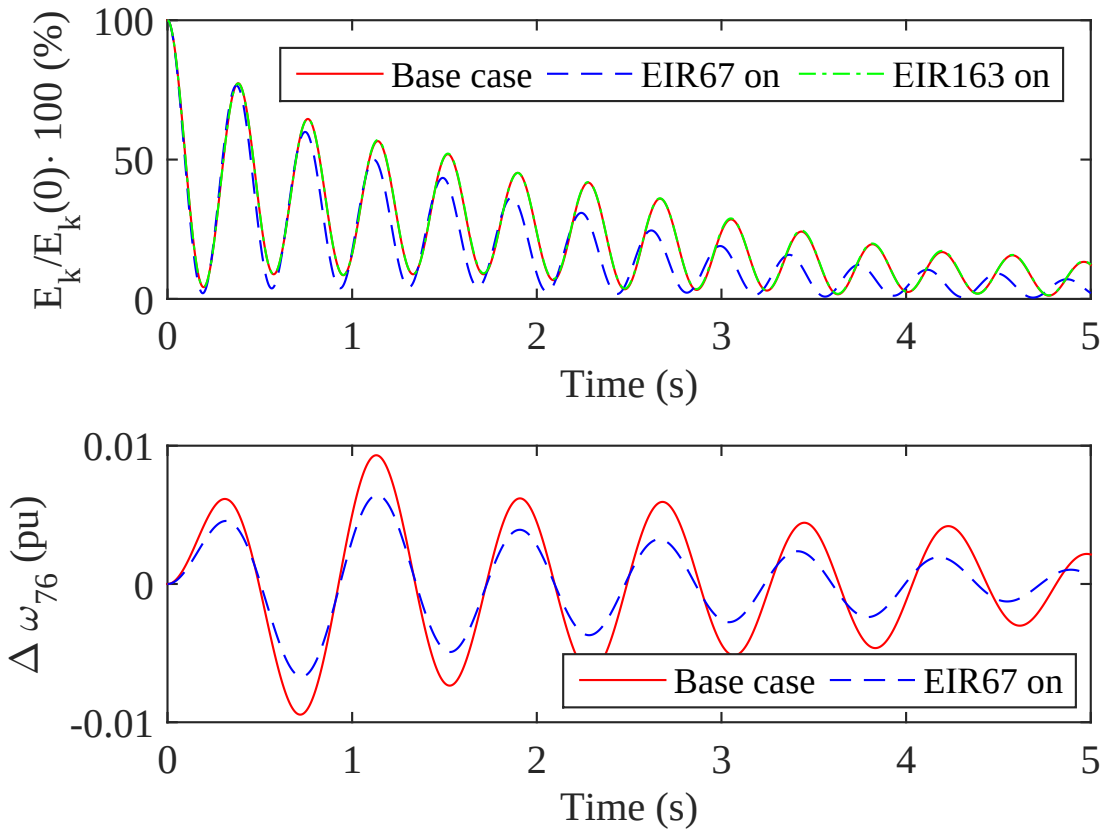

Figure 5.6: Kinetic energy of WECC for disturbance at SG69.

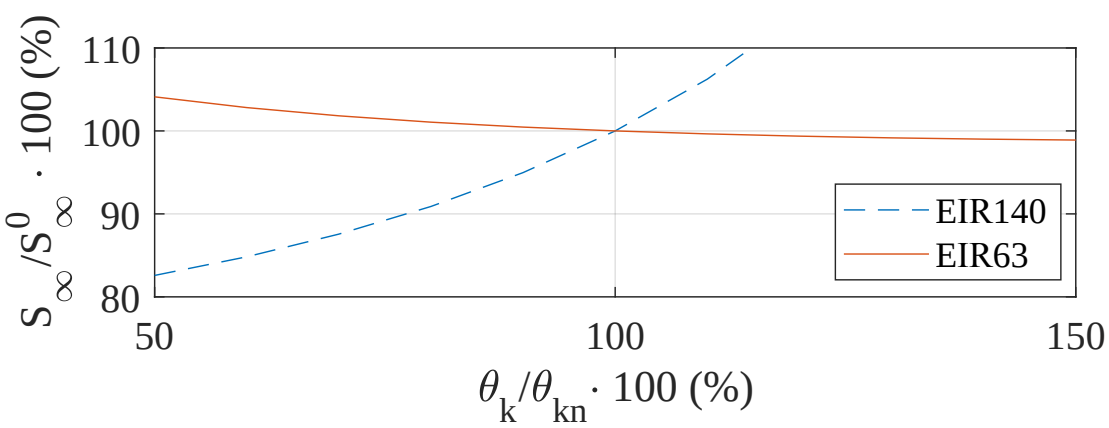

Figure 5.7: Parametrization for disturbance in speed of SG29.

Again, note that the linear estimation successfully describes the situation. Both damping controllers are already connected, thus, the damping controller of EIR140 must be switched off to minimize the total action. Figure 5.8 shows time domain simulations of the oscillation energy and rotor speed deviation of SG139.

The proposed linear estimation of the total action by means of its first order sensitivity is proven to identify the detrimental effect of the damping controller in EIR140 when the disturbance is located in SG29. By disconnecting the damping controller in EIR140 the oscillation energy is reduced. This occurs because the damping controller in EIR140 was tuned to damp an inter-area mode of around 0.6 Hz in the southern half of the system; however, this deteriorates the damping ratio of another inter-area mode of around 0.7 Hz that exhibits a high participation factor of the machine speed of SG29 and SG139—excited by this disturbance. The improvement achieved by disconnecting the damping controller in EIR140 can be seen in the damping enhancement of $\Delta\omega_{139}$ in Figure 5.8.

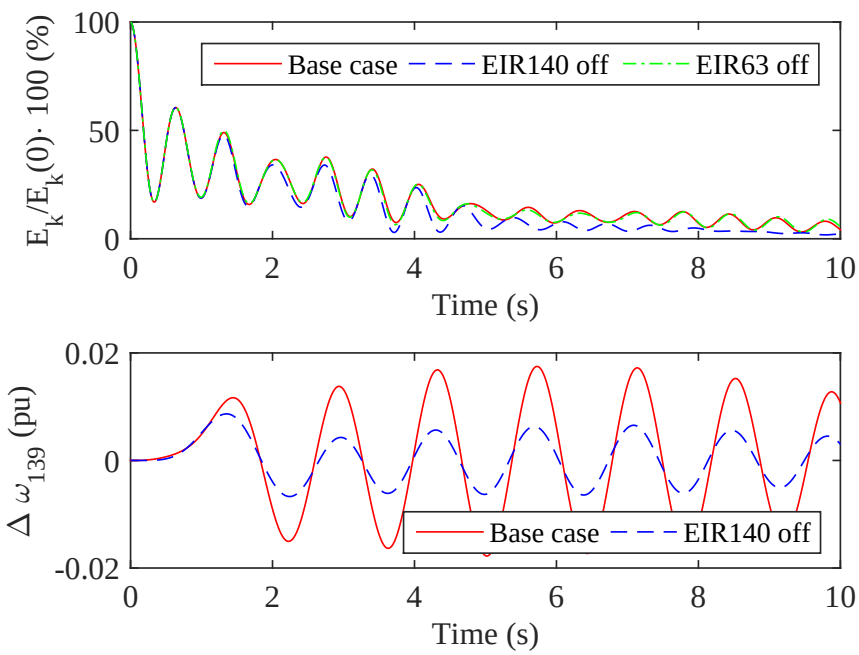

Figure 5.8: Kinetic energy of WECC for disturbance at SG29.

5.3.3 On-line implementation

The adaptive coordination of damping controllers is implemented in non-linear simulations. PMU data is typically transmitted at 48 frames per second ($\approx$ 20 ms), which can be assumed as the sensor delay in case the fault clearance is not detected in the first but in the next time stamp. Hence, the sensor delay is set to $\tau_a = 20$ ms.

Effective delay in recent real implementation of damping control using the Pacific DC Intertie and wide-area measurements in the WECC system—considering measurement, communication, control and command delay— have been reported to range between 69 and 113 ms [119, 120, 121]; this is well within tolerances for oscillation in the 0.1 to 1 Hz range, with an acceptable delay of up to 200 ms. The computation time of the proposed controller selector scheme varies depending on the computer used for the centralized control. Thus, the computation and communication delay τ_b is studied for an optimistic case with $\tau_{b1} = 0.4$ s and a pessimistic case with $\tau_{b2} = 2$ s. The negative and positive thresholds for the estimated total action variation are designed from the observation of the total action, and are set to $\Delta\check{S}_\infty = -10\%$ and $\Delta\hat{S}_\infty = 10\%$ respectively. Figure 5.9 shows the kinetic energy oscillation after a 64 ms short-circuit at bus 30.

The proposed adaptive coordination strategy improves the oscillation energy by changing the switching status of EIR67 from off to on, and changing the switching status of EIR140 and EIR107 from on to off. Note that while the optimistic delay is the best at damping the oscillation energy, the pessimistic delay still provides a significantly improved response in comparison to the the base case (without adaptive coordination). Figure 5.10 exhibits the rotor speed deviations of all the generators for (a) the base case, (b) optimistic τ_{b1} case and (c) pessimistic τ_{b1} case. The speeds in Figure 5.10 (c) are damped before 10 s, despite acting 2 s later than the base case in Figure 5.10 (a). In the worse delay case (communication loss) the proposed adaptive coordination is robust in the sense that does not worsen the dynamic performance of the base case. Consider now the control actions for different PMU reporting rates [122], which results in different sensor delays τ_a. Although the initial state vector $\Delta x_0(\tau_a)$ changes for different sensor delays, the control actions—based on the switching signals sent to the actuators—do not change within this time frame. Therefore, the proposed

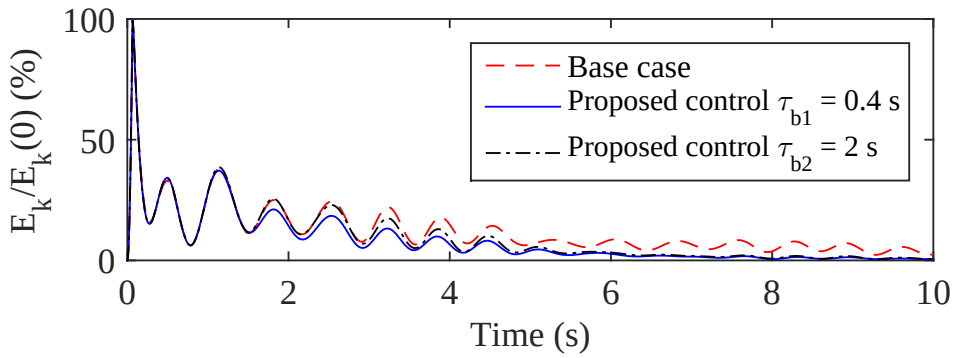

Figure 5.9: Kinetic energy of WECC for short-circuit at bus 30.

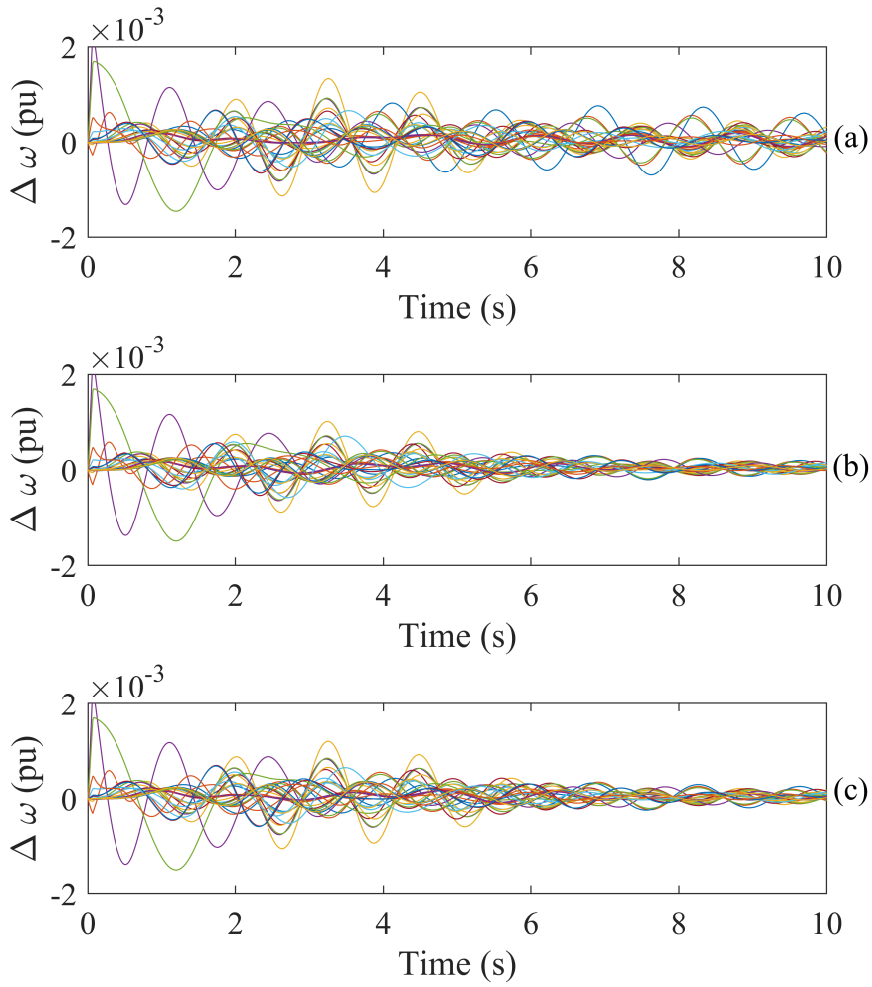

Figure 5.10: Rotor speed deviations of the WECC for short-circuit at bus 30 for: (a) base case, (b) proposed control with delay τ_{b1} and (c) proposed control with delay τ_{b2}.

adaptive coordination scheme is robust against both delays providing satisfactory dynamic performance improvement.

5.4 Final remarks

Before final implementation in a real system, the following considerations need to be addressed for the particular system of interest:

1) Linearity assumption and eigenvector derivatives: The determination of controller switching status (on-off) depends on the estimation of the changes in the total action, which is calculated assuming linear eigenvalue trajectories. This linear estimation is accurate for small actuators, however, as the actuator size gets bigger and the eigenvalue displacement is more relevant; second order sensitivities might be needed. Moreover, the effect of eigenvector derivatives α_k in equation (5.11) can be neglected if the mode shapes do not considerable change, speeding up the computation time.

2) Operation and topology changes: These changes can affect the accuracy of the sensitivities, and therefore, the estimation of the total action. A simple way to address this problem is to store a larger collection of data $\mathcal{G}_k$ by repeating Algorithm 2 for the selected operation—e.g., high, medium and low demand—and contingency scenarios. Reduced order models, system matrix sensitivities to these changes or adaptive control can also be implemented to improve the current adaptive coordination.

3) Large-scale system application: For larger systems, with several thousand of buses and state variables, a different approach can be applied for the off-line calculation of eigenvalues such as Prony method or eigenvalue realization algorithm (ERA). Similarly, a modified total action can be defined to represent the effect of eigenvectors and eigenvector derivatives. Future research will address this issue.

5.5 Summary

This chapter proposes a novel disturbance-adaptive coordination of damping controllers to improve system dynamic performance. The proposed framework uses the switching (on-off) of different damping controllers to minimize oscillation energy and total action in the system following a disturbance. The disturbance adaptation provides a new way to improve performance because it uses the information of the excited modes and their respective energy effect in the grid rather than arbitrarily targeted modes. Moreover, the adaptive coordination scheme works on top of the traditional damping control, avoiding complex system design and tuning. The basic concepts of the oscillation energy and total action are introduced for general systems and used to define a binary integer programming problem for the damping controllers coordination. The adaptive coordination problem is solved by looking at the total action sensitivity to determine the direction of the variables in the independent vector space of the damping gains, reducing the dimensionality complexity. The scheme is tested in the WECC system with 20% of wind penetration and EIR-based damping controllers. The proposed control is proven to successfully select changes in the switching status of damping controllers that quickly damp the oscillation energy and minimize the total action depending on what modes are excited. Moreover, the proposed control is robust against communication and sensor delays; the base case dynamic performance is improved even when the control actions are delayed 2 seconds.

Part III

Dynamic Reinforcement Planning

Chapter 6

Optimal location of EIRs

This chapter proposes a new probabilistic energy-based method to determine the optimal installation location of electronically-interfaced resources (EIRs) considering dynamic reinforcement under wind variability in systems with high penetration of wind power. The oscillation energy and total action are used to compare the dynamic performance for different EIR locations. A linear estimation of the total action allows to critically reduce the computational time from hours to minutes. A chance-constrained optimization is carried out in the IEEE-39 bus system with 30% of wind penetration to decide the location of an energy storage system (ESS) adding damping to the system oscillations. The results show that the proposed method is superior over traditional dominant mode analysis and arbitrary benchmark for damping ratios, selecting the bus location that guarantees the best dynamic performance with highest probability.

6.1 Linear estimation of the total action

Consider eigenvalue displacements caused by changes in an operational parameter such as the injected wind power $\Delta P_w = P_w - P_{w0}$, a random variable. As the total action must be calculated under the new operating conditions after the changes, to reduce computational burden, an approximation of the total action as a function of the random variable is of interest. By linearizing Equation (4.19) around initial eigenvalues λ_i^0, the following expression

is obtained:

$$\Delta S_\infty \approx \sum_{i=1}^{n} \frac{\partial S_\infty}{\partial \lambda_i} \frac{\partial \lambda_i}{\partial P_w} \Delta P_w = \underbrace{\left(\sum_{i=1}^{n} \beta_i \frac{\partial \lambda_i}{\partial P_w} \right)}_{\gamma} \Delta P_w \tag{6.1}$$

$$\text{where,} \quad \beta_i = \frac{\partial S_\infty}{\partial \lambda_i} = \sum_{j=1}^{n} \frac{z_{0i} z_{0j} g_{ij}}{(\lambda_i^0 + \lambda_j^0)^2} \tag{6.2}$$

$$\frac{\partial \lambda_i}{\partial P_w} = l_i^T \frac{\partial A}{\partial P_w} v_i \tag{6.3}$$

Here l_i and v_i are the left and right column-eigenvectors associated with λ_i, respectively. Note that ΔS_∞ is a real number, although β_i and $\partial \lambda_i / \partial P_w$ are all complex quantities. Based on preliminary evaluations, for an important range of operating conditions, the terms $\partial \lambda_i / \partial P_w$ can be assumed constant and equal to those calculated at the initial condition.

Assume now that we are interested in comparing the total action when different EIR locations are chosen to improve the system oscillations under wind power variability. If k is the bus where the EIR is placed, the total action becomes:

$$S_\infty^k \approx S_\infty^{0k} + \gamma_k \Delta P_w \tag{6.4}$$

where S_∞^k is the total action estimated for EIR at bus k, S_∞^{0k} is the initial total action for bus k at the initial wind power P_{w0} and γ_k is the linear coefficient of equation (6.1) when EIR is connected at bus k.

6.2 Chance-constrained optimization

6.2.1 Formulation

Because the wind power injection ΔP_w is a random variable, the system matrix A, $\Delta \lambda_i \; \forall \, i$ and the total action in equation (4.19) become random variables as well. Conditional probabilities associated with the total action can be computed for a given disturbance. By modeling $x_0 = \Delta x_0$ as a random variable, and obtaining some probability density function of common disturbances based on system data, the total probability of the total action can be calculated

using Bayes' rule. Using this information and recalling that the total action works as a system dynamic performance measure regarding oscillations, what is the system location where an EIR based damping control should be installed? This DPRP problem is stated as:

$$k^* = \arg\max_{k \in \mathcal{K}} \ \Phi_k \tag{6.5}$$

where,

$$\Phi_k = \sum_{x_0 \in X_0} \mathsf{P}(S_\infty^k = \min_{i \in \mathcal{K}} S_\infty^i | x_0) \times \mathsf{P}(x_0) \tag{6.6}$$

$$= \sum_{x_0 \in X_0} \mathsf{P}(S_\infty^k \leq S_\infty^1 ... \cap S_\infty^k \leq S_\infty^m | x_0) \times \mathsf{P}(x_0) \tag{6.7}$$

Here X_0 is the set of initial disturbances and $\mathcal{K}$, with $|\mathcal{K}| = m$, is the set of bus candidates to connect the EIR. Algorithm 3 shows the procedure to solve this chance-constrained optimization using the linear estimation of the total action.

6.3 Case study

The IEEE 39-bus system is employed for simulations. Each synchronous generator is represented by a 6th order model with an IEEE type-1 exciter and an IEEEG1 governor. The

Algorithm 3 Chance constrained optimization

```
Get random vector with N number of samples P_w
for each disturbance x_0 ∈ X_0 do
    for each actuator k ∈ K do
        Calculate γ_k and S_∞^{0k}
        Compute S_∞^k according to (6.4)
    end for
    for each actuator k ∈ K do
        Determine P_k = P(S_∞^k = min_{i∈K} S_∞^i | x_0)
        Update Φ_k^new = Φ_k^old + P_k × P(x_0)
    end for
end for
Obtain k* according to (6.5)
```

wind power variability is studied by adding an equivalent 1,000 MW wind turbine connected at bus 16 in Figure 6.1 ($\approx 30\%$ of the system load). The equivalent wind turbine is modeled as a static generator with fixed dispatched power, i.e., no additional dynamics of the wind turbine are included. The set of generator buses $\mathcal{K} = \{39,\ 31,\ 32, ...,\ 30\}$ corresponds to the set of bus candidates to connect the EIR. For simulation the EIR used in this chapter corresponds to a 200 MW ESS (battery). The damping control consists of a proportional gain between the frequency changes at the connection bus and the reference active power. Data for controllers, system parameters and the full battery model are obtained from the simulation library in DIgSILENT PowerFactory.

6.3.1 Preliminary deterministic analysis

To first get insights of the chance-constrained optimization stated in section 6.2, a parameterized analysis is performed to calculate the exact total action for a disturbance in machine speed ω_1—a short circuit at bus 39. The injected power of the wind turbine is used as a parameter, which is varied from 0 to 1,000 MW. For each prospective ESS location, the parameterized analysis is performed. At each value of wind power generation, the power system equations are linearized, eigenvalues and right/left eigenvector of the system matrix A calculated, and the total action defined in equation (4.19) determined. Figure 6.2 shows the total action as a function of the wind power for each ESS_k connected at bus k.

The results show that for $P_w = 0$ the best bus to place an ESS-based damping control corresponds to bus 36—bus of generator 7. This means that when the ESS is connected to bus 36 the total action is minimized, providing the optimal dynamic performance for system oscillations. However, as the wind power increases, the solution changes and bus 35 becomes the best location—bus of generator 6. Therefore, the optimal location for installing the ESS depends on the wind power, which is a random variable. For this particular disturbance, $\mathsf{P}(P_w < 125\ MW)$ gives the probability that the optimal solution is given by connecting the ESS at bus 36. Similarly, different disturbances can provide different solutions. This shows that the chance-constrained optimization in (6.5) is needed to solve the DRP problem. Figure 6.2 is obtained using the exact calculation of the total action for the ESS connected at each bus at a time. This calculation requires significant computational resources, and

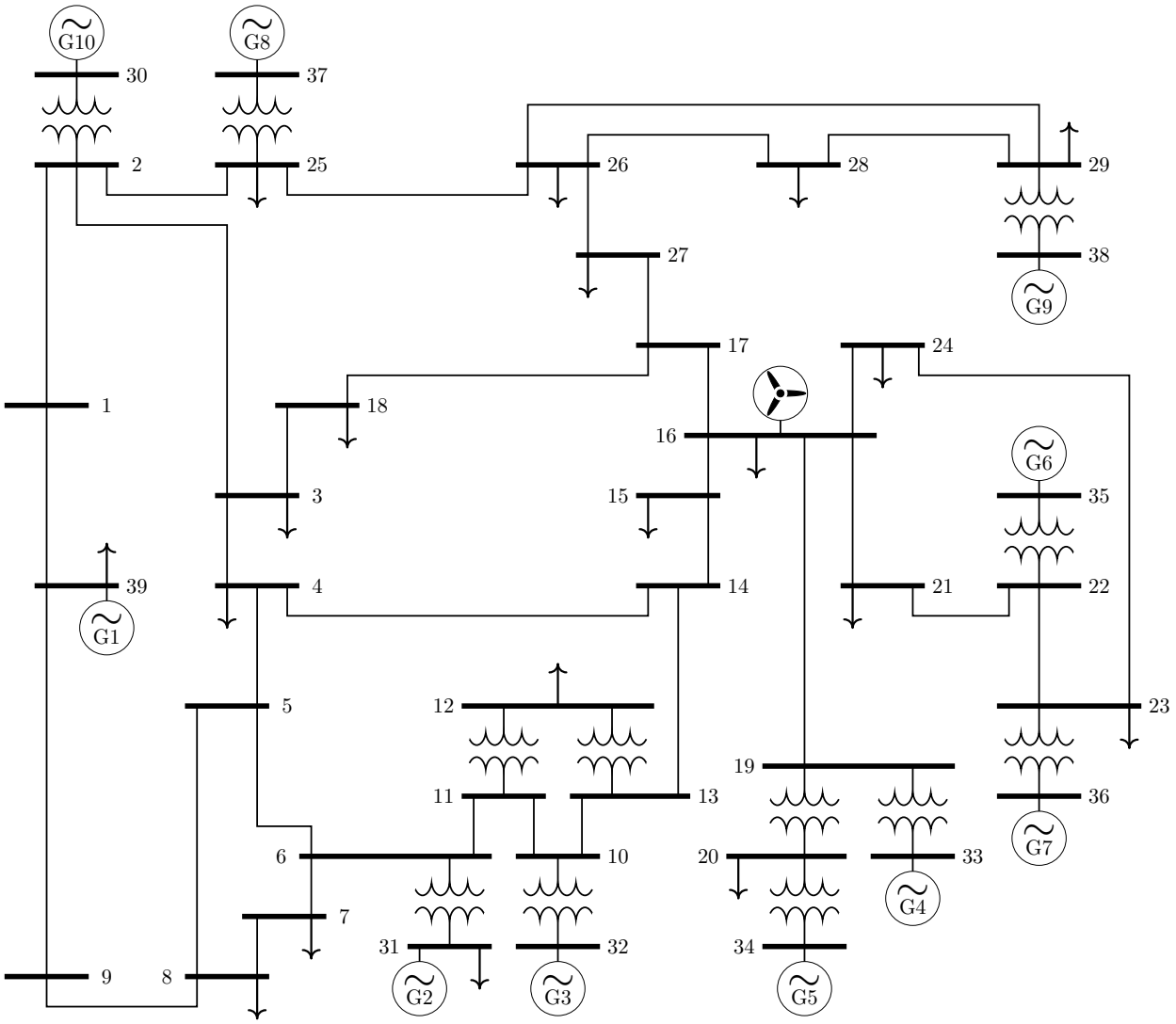

Figure 6.1: IEEE 39-bus test system

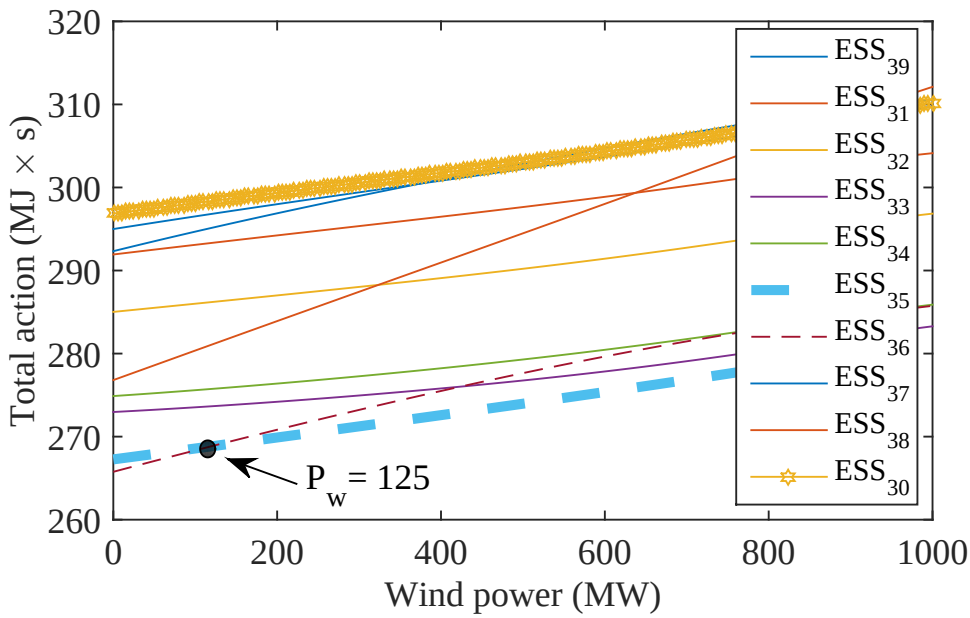

Figure 6.2: Parameterized total action for different ESS location.

therefore, it is impractical in real systems. Consider instead the linear approximation in Equation (6.4). Note that this estimate assumes eigenvalue trajectories to be linear with respect to changes in the wind power. Figure 6.3 verifies this assumption, which, due to space limitations, focuses only the base case without ESS. The arrows in Figure 6.3 represent the direction of eigenvalue trajectories for the electromechanical modes when the parameter P_w is increased.

6.3.2 Stochastic analysis

The chance-constrained DPRP problem is solved through Monte Carlo simulations using the linear approximation of the total action for an initial operation at $P_{w0} = 0$. The sample points P_w are obtained from the pdf of the wind power generated by a Weibull distribution of wind speed. Figure 6.4 shows (a) the deterministic relationship between wind speed and power, (b) the probability density function of the wind speed, and (c) the probability density function of the wind power. The latter is obtained by random variable transformation; parameters can be found in [123].

Before applying Algorithm 3, a total of $1,000$ sample points were employed to compare the results from the exact and estimated calculation of the total action. Figure 6.5 shows

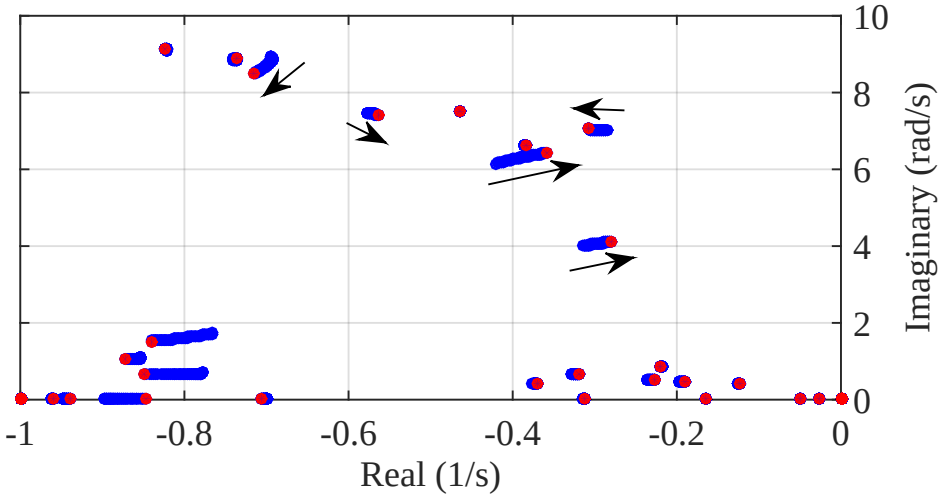

Figure 6.3: Eigenvalue trajectories for the parameterized case without ESS.

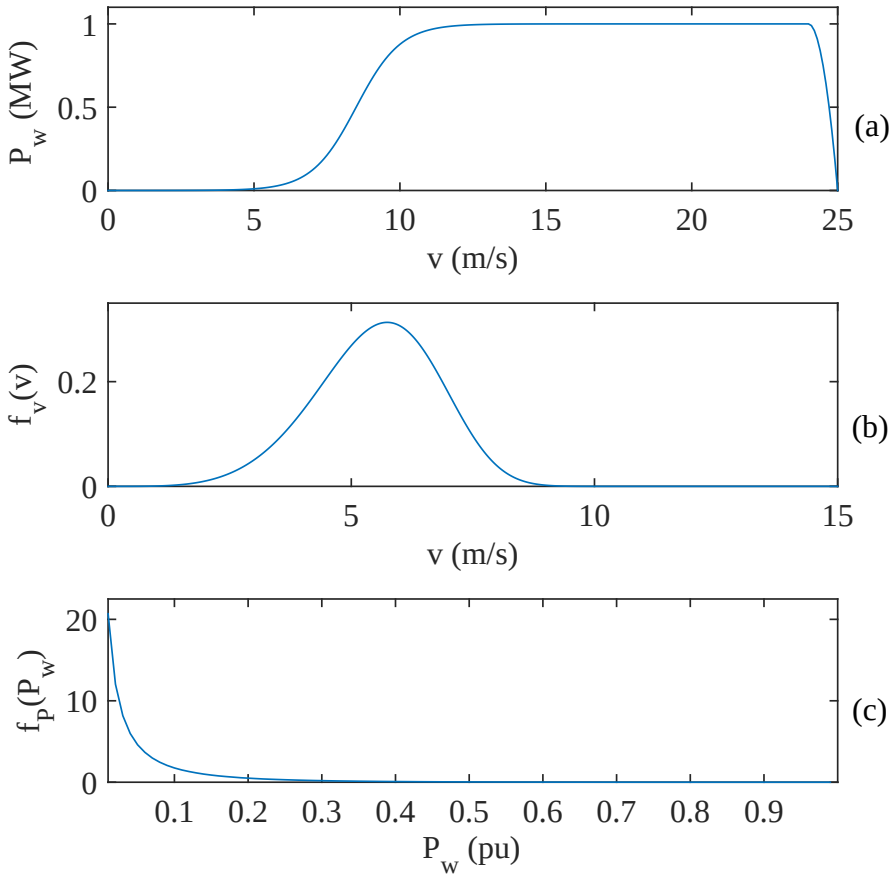

Figure 6.4: (a) Wind speed-power characteristic, (b) Weibull distribution of the wind speed, (c) pdf of the wind power.

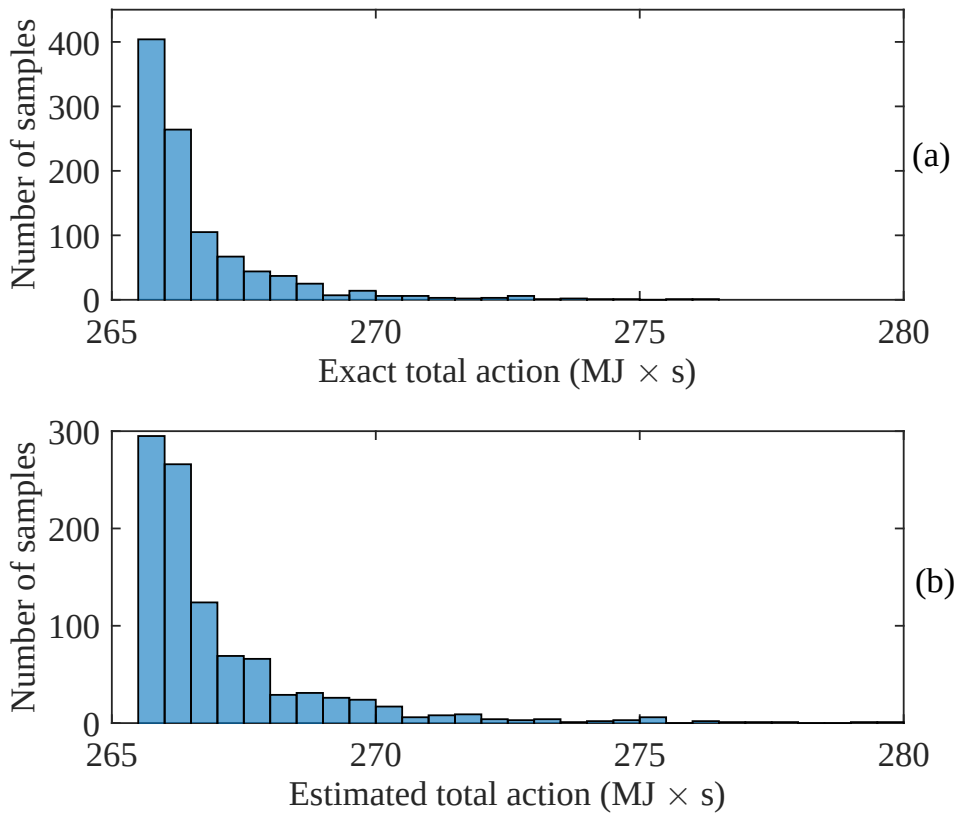

Figure 6.5: Histograms of total action when the ESS is connected at bus 36: (a) exact total action, (b) estimated total action.

the histograms of the total action when the ESS is connected at bus 36 for a disturbance in the speed of generator 1. This preliminary result shows agreement between the distributions of the exact and approximate total action. The big advantage of the approximation is the reduction in computational time, which is about 2 minutes for all the bus cansidates—including the calculation of γ_k—while the exact calculation computing eigenvalues is around 4 hours using an Intel®Core^{TM}i7-4790 CPU @3.6 GHz processor. Consider now $N = 10^6$ sample points of P_ω to solve the chance-constrained problem using the linear estimation, and the set of equally likely disturbances $X_0 = \{x_0^1,\ x_0^2, ...,\ x_0^7\}$, where $\Delta\omega_i = 0.01$ for each disturbance case. Table 6.1 shows the disturbances and the probabilities P_k, which corresponds to the probability of the ESS at bus k providing the minimum total action among all candidates buses over all wind power scenarios.

Table 6.1: Disturbances and probabilities of optimal location for each disturbance

	$\Delta\omega_i$	$\mathsf{P}(S_\infty^k = \min S_\infty^i)$
x_0^1	$\Delta\omega_1$	$\mathsf{P}_{35} = 0.1$, $\mathsf{P}_{36} = 0.9$
x_0^2	$\Delta\omega_1, \Delta\omega_8, \Delta\omega_{10}$	$\mathsf{P}_{35} = 0.07$, $\mathsf{P}_{36} = 0.93$
x_0^3	$\Delta\omega_1, \Delta\omega_2, \Delta\omega_3, \Delta\omega_4, \Delta\omega_5$	$\mathsf{P}_{32} = 0.05$, $\mathsf{P}_{36} = 0.95$
x_0^4	$\Delta\omega_8, \Delta\omega_9, \Delta\omega_{10}$	$\mathsf{P}_{38} = 0.01$, $\mathsf{P}_{30} = 0.99$
x_0^5	$\Delta\omega_1, \Delta\omega_2, \Delta\omega_3, \Delta\omega_8, \Delta\omega_{10}$	$\mathsf{P}_{35} = 0.05$, $\mathsf{P}_{36} = 0.95$
x_0^6	$\Delta\omega_2, \Delta\omega_3$	$\mathsf{P}_{32} = 1$
x_0^7	$\Delta\omega_9$	$\mathsf{P}_{38} = 1$

Using the results given in Table 6.1, the objective function Φ_k in (6.5) can be computed. Table 6.2 shows the results. Note that the chance-constrained optimization determines that bus 36, terminal bus of generator 7, provides the optimal solution for the DRP problem. Thus, connecting an ESS at bus 36 enhances the system dynamics with the highest probability ($\Phi_{36} = 0.53$). In order to show the superiority of the approach proposed in this thesis, different comparison with traditional stochastic analysis are performed. Table 6.3 summarizes the results of the best ESS location obtained by: (a) maximizing the probability of having the dominant mode with a damping ratio above the benchmark, (b) maximizing the probability of having all damping ratios above the benchmark and (c) maximizing the probability of total action being the minimum among all bus candidates. The original system without ESS and with $P_w = 0$ has critical damping ratios between 4 and 8%, therefore, the benchmark is chosen to be 5%. The results in Table 6.3 show that the traditional methods based on arbitrary benchmarks lead to an inefficient solution ($\Phi_{30} < \Phi_{36}$). In this case, the dominant mode corresponds to a local oscillation related to generator 10 connected at bus 30. An ESS connected at bus 30 will improve the local oscillation, however, the reduction in the energy of this oscillation does not improve overall system dynamics much and the probability of exciting this oscillation is small, which creates idle resources regarding the damping capacity of the ESS. The improvement of such local oscillation can be solved locally and does not require a system planning stage. Summarizing, solutions based on arbitrary displacement of eigenvalues may be operationally sufficient, but they are not optimal. On

Table 6.2: Results of the probability that each bus provides the best dynamic reinforcement.

Φ_{39}	Φ_{31}	Φ_{32}	Φ_{33}	Φ_{34}
0	0	0.15	0	0
Φ_{35}	Φ_{36}	Φ_{37}	Φ_{38}	Φ_{30}
0.03	0.53	0	0.14	0.14

Table 6.3: Methods comparison

Optimization method	Optimal solution
(a) Benchmark for dominant mode	$k = 30$
(b) Benchmark for all modes	$k = 30$
(c) Total action and disturbance based	$k = 36$

the other hand, the total action and disturbance based chance-constrained optimization guarantees the best dynamic behavior.

6.4 Summary

This chapter describes a novel approach to guarantee the optimal EIR installation location considering dynamic reinforcement under wind power variability. The proposed chance-constrained optimization uses an energy-based index—total action—to measure system dynamic performance by combining all system eigenvalues rather than the study of a dominant mode or an arbitrary operational benchmark for damping ratios. Additionally, this method benefits from the treatment of disturbance probabilities. Simulations are implemented in the IEEE-39 bus system with 30% of wind penetration, and the location of an ESS is analyzed with a linear estimation of the total action. Results show the the linear estimation drastically reduces the computation time from 4 hours to 2 minutes. Moreover, the comparison of the results with traditional approaches demonstrates its superiority by choosing a location that maximizes the probability of having the best performance, while the solutions obtained by other methods lead to inefficient installations.

Chapter 7

Effect of Wind Farm Spatial Correlation on Oscillation Damping in the WECC System

This chapter studies the effect of spatial correlation between wind speed of geographically closed wind farms on the damping of electromechanical oscillations in the Western Electricity Coordinating Council (WECC) system. Three correlation cases are analyzed based on the measured wind speed in the west coast. The damping of electromechanical oscillations is evaluated by studying all system modes expressed in the oscillation energy and total action. Mote Carlo simulations are performed to obtain different probability density functions (pdfs) of the total action for different correlations and dependence structures. The simulations show that, when wind farm correlation are disregarded, the probabilities for a critical dynamic performance are overestimated, which may lead to misguided planning and operation.

7.1 Wind farm model

7.1.1 Dynamic model

The variable-speed DFIG-based wind turbine is considered for analysis. Consider the i-th wind farm modeled as an aggregated equivalent WT, where the grid side converter

is controlled to keep constant voltage in the dc-link and unity power factor. The rotor side converter is controlled to keep terminal voltage and extract maximum power from the available wind speed (v_i) [124]. Figure 7.1 shows the reactive power control loop with terminal voltage control and the active power loop with optimal tracking acting on the rotor voltage in d-q reference frame.

7.1.2 Stochastic model

The wind speed v_i in Figure 7.1 corresponds to a random variable. Note that the wind speed v_j at a neighboring wind farm can be correlated with v_i depending on the distance between the wind farms and the topographical conditions. Thus, the wind farm injected power and system operation is affected by this correlation. The main contribution of this work is to analyze the effect of this spatial correlation between wind speed of nearby wind farms on the damping of electromechanical oscillations. The global system performance used in this paper consists of a function of all system eigenvalues, obtained by looking at the oscillation energy and total action, providing a physical interpretation of the oscillation problem [116].

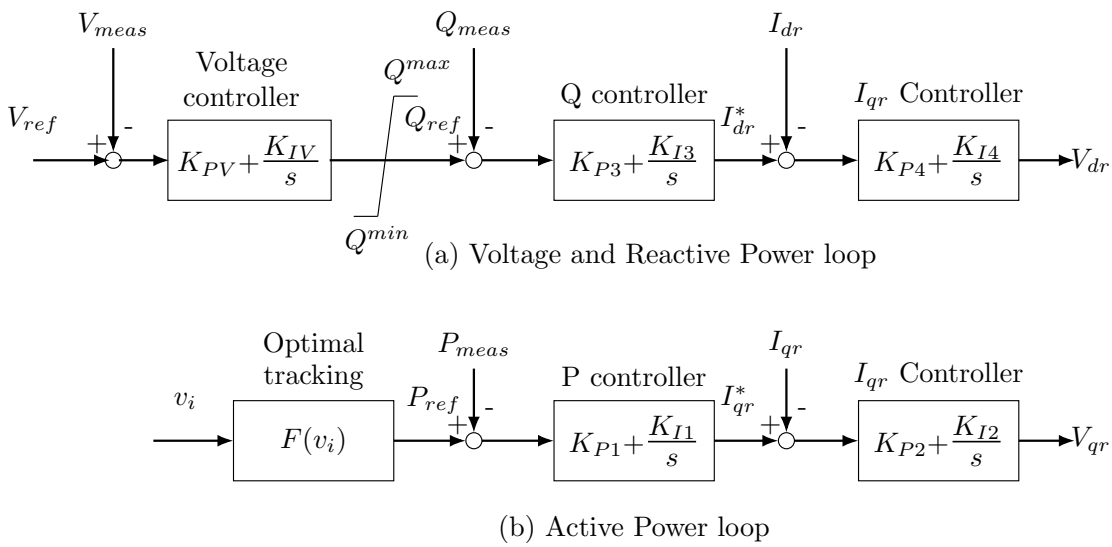

Figure 7.1: DFIG active and reactive power loops.

Sample generation

The sample generation of multivariate correlated random variables becomes challenging as it can be difficult to generate random variables with dependence in distributions different than standard multivariate distribution; which can model only limited types of dependence. Thus, an alternative to represent the joint cdf $F(v_1, ..., v_n) = \mathsf{P}(V_1 \leq v_1 \& ... \& V_n \leq v_n)$ of several random variables $V_1, ..., V_n$, is by using copula theory. Sklar's theorem states that by using a copula with a defined dependence structure between variables, and by specifying marginal univariate distributions $F_1(v_1), ...F_n(v_n)$ it is possible to reconstruct any multivariate joint distribution. Suppose the marginals $F_i(v_i), \forall i \in \{1, ..., n\}$ are continuous, then applying the probability integral transform to each random variable gives the random vector:

$$(U_1, ..., U_n) = (F_1(v_1), ...F_2(v_2)) \tag{7.1}$$

which has uniformly distributed marginals in $[0, 1]$. The copula of the random variables $V_i, \forall i \in \{1, ..., n\}$ is the joint cumulative distribution function of $U_i, \forall i \in \{1, ..., n\}$:

$$C(u_1, ..., u_n) = \mathsf{P}(U_1 \leq u_1 \& ... \& U_n \leq u_n) \tag{7.2}$$

Therefore, given a known copula with specified dependency structure in equation (7.2), one can be reverse the process to generate samples from any multivariate distribution. The generated samples are constructed as:

$$(V_1, ..., V_n) = (F_1^{-1}(U_1), ..., F_1^{-1}(U_1)) \tag{7.3}$$

There are several families of copulas such as Archimedean and elliptical copulas. Although different copulas can be constructed from the same marginals or with the same rank correlation, they can still provide very different dependence structures. This is why the observation of data and the sensitivity of simulation results with respect to different dependence structures is important for analysis. This work analyzes the results from two different elliptical copulas: Gaussian copula and t-copulas with Weibull marginal distributions. Figure 7.2 (a) shows the wind speed/reference power characteristic $F(v_i)$, and

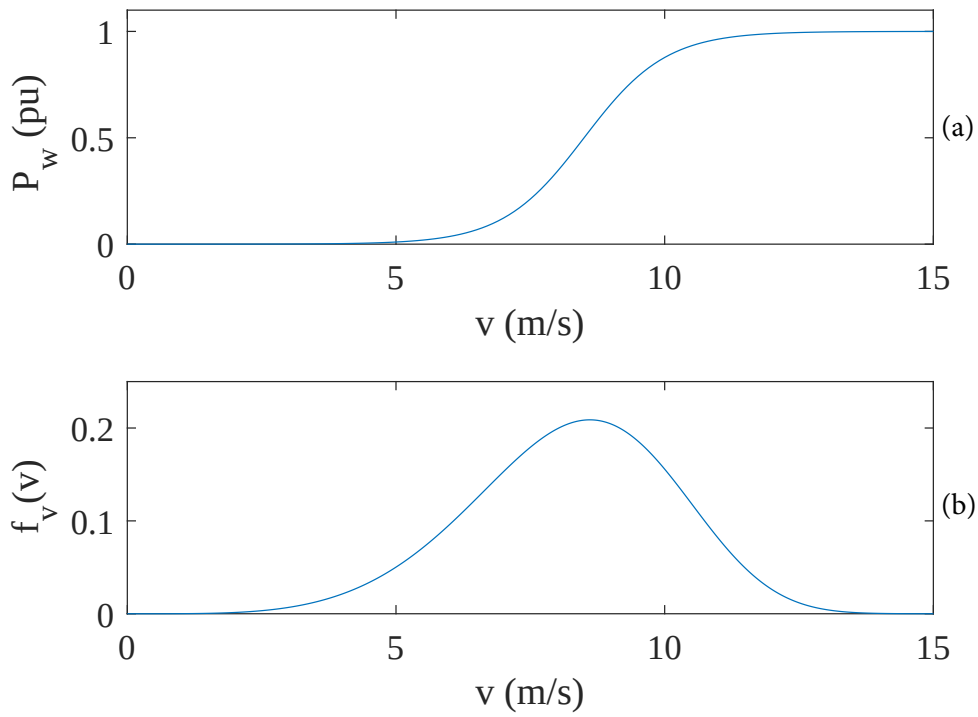

Figure 7.2: Wind speed-power characteristic and wind speed distribution.

Figure 7.2 (b) shows the marginal Weibull probability density function with shape parameter $b = 5$ and scale parameter $a = 9$ used for analysis [123].

Correlation measure

To express the desired correlation between the constructed random variables, a rank correlation coefficient is needed. This rank correlation is preserved under nonlinear transformations, thus, it is more appropriate than the linear correlation ρ, which is still needed to parameterize the copula. Consider the relationship between Kendall's τ rank coefficient and the linear correlation coefficient ρ as follows:

$$\rho = \sin(\tau \frac{\pi}{2}) \tag{7.4}$$

The selection of Kendall's coefficient in the sample generation for analysis of dynamic performance is done by the observation of real wind speed data taken from the National

Renewable Energy Laboratory (NREL) [125]. Figure 7.3 (a) shows the time series of wind speed over a day with resolution of 1 minute for two measurement stations at 30 ft of height: University of Oregon (UO SRML) and University of Nevada-Las Vegas (UNLV). Figure 7.3 (b) shows the dispersion plot of the two time series. The calculated Kendall correlation coefficient is $\tau = 0.3743$.

Figure 7.4 (a) compares the times series of wind speed measurements at UNLV and SOLRMAP Utah Geological Survey (USEP) Cedar. Figure 7.4 (b) shows the dispersion plot with a Kendall correlation coefficient of $\tau = 0.3835$.

Note that the above measurement points are located about 180 miles apart from each other in western North America, but still their data exhibits an important dependency. Based on the above, three cases are presented for analysis in the next section: (a) no correlation $\tau = 0$, (b) medium correlation $\tau = 0.4$ and (c) high correlation $\tau = 0.8$.

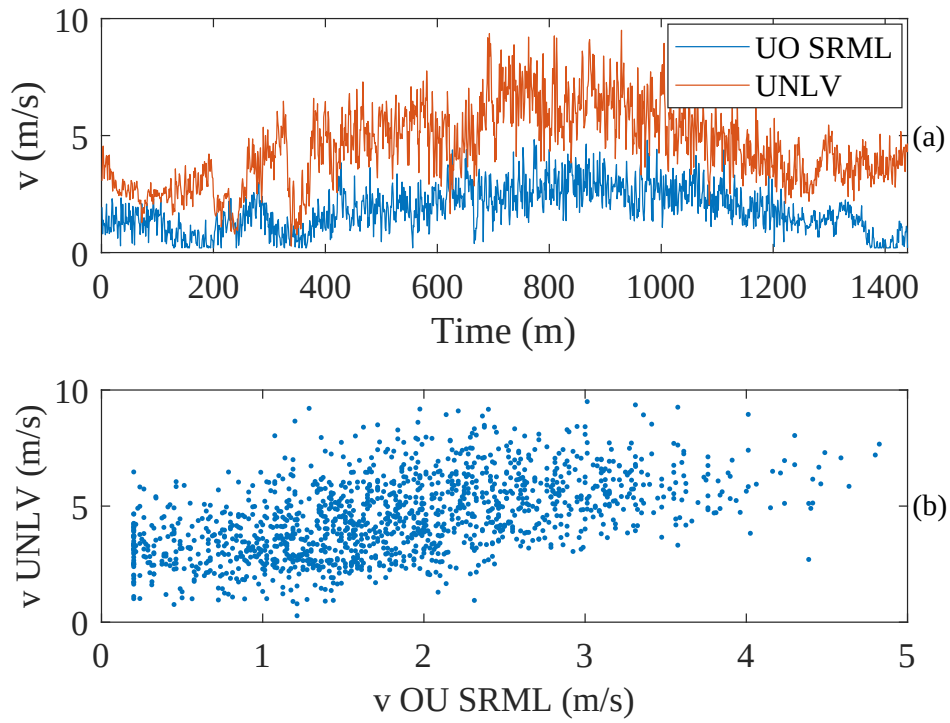

Figure 7.3: Time series for wind speed at two measurement stations.

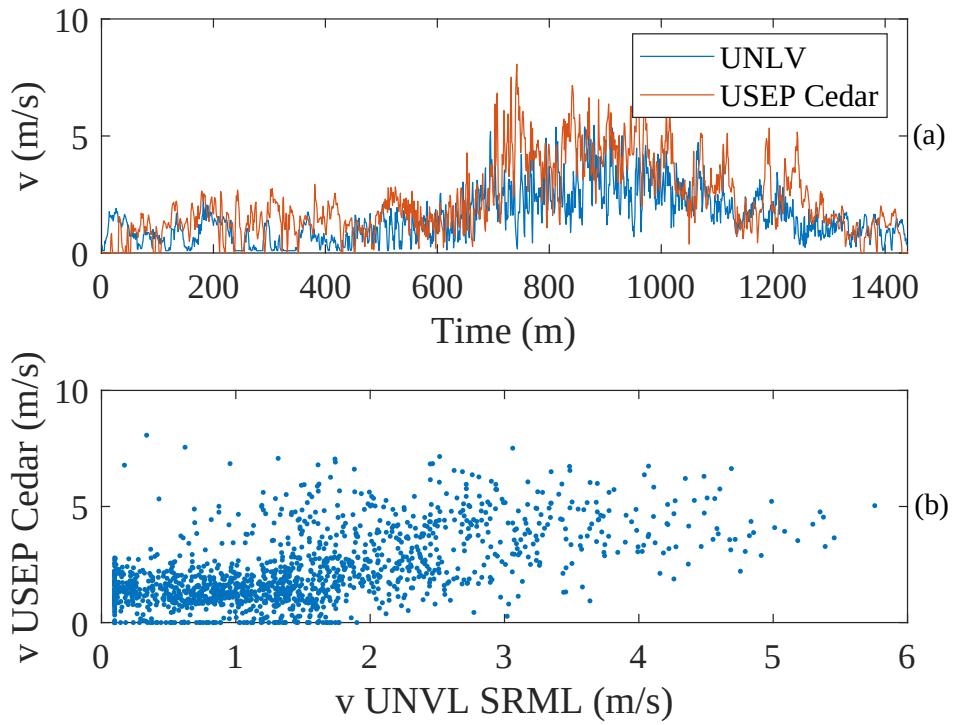

Figure 7.4: Dispersion plot of wind speed at two locations.

7.2 Case Study

Simulations are performed in the western North America power system using the 179-bus Western Electricity Coordinating Council (WECC) model with nominal penetration of wind power of 10%. The system data and the DFIG-based wind turbine locations are taken from [112] and [8] respectively. The model captures the well known "NS mode A", "NS mode B", "BC mode" and "Montana mode" among others, which have been observed in the wNAPS [118]. The software DIgSILENT PowerFactory is used for simulations with 6th order models for synchronous generator, IEEE standard governor models (IEESGO) and different excitation systems. Additionally, some generators are equipped with PSSs and tuned to achieve a desired damping ratio for the electromechanical modes in the mean case scenario. The DFIG-based wind turbines use the software default model, which is based on [110]. Figure 7.5 shows the system topology and the wind turbine locations.

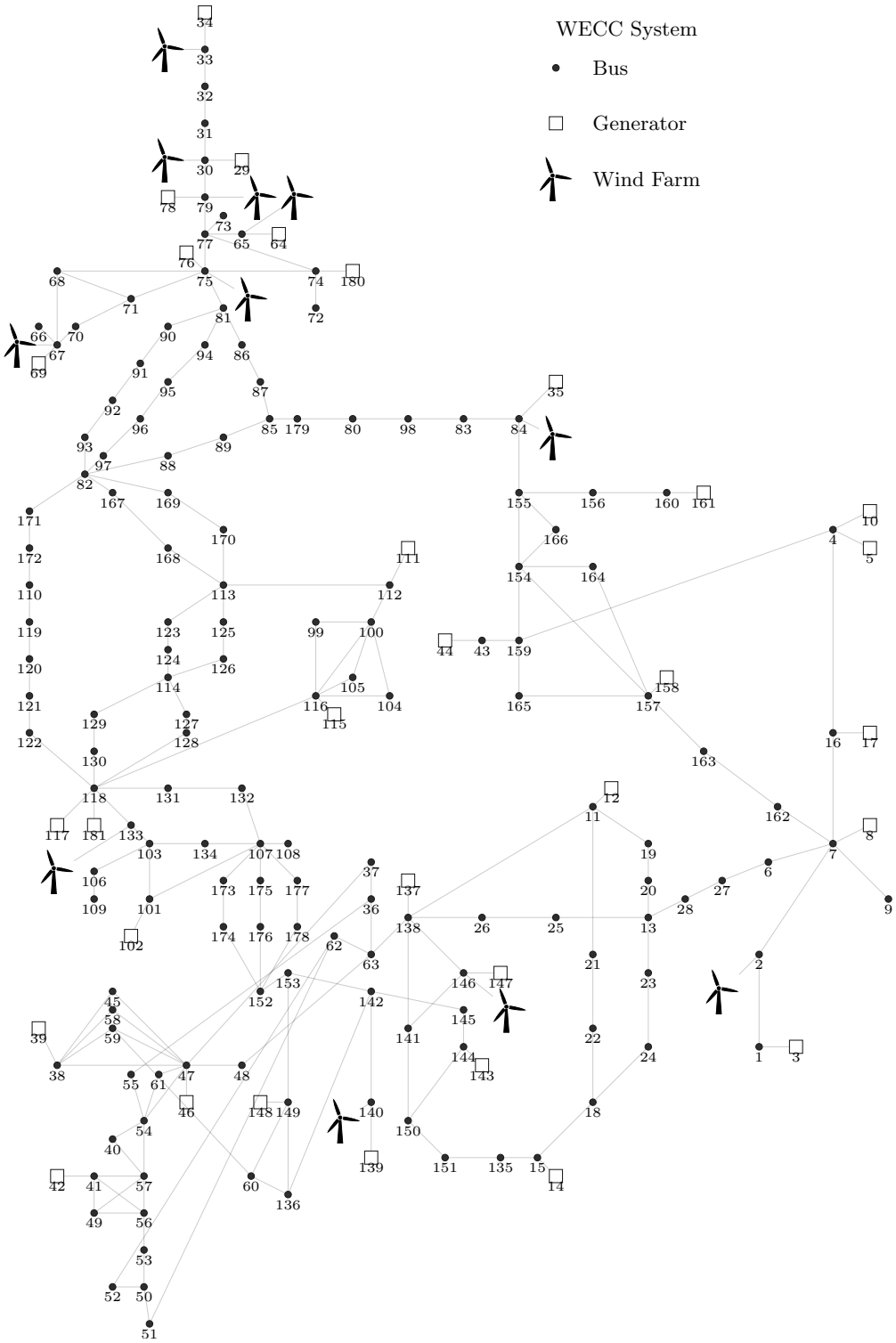

Figure 7.5: 179-bus WECC model.

7.2.1 Input model

The 179-bus WECC system is employed for Monte Carlo simulations. The dynamic model is initialized with random correlated wind power data generated from correlated wind speed through the characteristic in Figure 7.2. The power variations with respect to the mean case scenario are compensated considering generator SG78 and SG117 to participate in secondary frequency control. For simulations $N = 1,000$ data samples of wind speed are considered for the eleven equivalent wind turbines—after verifying convergence of the mean and variance of the results. The correlation is studied for three different scenarios (a) no correlation $\tau = 0$, (b) medium correlation $\tau = 0.4$ and (c) high correlation $\tau = 0.8$. The correlation is defined between the pairs (v_{33}, v_{30}), (v_{30}, v_{79}), (v_{33}, v_{79}) and (v_{146}, v_{140})—with v_i the wind speed of the WT connected at bus i. Furthermore, the effect of the dependence structure is investigated. Figure 7.6 and 7.7 show the dispersion plot of the pair (v_{33}, v_{30}) for medium correlation with Gaussian copula and t-copula, respectively.

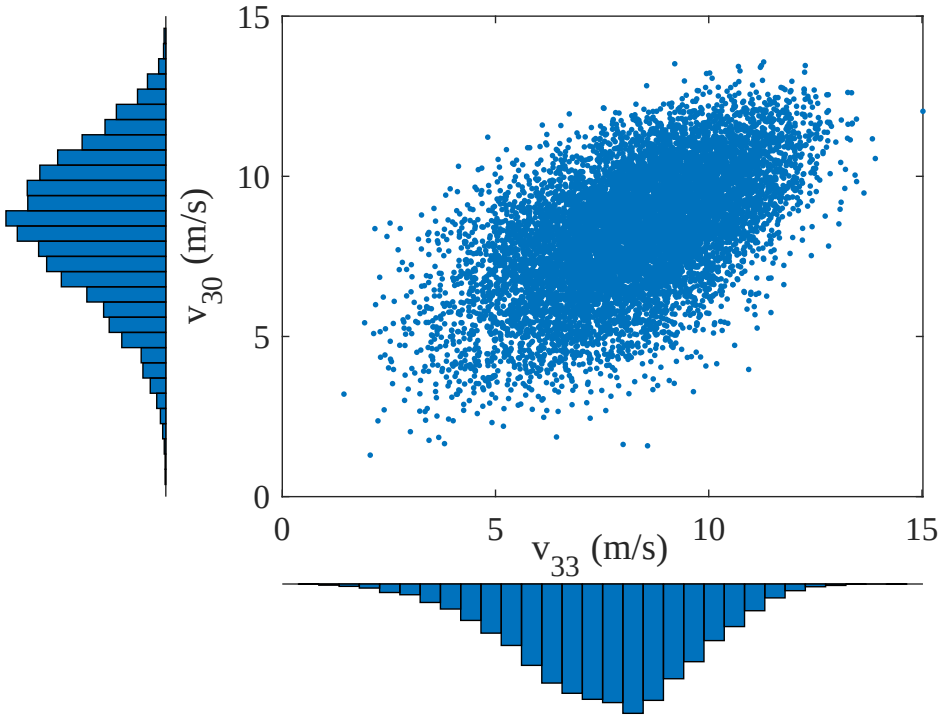

Figure 7.6: Correlated wind speed at WT33 and WT30 generated from Gaussian copula.

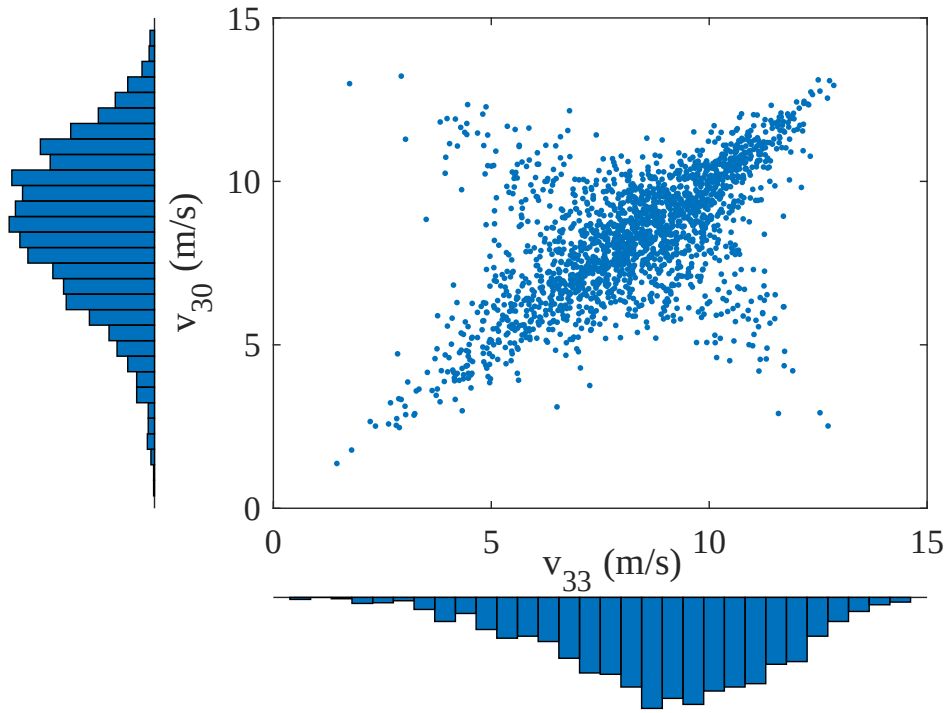

Figure 7.7: Correlated wind speed at WT33 and WT30 generated from t-copula.

7.2.2 Dynamic performance assessment

For each power scenarios $k \in \{1, ..., N\}$ obtained from the input model, a linearized system matrix $A_k \in \mathbb{R}^n$, such that $\dot{x} = A_k x, \quad x(t_0) = x_0$ is obtained, where n is the number of state variables and $x \in \mathbb{R}^n$ is the vector of state variables. Moreover, for each scenario it is possible to calculate $\Lambda_k = M_k^{-1} A_k M_k = \text{diag}\{\lambda_i^{(k)}\}$, where $\lambda_i^{(k)}$ is the i-th system eigenvalue associated with scenario k and $M_k = \{v_1^{(k)}, v_k^{(k)}, ...v_n^{(k)}\}$ is the matrix of right eigenvectors for scenario k. Using these matrices the state space model can be transformed into $\dot{z} = \Lambda z, \quad z_0^{(k)} = M_k^{-1} x_0$ and $z^{(k)} = M_k^{-1} x$. By also defining the transformed inertia matrix $G^{(k)} = M_k^T 2H\omega_s M_k$, with H the inertia matrix in s and $\omega_b = 120\pi$, the oscillation energy for scenario k following the disturbance x_0 becomes:

$$E_k^{(k)}(t) = \sum_{j=1}^{p} H_j \omega_s \Delta\omega_j^2(t) = x^T H \omega_s x \tag{7.5}$$

$$= \frac{1}{2} z^{(k)T} G^{(k)} z^{(k)} \in \mathbb{R} \tag{7.6}$$

Assuming stability, the time integral of the oscillation energy, known as total action, is defined as:

$$S_{\infty}^{(k)}(x_0) = -\frac{1}{2}\sum_{j=1}^{n}\sum_{i=1}^{n}\frac{z_{0i}^{(k)} z_{0j}^{(k)} g_{ij}^{(k)}}{(\lambda_i^{(k)} + \lambda_j^{(k)})} \tag{7.7}$$

where $z_{0i}^{(k)}$ is the i-th entry of the vector $z_0^{(k)}$ and $g_{ij}^{(k)}$ is the the entry in the i-th row and j-th column of $G^{(k)}$. Note that S_{∞}^{k} provides a measure of how quickly the system oscillation energy approaches to steady state after a disturbance—for more details refer to [116].

7.2.3 Analysis

Consider four frequently known disturbances in the system x_0^{γ} $\forall\gamma \in \{1, ...4\}$: (1) Palo verde (SG14), (2) Jhon Day (SG76),(3) San Juan (SG17) and (4) Diablo (SG102). Thus, the expected value of the total action becomes:

$$\mathbb{E}[S_{\infty}^{k}] = \sum_{\gamma=1}^{4} S_{\infty}^{(k)}(x_0^{\gamma}) \times \mathsf{P}(x_0^{\gamma}) \tag{7.8}$$

Considering equal probabilities in equation (7.8), the probability density function of the expected total action for Gaussian and t-copula are shown in Figure 7.8.

The first observation from the results in Figure 7.8 is that the outcome of the Monte Carlo simulation is robust against the dependence structure chosen for analysis. Both Gaussian and t-copula provide similar results for the fitted pdf of the expected total action. The second observation is in regards to the effect of increasing correlation, which flatten the pdf as the correlation becomes larger. This translates to overestimation of probabilities when correlation is not considered. Figure 7.9 shows the cumulative distribution for the Gaussian copula for the three correlation cases. For illustration purposes assume that an expected total action $\mathbb{E}[S_{\infty}^{k}] = 0.49$ is unacceptable for a reliable operation, meaning the system is close to instability, the oscillation takes too long to be damped or the energy associated with the oscillation is dangerous for the available power transfer capability. Then a system planner needs to calculate the probability associated with this condition.

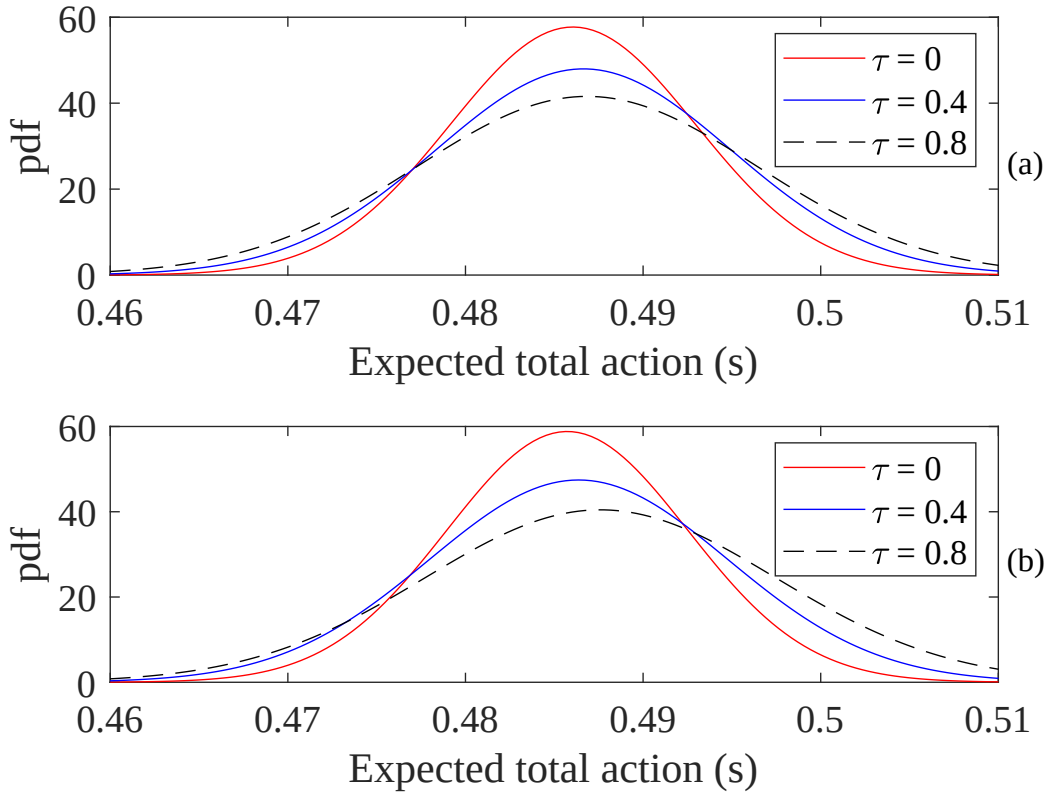

Figure 7.8: (a) pdf resulting from Gaussian copula. (b) pdf resulting from t-copula

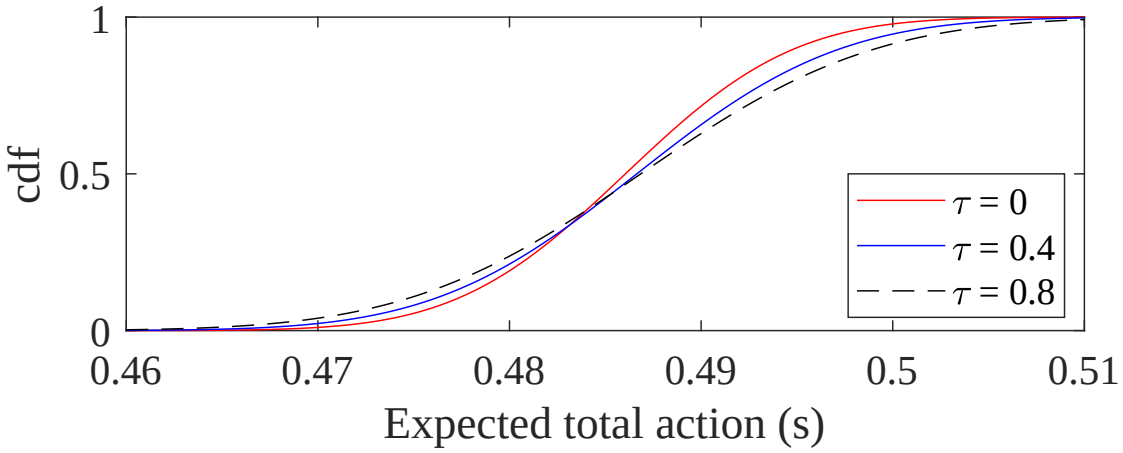

Figure 7.9: Cumulative density function for different correlations.

The probability is calculated as $\mathsf{P}(\mathbb{E}[S_\infty^k] \leq 0.495) = \mathsf{cdf}(0.495)$, which corresponds to 0.91 for no correlation, 0.85 for medium correlation and 0.81 for high correlation. This occurs because the no correlation case considers unrealistic wind speed/power scenarios providing more conservative results.

7.3 Summary

This paper analyzes the effect of spatial correlation of nearby wind farms on the power system dynamic performance, measured in terms of oscillation energy and total action. The correlated samples are generated by using copula theory, two copulas are evaluated to investigate the effect of the dependence structure in the results. Monte Carlo simulations are performed in the 179-bus WECC system with eleven equivalent wind turbines. The results show that disregarding correlation between the wind speed of geographically closed wind farms leads to overestimation of critical probabilities, which can result in misguided planning and operational decisions based on conservative estimates of dynamic performance affecting the system reliability. Furthermore, the results based on the expected value of the total action are robust against the dependence structures studied in this work.

Chapter 8

Conclusions

This PhD dissertation studies electromechanical oscillations in power systems from three different perspectives: (a) modeling and control design of EIR-based damping controllers, (b) performance evaluation for multi-critical mode scenario and coordination of damping controllers and (c) analysis of the selection site for EIR-based damping controllers in systems with high generation variability using a probabilistic framework. The modeling and control part is performed for a flywheel energy storage system and a large-scale solar PV plant. Both of these EIRs show great potential to improve power system stability by taking advantage of their fast real power injection capabilities. An appropriate electromechanical model for the FES is developed for bulk power system analysis. Similarly, a step-down and modulation control strategy is incorporated in the PV plant to enable damping control without the need for curtailment. Simulations carried out in large test cases such as the Chilean power grid and the WECC system validate the results, showing the benefits of using these EIRs.

The performance evaluation and coordination part provides a new global performance measure for oscillation analysis in systems with several critically low damping ratios, and proposes a method to coordinate damping controllers in real time to avoiding adverse dynamic behaviors. The approach, based on the physical meaning of the system oscillation energy, measures the magnitude of the energy exchange between synchronous generators and the duration of the oscillation. The total action and total action sensitivity are proposed for comparing the performance of different EIR-based damping controllers. Results show that the EIRs can be utilized in a more effective way by looking at excited modes, rather than all

critical modes in the traditional formulation. This idea is then used to implement a fault-adaptive coordination. The coordination estimates the changes in the total action produced by binary switching on/off of the damping control loop in different EIRs located among the system. Results in the 179-bus WECC system show the benefits of this coordination and the robustness against communication delays.

Finally, the analysis of location of EIR-based damping controllers in systems with high variability introduces a new perspective and provides results for a new planning problem in power systems. The approach successfully determines the location of an EIR that maximizes the improvement in the system stability. The approach uses the total action to compare the performance of the system for a wide-range of wind generation scenarios, generated from their respective probability density function in Monte Carlo simulations. Furthermore, the role of spatial correlation between geographically near wind farms is also studied. The results show the importance of correlation, in order to avoid over estimation of probabilities for critical or under-critical scenarios, which may result in inefficient location decisions for system operators.

Bibliography

[1] J. Chow, J. J. Sanchez-Gasca, H. Ren, and S. Wang, "Power system damping controller design using multiple input signals," *IEEE Control Systems*, vol. 20, no. 4, pp. 82–90, Aug 2000. 1

[2] D. N. Kosterev, C. W. Taylor, and W. A. Mittelstadt, "Model validation for the august 10, 1996 WSCC system outage," *IEEE Transactions on Power Systems*, vol. 14, no. 3, pp. 967–979, Aug 1999. 1

[3] N. Martins and L. T. G. Lima, "Determination of suitable locations for power system stabilizers and static var compensators for damping electromechanical oscillations in large scale power systems," *IEEE Transactions on Power Systems*, vol. 5, no. 4, pp. 1455–1469, Nov 1990. 1

[4] H. F. Wang, "Selection of robust installing locations and feedback signals of facts-based stabilizers in multi-machine power systems," *IEEE Transactions on Power Systems*, vol. 14, no. 2, pp. 569–574, May 1999. 1

[5] H. Silva-Saravia, H. Pulgar-Painemal, and J. M. Mauricio, "Flywheel energy storage model, control and location for improving stability: The Chilean case," *IEEE Transactions on Power Systems*, vol. 32, no. 4, pp. 3111–3119, July 2017. 2, 6, 61

[6] D. Rimorov, A. Heniche, I. Kamwa, G. Stefopoulos, S. Babaei, and B. Fardanesh, "Inter-area oscillation damping and primary frequency control of the new york state power grid with multi-functional multi-band power system stabilizers," in *2016 IEEE Power and Energy Society General Meeting (PESGM)*, July 2016, pp. 1–5. 2

[7] L.-J. Cai and I. Erlich, "Simultaneous coordinated tuning of pss and facts damping controllers in large power systems," *IEEE Transactions on Power Systems*, vol. 20, no. 1, pp. 294–300, Feb 2005. 2

[8] M. E. Raoufat, K. Tomsovic, and S. M. Djouadi, "Dynamic control allocation for damping of inter-area oscillations," *IEEE Transactions on Power Systems*, vol. PP, no. 99, pp. 1–1, 2017. 2, 76, 77, 104

[9] C. Jing, J. D. McCalley, and M. Kommareddy, "An energy approach to analysis of interarea oscillations in power systems," *IEEE Transactions on Power Systems*, vol. 11, no. 2, pp. 734–740, May 1996. 2

[10] A. R. Messina, M. Ochoa, and E. Barocio, "Use of energy and power concepts in the analysis of the inter-area mode phenomenon," *Electric Power Systems Research*, vol. 59, no. 2, pp. 111–119, 2001. 2

[11] Y. Yu, S. Grijalva, J. J. Thomas, L. Xiong, P. Ju, and Y. Min, "Oscillation energy analysis of inter-area low-frequency oscillations in power systems," *IEEE Transactions on Power Systems*, vol. 31, no. 2, pp. 1195–1203, March 2016. 2

[12] L. Chen, Y. Min, Y. P. Chen, and W. Hu, "Evaluation of generator damping using oscillation energy dissipation and the connection with modal analysis," *IEEE Transactions on Power Systems*, vol. 29, no. 3, pp. 1393–1402, May 2014. 2

[13] F. Gonzalez-Longatt, "Effects of the synthetic inertia from wind power on the total system inertia: simulation study," in *2012 2nd International Symposium on Environment Friendly Energies and Applications (EFEA)*, June 2012, pp. 389–395. 3

[14] Y. Chen, R. Hesse, D. Turschner, and H. P. Beck, "Improving the grid power quality using virtual synchronous machines," in *2011 International Conference on Power Engineering, Energy and Electrical Drives (POWERENG)*, May 2011, pp. 1–6. 3

[15] E.-Z. Zhou, "Application of static var compensators to increase power system damping," *IEEE Transactions on Power Systems*, vol. 8, no. 2, pp. 655–661, May 1993. 3

[16] L. Angquist, B. Lundin, and J. Samuelsson, "Power oscillation damping using controlled reactive power compensation-a comparison between series and shunt approaches," *IEEE Transactions on Power Systems*, vol. 8, no. 2, pp. 687–700, May 1993. 3

[17] P. Dolan, J. Smith, and W. Mittelstadt, "A study of TCSC optimal damping control parameters for different operating conditions," *IEEE Transactions on Power Systems*, vol. 10, no. 4, pp. 1972–1978, Nov 1995. 3

[18] N. Yang, Q. Liu, and J. McCalley, "TCSC controller design for damping interarea oscillations," *IEEE Transactions on Power Systems*, vol. 13, no. 4, pp. 1304–1310, Nov 1998. 3

[19] F. A. Bhuiyan and A. Yazdani, "Energy storage technologies for grid-connected and off-grid power system applications," in *Electrical Power and Energy Conference (EPEC), 2012 IEEE*, Oct 2012, pp. 303–310. 3

[20] H. Chen, T. N. Cong, W. Yang, C. Tan, Y. Li, and Y. Ding, "Progress in electrical energy storage system: A critical review," *Progress in Natural Science*, vol. 19, no. 3, pp. 291–312, 2009. 3

[21] X. Li, C. Hu, C. Liu, and D. Xu, "Modeling and control of aggregated super-capacitor energy storage system for wind power generation," in *Industrial Electronics, 2008. IECON 2008. 34th Annual Conference of IEEE*, Nov 2008, pp. 3370–3375. 3

[22] J. Zhang, "Research on super capacitor energy storage system for power network," in *2005 International Conference on Power Electronics and Drives Systems*, vol. 2, Nov 2005, pp. 1366–1369. 3

[23] J. C. Neely, R. H. Byrne, R. T. Elliott, C. A. Silva-Monroy, D. A. Schoenwald, D. J. Trudnowski, and M. K. Donnelly, "Damping of inter-area oscillations using energy storage," in *2013 IEEE Power Energy Society General Meeting*, July 2013, pp. 1–5. 3

[24] C. F. Lu, C. C. Liu, and C. J. Wu, "Dynamic modelling of battery energy storage system and application to power system stability," *IEE Proceedings - Generation, Transmission and Distribution*, vol. 142, no. 4, pp. 429–435, Jul 1995. 3

[25] D. Zhang, M. Zarghami, T. Liang, and M. Vaziri, "A state-space model for integration of battery energy storage systems in bulk power grids," in *North American Power Symposium (NAPS), 2015*, Oct 2015, pp. 1–5. 3

[26] A. Adrees, H. Andami, and J. V. Milanovi, "Comparison of dynamic models of battery energy storage for frequency regulation in power system," in *2016 18th Mediterranean Electrotechnical Conference (MELECON)*, April 2016, pp. 1–6. 3

[27] X. Li, Y. Huang, J. Huang, S. Tan, M. Wang, T. Xu, and X. Cheng, "Modeling and control strategy of battery energy storage system for primary frequency regulation," in *2014 International Conference on Power System Technology (POWERCON)*, Oct 2014, pp. 543–549. 3

[28] M. W. Tsang and D. Sutanto, "Control strategies to damp inter-area oscillations using a battery energy storage system," in *1998 International Conference on Energy Management and Power Delivery, 1998. Proceedings of EMPD '98.*, vol. 1, Mar 1998, pp. 241–246 vol.1. 3

[29] ——, "Damping inter-area oscillation using a battery energy storage system," in *Fourth International Conference on Advances in Power System Control, Operation and Management, 1997. APSCOM-97.(Conf. Publ. No. 450)*, vol. 2, Nov 1997, pp. 409–414 vol.2. 3

[30] ——, "Power system stabiliser using energy storage," in *Power Engineering Society Winter Meeting, 2000. IEEE*, vol. 2, 2000, pp. 1354–1359 vol.2. 3

[31] S. Samineni, B. K. Johnson, H. L. Hess, and J. D. Law, "Modeling and analysis of a flywheel energy storage system for voltage sag correction," *IEEE Transactions on Industry Applications*, vol. 42, no. 1, pp. 42–52, Jan 2006. 3

[32] G. Li, J. Zhang, S. Cheng, J. Wen, and Y. Pan, "State space formulation and stability analysis of a doubly-fed induction machine with a flywheel energy storage system," in *2006 International Conference on Power System Technology*, Oct 2006, pp. 1–6. 3

[33] C. F. Lu, C. C. Liu, and C. J. Wu, "Dynamic modelling of battery energy storage system and application to power system stability," *IEE Proceedings - Generation, Transmission and Distribution*, vol. 142, no. 4, pp. 429–435, Jul 1995. 3

[34] S. Lin-jun, Z. Lei, Z. Min-hui, and T. Guo-qing, "Applications of fess in power system muti-mode oscillations," in *2011 4th International Conference on Electric Utility Deregulation and Restructuring and Power Technologies (DRPT)*. IEEE, 2011, pp. 1732–1736. 3

[35] L. Shi, S. Chen, J. Liu, M. Zhuang, and G. Tang, "Design of robust fess-based stabilizers in multi-machine power systems," in *2011 International Conference on Advanced Power System Automation and Protection (APAP)*, vol. 1, Oct 2011, pp. 431–435. 3

[36] L. Wang, J. Y. Yu, and Y. T. Chen, "Dynamic stability improvement of an integrated offshore wind and marine-current farm using a flywheel energy-storage system," *IET Renewable Power Generation*, vol. 5, no. 5, pp. 387–396, September 2011. 3

[37] American Wind Energy Association, *"AWEA U.S. Wind Industry Third Quarter 2018 Market Report"*. [Online]. Available: http://www.awea.org [Accessed: November 2018]. 3

[38] F. M. Hughes, O. Anaya-Lara, N. Jenkins, and G. Strbac, "A power system stabilizer for DFIG-based wind generation," *IEEE Transactions on Power Systems*, vol. 21, no. 2, pp. 763–772, May 2006. 3

[39] Y. Zhang, K. Tomsovic, S. M. Djouadi, and H. Pulgar-Painemal, "Hybrid controller for wind turbine generators to ensure adequate frequency response in power networks," *IEEE Journal on Emerging and Selected Topics in Circuits and Systems*, vol. 7, no. 3, pp. 359–370, 2017. 3

[40] Solar energy industries association, *"U.S. Solar Market insight Executive summary Third Quarter 2018"*. [Online]. Available: https://www.seia.org/research-resources/solar-market-insight-report-2018-q3 [Accessed: November 2018]. 3

[41] S. You, G. Kou, Y. Liu, X. Zhang, Y. Cui, M. J. Till, W. Yao, and Y. Liu, "Impact of high pv penetration on the inter-area oscillations in the u.s. eastern interconnection," *IEEE Access*, vol. 5, pp. 4361–4369, 2017. 4

[42] R. Shah, N. Mithulananathan, and K. Y. Lee, "Design of robust power oscillation damping controller for large-scale pv plant," in *2012 IEEE Power and Energy Society General Meeting*, July 2012, pp. 1–8. 4

[43] D. Remon, A. M. Cantarellas, J. M. Mauricio, and P. Rodriguez, "Power system stability analysis under increasing penetration of photovoltaic power plants with synchronous power controllers," *IET Renewable Power Generation*, vol. 11, no. 6, pp. 733–741, 2017. 4

[44] R. G. Wandhare and V. Agarwal, "Novel stability enhancing control strategy for centralized pv-grid systems for smart grid applications," *IEEE Transactions on Smart Grid*, vol. 5, no. 3, pp. 1389–1396, May 2014. 4

[45] R. K. Varma and H. Maleki, "PV solar system control as STATCOM (PV-STATCOM) for power oscillation damping," *IEEE Transactions on Sustainable Energy*, pp. 1–1, 2018. 4

[46] R. Shah, N. Mithulananthan, and K. Y. Lee, "Large-scale pv plant with a robust controller considering power oscillation damping," *IEEE Transactions on Energy Conversion*, vol. 28, no. 1, pp. 106–116, March 2013. 4

[47] R. Shah, N. Mithulananthan, K. Y. Lee, and R. C. Bansal, "Wide-area measurement signal-based stabiliser for large-scale photovoltaic plants with high variability and uncertainty," *IET Renewable Power Generation*, vol. 7, no. 6, pp. 614–622, Nov 2013. 4

[48] Y. Shen, W. Yao, J. Wen, and H. He, "Adaptive wide-area power oscillation damper design for photovoltaic plant considering delay compensation," *IET Generation, Transmission Distribution*, vol. 11, no. 18, pp. 4511–4519, 2017. 4

[49] T. Smed and G. Andersson, "Utilizing hvdc to damp power oscillations," *IEEE Transactions on Power Delivery*, vol. 8, no. 2, pp. 620–627, April 1993. 4

[50] V. A. K. Pappu, B. Chowdhury, and R. Bhatt, "Implementing frequency regulation capability in a solar photovoltaic power plant," in *North American Power Symposium 2010*, Sep. 2010, pp. 1–6. 4

[51] A. Hoke and D. Maksimovi, "Active power control of photovoltaic power systems," in *2013 1st IEEE Conference on Technologies for Sustainability (SusTech)*, Aug 2013, pp. 70–77. 4

[52] Y. Liu, L. Zhu, L. Zhan, J. R. Gracia, T. J. King, and Y. Liu, "Active power control of solar pv generation for large interconnection frequency regulation and oscillation damping," *International Journal of Energy Research*, vol. 40, no. 3, pp. 353–361. [Online]. Available: https://onlinelibrary.wiley.com/doi/abs/10.1002/er.3362 4, 48

[53] P. Denholm, "Energy storage to reduce renewable energy curtailment," in *2012 IEEE Power and Energy Society General Meeting*, 2012, pp. 1–4. 4

[54] M. Steurer, U. Fahl, A. Vo, and P. Deane, "Chapter 15 - curtailment: An option for cost-efficient integration of variable renewable generation?" in *Europe's Energy Transition - Insights for Policy Making*, M. Welsch, S. Pye, D. Keles, A. Faure-Schuyer, A. Dobbins, A. Shivakumar, P. Deane, and M. Howells, Eds. Academic Press, 2017, pp. 97 – 104. [Online]. Available: http://www.sciencedirect.com/science/article/pii/B9780128098066000158 4, 51

[55] Y. Guo, D. J. Hill, and Y. Wang, "Global transient stability and voltage regulation for power systems," *IEEE Transactions on Power Systems*, vol. 16, no. 4, pp. 678–688, Nov 2001. 5

[56] Y. Wang and D. J. Hill, "Robust nonlinear coordinated control of power systems," *Automatica*, vol. 32, no. 4, pp. 611–618, 1996. 5

[57] Y. Wang, D. J. Hill, R. H. Middleton, and L. Gao, "Transient stability enhancement and voltage regulation of power systems," *IEEE Transactions on Power Systems*, vol. 8, no. 2, pp. 620–627, May 1993. 5

[58] K. S. Narendra and J. Balakrishnan, "Improving transient response of adaptive control systems using multiple models and switching," *IEEE Transactions on Automatic Control*, vol. 39, no. 9, pp. 1861–1866, Sept 1994. 5

[59] J. Neely, J. Johnson, R. Byrne, and R. T. Elliott, "Structured optimization for parameter selection of frequency-watt grid support functions for wide-area damping," *International Journal of Distributed Energy Resources and Smart Grids, DERlab/SIRFN Special Issue on Pre-standardisation Activities in Grid Integration of DER*, 2015. 5

[60] J. C. Neely, R. H. Byrne, D. A. Schoenwald, R. T. Elliott, D. Trudnowski, and M. Donnelly, "Optimal control of distributed networked energy storage for improved small-signal stability." 9 2015. 5

[61] Y. Zhang and A. Bose, "Design of wide-area damping controllers for interarea oscillations," *IEEE Transactions on Power Systems*, vol. 23, no. 3, pp. 1136–1143, Aug 2008. 5

[62] X. Lei, E. N. Lerch, and D. Povh, "Optimization and coordination of damping controls for improving system dynamic performance," *IEEE Transactions on Power Systems*, vol. 16, no. 3, pp. 473–480, Aug 2001. 5

[63] P. Pourbeik and M. J. Gibbard, "Simultaneous coordination of power system stabilizers and facts device stabilizers in a multimachine power system for enhancing dynamic performance," *IEEE Transactions on Power Systems*, vol. 13, no. 2, pp. 473–479, May 1998. 5

[64] G. N. Taranto, J.-K. Shiau, J. H. Chow, and H. A. Othman, "A robust decentralized control design for damping controllers in facts applications," in *Proceedings of International Conference on Control Applications*, Sept 1995, pp. 233–238. 5

[65] I. Kamwa, G. Trudel, and L. Gerin-Lajoie, "Robust design and coordination of multiple damping controllers using nonlinear constrained optimization," in *Proceedings of the 21st International Conference on Power Industry Computer Applications. Connecting*

Utilities. PICA 99. To the Millennium and Beyond (Cat. No.99CH36351), May 1999, pp. 87–94. 5

[66] H. Ni, G. T. Heydt, and L. Mili, "Power system stability agents using robust wide area control," *IEEE Transactions on Power Systems*, vol. 17, no. 4, pp. 1123–1131, Nov 2002. 5

[67] D. Angeli and E. Mosca, "Lyapunov-based switching supervisory control of nonlinear uncertain systems," *IEEE Transactions on Automatic Control*, vol. 47, no. 3, pp. 500–505, March 2002. 5

[68] J. P. Hespanha, D. Liberzon, and A. Morse, "Hysteresis-based switching algorithms for supervisory control of uncertain systems," *Automatica*, vol. 39, no. 2, pp. 263 – 272, 2003. [Online]. Available: http://www.sciencedirect.com/science/article/pii/S0005109802002418 5

[69] J. P. Hespanha and A. Morse, "Switching between stabilizing controllers," *Automatica*, vol. 38, no. 11, pp. 1905 – 1917, 2002. [Online]. Available: http://www.sciencedirect.com/science/article/pii/S0005109802001395 5

[70] P. Ouyang, W. Zhang, and M. M. Gupta, "An adaptive switching learning control method for trajectory tracking of robot manipulators," *Mechatronics*, vol. 16, no. 1, pp. 51 – 61, 2006. [Online]. Available: http://www.sciencedirect.com/science/article/pii/S095741580500111X 6

[71] K.-H. Jung, H. Kim, and D. Rho, "Determination of the installation site and optimal capacity of the battery energy storage system for load leveling," *IEEE Transactions on Energy Conversion*, vol. 11, no. 1, pp. 162–167, March 1996. 6

[72] N. S. Rau and Y.-H. Wan, "Optimum location of resources in distributed planning," *IEEE Transactions on Power Systems*, vol. 9, no. 4, pp. 2014–2020, Nov 1994. 6

[73] B. Xu, Y. Wang, Y. Dvorkin, R. Fernndez-Blanco, C. A. Silva-Monroy, J. Watson, and D. S. Kirschen, "Scalable planning for energy storage in energy and reserve markets," *IEEE Transactions on Power Systems*, vol. 32, no. 6, pp. 4515–4527, Nov 2017. 6

[74] A. Giannitrapani, S. Paoletti, A. Vicino, and D. Zarrilli, "Optimal allocation of energy storage systems for voltage control in lv distribution networks," *IEEE Transactions on Smart Grid*, vol. 8, no. 6, pp. 2859–2870, Nov 2017. 6

[75] H. Akagi, "Control strategy and site selection of a shunt active filter for damping of harmonic propagation in power distribution systems," *IEEE Transactions on Power Delivery*, vol. 12, no. 1, pp. 354–363, Jan 1997. 6

[76] W. Huang, K. Sun, J. Qi, and J. Ning, "Optimal allocation of dynamic var sources using the voronoi diagram method integrating linear programing," *IEEE Transactions on Power Systems*, vol. 32, no. 6, pp. 4644–4655, Nov 2017. 6

[77] D. B. Liu, L. J. Shi, Q. Xu, W. J. Du, and H. F. Wang, "Selection of installing locations of flywheel energy storage system in multimachine power systems by modal analysis," in *2009 International Conference on Sustainable Power Generation and Supply*, April 2009, pp. 1–4. 6

[78] L. Zhang, F. Wang, Y. Liu, M. R. Ingram, S. Eckroad, and M. L. Crow, "Facts/ess allocation research for damping bulk power system low frequency oscillation," in *2005 IEEE 36th Power Electronics Specialists Conference*, June 2005, pp. 2494–2500. 6

[79] H. Pulgar-Painemal and R. Gálvez-Cubillos, "Wind farms participation in frequency regulation and its impact on power system damping," in *2013 IEEE Grenoble Conference*, June 2013, pp. 1–4. 6, 27

[80] H. Silva-Saravia, Y. Wang, and H. Pulgar-Painemal, "Determining wide-area signals and locations of regulating devices to damp inter-area oscillations through eigenvalue sensitivity analysis using DIgSILENT Programming Language," in *Advanced Smart Grid Functionalities Based on PowerFactory*. Springer, 2018, pp. 153–179. 6

[81] B. K. Poolla, S. Bolognani, and F. Dörfler, "Optimal placement of virtual inertia in power grids," *IEEE Transactions on Automatic Control*, vol. 62, no. 12, pp. 6209–6220, Dec 2017. 7

[82] H. Pulgar-Painemal, Y. Wang, and H. Silva-Saravia, "On inertia distribution, inter-area oscillations and location of electronically-interfaced resources," *IEEE Transactions on Power Systems*, vol. PP, no. 99, pp. 1–1, 2017. 7, 61

[83] Y. Wang, H. Silva-Saravia, and H. Pulgar-Painemal, "Estimating inertia distribution to enhance power system dynamics," in *2017 North American Power Symposium (NAPS)*, Sept 2017. 7

[84] R. C. Burchett and G. Heydt, "Probabilistic methods for power system dynamic stability studies," *IEEE Transactions on Power Apparatus and Systems*, no. 3, pp. 695–702, 1978. 7

[85] S. Q. Bu, W. Du, H. F. Wang, Z. Chen, L. Y. Xiao, and H. F. Li, "Probabilistic analysis of small-signal stability of large-scale power systems as affected by penetration of wind generation," *IEEE Transactions on Power Systems*, vol. 27, no. 2, pp. 762–770, May 2012. 7

[86] Z. W. Wang, C. Shen, and F. Liu, "Probabilistic analysis of small signal stability for power systems with high penetration of wind generation," *IEEE Transactions on Sustainable Energy*, vol. 7, no. 3, pp. 1182–1193, July 2016. 7

[87] X. Y. Bian, Y. Geng, K. L. Lo, Y. Fu, and Q. B. Zhou, "Coordination of PSSs and SVC damping controller to improve probabilistic small-signal stability of power system with wind farm integration," *IEEE Transactions on Power Systems*, vol. 31, no. 3, pp. 2371–2382, May 2016. 7

[88] Y. Zhang, Z. Y. Dong, F. Luo, Y. Zheng, K. Meng, and K. P. Wong, "Optimal allocation of battery energy storage systems in distribution networks with high wind power penetration," *IET Renewable Power Generation*, vol. 10, no. 8, pp. 1105–1113, 2016. 7

[89] P. Li, X. Guan, J. Wu, and X. Zhou, "Modeling dynamic spatial correlations of geographically distributed wind farms and constructing ellipsoidal uncertainty sets for

optimization-based generation scheduling," *IEEE Transactions on Sustainable Energy*, vol. 6, no. 4, pp. 1594–1605, Oct 2015. 7

[90] L. Gang, C. Jinfu, C. Defu, S. Dongyuan, and D. Xianzhong, "Probabilistic assessment of available transfer capability considering spatial correlation in wind power integrated system," *IET Generation, Transmission Distribution*, vol. 7, no. 12, pp. 1527–1535, December 2013. 7

[91] W. Wangdee and R. Billinton, "Considering load-carrying capability and wind speed correlation of wecs in generation adequacy assessment," *IEEE Transactions on Energy Conversion*, vol. 21, no. 3, pp. 734–741, Sept 2006. 8

[92] Y. Chen, J. Wen, and S. Cheng, "Probabilistic load flow method based on nataf transformation and latin hypercube sampling," *IEEE Transactions on Sustainable Energy*, vol. 4, no. 2, pp. 294–301, April 2013. 8

[93] Y. Pan, L. Shi, and Y. Ni, "Modelling of multiple wind farms output correlation based on copula theory," *The Journal of Engineering*, vol. 2017, no. 13, pp. 2303–2308, 2017. 8

[94] R. Pena-Alzola, R. Sebastian, J. Quesada, and A. Colmenar, "Review of flywheel based energy storage systems," in *2011 International Conference on Power Engineering, Energy and Electrical Drives (POWERENG)*, May 2011, pp. 1–6. 14

[95] Beacon Power, LLC. [Online]. Available: http://beaconpower.com [Accessed: January 2016]. 14, 17

[96] R. Cardenas, R. Pena, G. Asher, and J. Clare, "Power smoothing in wind generation systems using a sensorless vector controlled induction machine driving a flywheel," *IEEE Transactions on Energy Conversion*, vol. 19, no. 1, pp. 206–216, March 2004. 14

[97] R. Cardenas, R. Pea, M. Perez, J. Clare, G. Asher, and P. Wheeler, "Power smoothing using a flywheel driven by a switched reluctance machine," *IEEE Transactions on Industrial Electronics*, vol. 53, no. 4, pp. 1086–1093, June 2006. 14

[98] X. Rong, W. Xiaoru, and T. Jin, "Operation control of flywheel energy storage system with wind farm," in *Control Conference (CCC), 2011 30th Chinese*, July 2011, pp. 6208–6212. 14

[99] A. EL-Refaie and T. Jahns, "Comparison of synchronous PM machine types for wide constant-power speed range operation," in *Industry Applications Conference, 2005. Fourtieth IAS Annual Meeting. Conference Record of the 2005*, vol. 2, Oct 2005, pp. 1015–1022 Vol. 2. 14

[100] M. L. Lazarewicz and A. Rojas, "Grid frequency regulation by recycling electrical energy in flywheels," in *Power Engineering Society General Meeting, 2004. IEEE*, June 2004, pp. 2038–2042 Vol.2. 15

[101] M. Chinchilla, S. Arnaltes, and J. Burgos, "Control of permanent-magnet generators applied to variable-speed wind-energy systems connected to the grid," *IEEE Transactions on Energy Conversion*, vol. 21, no. 1, pp. 130–135, March 2006. 17

[102] J. Cleary, M. Lazarewicz, L. Nelson, R. Rounds, and J. Arsenault, "Interconnection study: 5MW of Beacon Power Flywheels on 23 kV line—Tyngsboro, MA," in *2010 IEEE Conference on Innovative Technologies for an Efficient and Reliable Electricity Supply (CITRES)*, Sept 2010, pp. 285–291. 17

[103] A. Carlsson, "The back-to-back converter," Ph.D. dissertation, Department of Industrial Electrical Engineering and Automation, Lund Institute of Technology, 1998. 17

[104] Energy Storage Association. Case studies. [Online]. Available: http://energystorage.org/energy-storage/case-studies [Accessed: January 2016]. 22

[105] Independent System Operator, Northern Chile Interconnected System. [Online]. Available: http://www.cdec-sing.cl (Accessed: January 2016). 22

[106] F. Pagola, I. Perez-Arriaga, and G. C. Verghese, "On sensitivities, residues and participations: applications to oscillatory stability analysis and control," *IEEE Transactions on Power Systems*, vol. 4, no. 1, pp. 278–285, Feb 1989. 25

[107] D. Wu, C. Lin, V. Perumalla, and J. Jiang, "Impact of grid structure on dynamics of interconnected generators," *IEEE Transactions on Power Systems*, vol. 29, no. 5, pp. 2329–2337, Sept 2014. 27

[108] P. Kundur, N. J. Balu, and M. G. Lauby, *Power system stability and control*. McGraw-hill New York, 1994, vol. 7. 34, 41

[109] M. G. Villalva, J. R. Gazoli, and E. R. Filho, "Comprehensive approach to modeling and simulation of photovoltaic arrays," *IEEE Transactions on Power Electronics*, vol. 24, no. 5, pp. 1198–1208, May 2009. 38

[110] DIgSILENT GmbH, *DIgSILENT PowerFactory Application Guide, DFIG template*, 2013. 43, 77, 104

[111] R. T. Elliott, A. Ellis, P. Pourbeik, J. J. Sanchez-Gasca, J. Senthil, and J. Weber, "Generic photovoltaic system models for wecc - a status report," in *2015 IEEE Power Energy Society General Meeting*, July 2015, pp. 1–5. 46

[112] *"Test cases library of sustained power system oscillations,"[Online]*. Available: http://web.eecs.utk.edu/kaisun/Oscillation/. 48, 77, 104

[113] M. Pai, *Power system stability: analysis by the direct method of Lyapunov*. North-Holland Publishing Company, 1981, vol. 3. 55

[114] C. Lanczos, *The variational principles of mechanics*. Courier Corporation, 2012. 59

[115] M. I. Friswell, "Calculation of second-and higher order eigenvector derivatives," *Journal of Guidance, Control, and Dynamics*, vol. 18, no. 4, pp. 919–921, 1995. 60, 73

[116] H. Silva-Saravia, Y. Wang, H. Pulgar-Painemal, and K. Tomsovic, "Oscillation energy based sensitivity analysis and control for multi-mode oscillation systems," in *2018 IEEE Power and Energy Society General Meeting*, August 2018, pp. 1–5. 71, 100, 108

[117] H. Silva-Saravia, H. Pulgar-Painemal, and R. Zaretzki, "Chance-constrained optimal location of damping control actuators under wind power variability," in *2018 IEEE International Conference on Probabilistic Methods Applied to Power Systems (PMAPS)*, June 2018, pp. 1–5. 72

[118] D. Trudnowski, D. Kosterev, and J. Undrill, "PDCI damping control analysis for the western North American power system," in *2013 IEEE Power Energy Society General Meeting*, July 2013, pp. 1–5. 77, 104

[119] D. A. Schoenwald, B. J. Pierre, F. Wilches-Bernal, and D. J. Trudnowski, "Design and implementation of a wide-area damping controller using high voltage DC modulation and synchrophasor feedback," *IFAC-PapersOnLine*, vol. 50, no. 1, pp. 67–72, 2017. 84

[120] B. J. Pierre, F. Wilches-Bernal, D. A. Schoenwald, R. T. Elliott, J. C. Neely, R. H. Byrne, and D. J. Trudnowski, "Open-loop testing results for the pacific DC intertie wide area damping controller," in *2017 IEEE Manchester PowerTech*, June 2017, pp. 1–6. 84

[121] F. Wilches-Bernal, B. J. Pierre, R. T. Elliott, D. A. Schoenwald, R. H. Byrne, J. C. Neely, and D. J. Trudnowski, "Time delay definitions and characterization in the pacific dc intertie wide area damping controller," in *2017 IEEE Power Energy Society General Meeting*, July 2017, pp. 1–5. 84

[122] "IEEE Standard for synchrophasor measurements for power systems," *IEEE Std C37.118.1-2011 (Revision of IEEE Std C37.118-2005)*, pp. 1–61, Dec 2011. 84

[123] S. V. Dhople and A. D. Domínguez-García, "A framework to determine the probability density function for the output power of wind farms," in *2012 North American Power Symposium (NAPS)*, Sept 2012, pp. 1–6. 94, 102

[124] H. A. Pulgar-Painemal and P. W. Sauer, "Dynamic modeling of wind power generation," in *North American Power Symposium (NAPS), 2009*. IEEE, 2009, pp. 1–6. 100

[125] NWTC information portal (NWTC 135-m meteorological towers data repository). [Online]. Available: https://nwtc.nrel.gov/135mData.Lastmodified01-April-2015; Accessed02-October-2018 103

Appendices

A FES plant model parameters

The following FES plant model parameters were used:

$T_w = 10$ s	$R = 2 \times 10^{-3}$ pu	$C = 4$ mF
$T_1 = 0.464$ s	$I_q^{min} = -1.1$ pu	$I_q^{max} = 1.1$ pu
$T_2 = 0.412$ s	$K_v = 10$ pu	$S_b = 1$ MVA
$T_P = 0.01$ s	$K_P = 0.1$ pu	$H = 450$ s
$T_v = 1$ ms	$i_q^{min} = -1.1$ pu	$i_q^{max} = 1.1$ pu
$V_{dc,b} = 750$ V	$\Phi_f = 1$ pu	$K_Q = 10$ pu
$T_C = 0.5$ ms	$i_g^{min} = -1$ pu	$i_g^{max} = 1$ pu
$T_Q = 0.1$ s		

B Linear solution of the SMIB system

Linearize equation (3.1) and (3.2) around ω_e and δ_e (system equilibrium point):

$$\begin{bmatrix} \Delta\dot{\delta} \\ \Delta\dot{\omega} \end{bmatrix} = \underbrace{\begin{bmatrix} 0 & \omega_s \\ -\frac{K_S}{2H} & -\frac{K_D}{2H} \end{bmatrix}}_{A} \begin{bmatrix} \Delta\delta \\ \Delta\omega \end{bmatrix} \tag{1}$$

The eigenvalues of A correspond to $\lambda_{1,2} = \lambda_x \pm j\lambda_y$ where $\lambda_x = -{}^{K_D}/_{4H}$ and $\lambda_y = \sqrt{{K_s}^{\omega_s}/_{2H} - {}^{K_D^2}/_{16H^2}}$. Thus, the solution for the linearized state variables are given by:

$$\Delta\delta(t) = C_1 e^{\lambda_1(t-t_0)} + C_2 e^{\lambda_2(t-t_0)} \tag{2}$$

$$\Delta\omega(t) = \frac{\Delta\dot{\delta(t)}}{\omega_s} = \frac{C_1\lambda_1}{\omega_s} e^{\lambda_1(t-t_0)} + \frac{C_2\lambda_2}{\omega_s} e^{\lambda_2(t-t_0)} \tag{3}$$

where the constants C_1 and C_2 are calculated from the initial conditions when the fault is cleared at t_0. Without loss of generality consider that $t_0 = 0$ and define $\Delta\delta(t_0) = \Delta\delta_0$ and $\Delta\omega(t_0) = \Delta\omega_0$, then from equations (2) and (3) the following set of equations is obtained:

$$\Delta\delta_0 = C_1 + C_2 \tag{4}$$

$$\Delta\omega_0 = \frac{C_1\lambda_1}{\omega_s} + \frac{C_2\lambda_2}{\omega_s} \tag{5}$$

whose solution is $C_1 = (\lambda_y + j\lambda_x)\Delta\delta_0/(2\lambda_y) - j\omega_s\Delta\omega_0/(2\lambda_y)$ and $C_2 = C_1^*$ (note that $j = \sqrt{-1}$ and the symbol * denotes the complex conjugate operator). By replacing C_1 and C_2 in equations (2) and (3):

$$\Delta\delta(t) = \frac{\omega_s\Delta\omega_0 e^{\lambda_x t}}{\lambda_y}\sin(\lambda_y t) - \frac{\Delta\delta_0 e^{\lambda_x t}}{\sin(\theta)}\sin(\lambda_y t - \theta) \tag{6}$$

$$\Delta\omega(t) = -\frac{\Delta\delta_0 e^{\lambda_x t}|\lambda|}{\omega_s\sin(\theta)}\sin(\lambda_y t) + \frac{\Delta\omega_0 e^{\lambda_x t}}{\sin(\theta)}\sin(\lambda_y t + \theta) \tag{7}$$

with $|\lambda| = \sqrt{\lambda_x^2 + \lambda_y^2}$ and $\theta = \arctan({}^{\lambda_y}/_{\lambda_x})$

C Potential energy and total action

Using $\delta \approx \delta_e + \Delta\delta$ in the definition of potential energy and using the first order term in the Taylor expansion of cosine,

$$E_u(\delta) \approx - P_m \Delta\delta - K_S(\cos(\delta_0 + \Delta\delta) - \cos(\delta_0)) \tag{8}$$

$$\approx - P_m \Delta\delta + K_S(\delta_0 \Delta\delta + \Delta\delta^2/2) \tag{9}$$

$$\approx \underbrace{(-P_m + K_S\delta_0)}_{\approx 0} \Delta\delta + K_S \Delta\delta^2/2 \tag{10}$$

Considering that right after a short circuit ${}^{\Delta\delta_0}/_{\sin(\theta)} \ll {}^{\omega_s \Delta\omega_0}/_{\lambda_y}$, the total action calculated from the potential energy is:

$$S_\infty = \lim_{\tau\to\infty} \int_0^\tau E_u(\delta(t))dt \approx \lim_{\tau\to\infty} \int_0^\tau K_s \frac{\Delta\delta(t)^2}{2} dt \tag{11}$$

$$\approx \lim_{\tau\to\infty} \frac{K_S \omega_s^2 \Delta\omega_0^2}{2\lambda_y^2} \int_0^\tau e^{2\lambda_x t} \sin(\lambda_y t)^2 dt \tag{12}$$

$$\approx \frac{K_S \omega_s^2 \Delta\omega_0^2}{8\lambda_x(\lambda_x^2 + \lambda_y^2)} = \frac{H^2 \omega_s \Delta\omega_0^2}{K_D} \tag{13}$$

which yields the same result obtained from the kinetic energy in equation (4.7).

Vita

Horacio Silva-Saravia was born in Valparaiso, Chile. He received his B.Sc. and M.Sc. degrees from the Federico Santa Maria Technical University, Chile in 2014. His research area includes power system dynamics, stability and control, energy storage modeling and applications for power systems, solar PV generation modeling and control, and wind power generation modeling and control.